

**Plasmonic core/half-shell nanoparticles: Exploring half-shell  
growth for Au, TiO<sub>2</sub>, SiO<sub>2</sub>, and Cu<sub>2</sub>O onto silver nanocubes**

by

**Alexandra Gale-Mouldey**

A thesis submitted to the Department of Chemistry

In partial fulfillment of the requirements for the degree of

Master of Science

in

Chemistry

to

Carleton University

Department of Chemistry

Ottawa, Ontario, Canada

August 2018

The undersigned hereby recommends to the

Department of Chemistry

acceptance of the thesis

**Plasmonic core/half-shell nanoparticles: Exploring half-shell growth for  
Au, TiO<sub>2</sub>, SiO<sub>2</sub>, and Cu<sub>2</sub>O onto silver nanocubes**

Submitted by:

Alexandra Gale-Mouldey

In partial fulfillment of the requirements of the degree of

Master of Science in Chemistry

---

Dr. Anatoli Ianoul

(Supervisor)

## Abstract

Core/shell nanoparticles have often been studied due to their attractive optical, electronic, and catalytic properties. By coupling these core/shell features with physical anisotropy of the shell – by selectively capping only a portion of the core – complex nanostructures with unique properties can be formed. This research investigates the synthesis and plasmonic properties of silver nanocube/metal and oxide core/shell nanoparticles with full or partial shells. The shell materials tested were gold, titania, silica, and cuprous oxide. The general method involved growing the shell on a silver nanocube (AgNC) that was partially embedded in a polystyrene thin-film supported by a glass substrate. The amount of shell coverage was dictated by the depth of embedding, and thus nanocube surface exposed and available for reaction. After in-solution shell growth, the particles were removed from the substrate and suspended in solution. The characterization of these particles by UV-vis spectroscopy and transmission electron microscopy confirmed their altered plasmonic properties and their morphology. This partial shell growth technique is ideal for any low temperature, two step core/shell synthesis. The resultant shells had quite distinct morphologies dependant on the shell material chosen. While the gold and titania shell growths are incomplete at this time, silica and cuprous oxide provided positive results. The AgNC/SiO<sub>2</sub> core/shell nanoparticles exhibited a complete and conformal coverage of SiO<sub>2</sub> due to undergrowth between the AgNC and the polystyrene. This undergrowth arises from mild etching of the silver during the silica growth, creating space for the silica precursor to penetrate between the core and the polymer thin-film. The AgNC/Cu<sub>2</sub>O core/shell nanoparticles formed had a distinct half-shell morphology with

either pyramidal or cubic half-shells where the geometry of the shell is dependent upon the order of reagent addition. Furthermore, the cuprous oxide half-shells caused significant modifications to the localized surface plasmon resonance of the AgNC core and resulted in in-solution hybridization of the plasmon modes. The proposed core/half-shell morphology will be particularly advantageous in the formation of dimers for SERS sensing or as individual particles for catalysis.

## **Acknowledgments**

I would like to extend my sincere thank you to Dr. Anatoli Ianoul for his guidance, insight, and motivation to strive for greatness. Many thanks are extended to Daniel Prezgot and Mike Bushell for their talents with FDTD simulations and for being excellent company on this journey. Thank you to Emma Jorgenson for her friendship and help throughout our time at Carleton. Thank you as well to JJ Wang from the Nano Imaging Facility without whom this thesis would have had no results.

I must also extend my appreciation for my family and friends. You gave me endless support during my many years at university, especially in the last few months. You kept me sane and happy. Thank you for letting me talk about my work, no matter how much or how little you understood.

## Table of Contents

|   |             |
|---|-------------|
| <b>Abstract</b> .....   | <b>iii</b>  |
| <b>Acknowledgments</b> .....                                    | <b>v</b>    |
| <b>List of Tables</b> .....                                     | <b>viii</b> |
| <b>List of Figures</b> .....                                    | <b>viii</b> |
| <b>Abbreviations</b> .....                                      | <b>xiv</b>  |
| <br>  |             |
| <b>1 Introduction</b> .....                                     | <b>1</b>    |
| 1.1 ANISOTROPIC PARTICLES.....                                  | 2           |
| 1.1.1 <i>Chemical anisotropy</i> .....                          | 2           |
| 1.1.2 <i>Morphological anisotropy</i> .....                     | 6           |
| 1.1.3 <i>Combining the two anisotropies</i> .....               | 8           |
| 1.2 PLASMONICS .....  | 9           |
| 1.3 EMBEDMENT OF SILVER NANOCUBES INTO POLYMER THIN FILMS ..... | 14          |
| 1.4 CORE/SHELL PARTICLES .....                                  | 17          |
| 1.4.1 <i>Silver nanocube core</i> .....                         | 18          |
| 1.4.2 <i>Gold shell</i> .....                                   | 22          |
| 1.4.3 <i>Titania shell</i> .....                                | 25          |
| 1.4.4 <i>Silica shell</i> .....                                 | 28          |
| 1.4.5 <i>Cuprous oxide shell</i> .....                          | 31          |
| <br>  |             |
| <b>2 Experimental</b> .....                                     | <b>39</b>   |
| 2.1 SUBSTRATE PREPARATION.....                                  | 39          |
| 2.1.1 <i>Silver nanocube synthesis</i> .....                    | 39          |
| 2.1.2 <i>Polystyrene spin coating</i> .....                     | 40          |
| 2.1.3 <i>Langmuir-Schaeffer deposition</i> .....                | 40          |
| 2.1.4 <i>Silver nanocube embedding</i> .....                    | 42          |
| 2.2 HALF-SHELL GROWTH .....                                     | 42          |
| 2.2.1 <i>Gold</i> .....   | 42          |
| 2.2.2 <i>Titania</i> .....                                      | 43          |
| 2.2.3 <i>Silica</i> .....                                       | 43          |
| 2.2.4 <i>Copper oxide</i> .....                                 | 44          |
| 2.3 REMOVAL OF NANOCUBES FROM GLASS-SUPPORTED POLYSTYRENE ..... | 45          |
| 2.4 CHARACTERIZATION.....                                       | 45          |
| 2.4.1 <i>UV-vis spectroscopy</i> .....                          | 45          |
| 2.4.2 <i>Atomic Force Microscopy</i> .....                      | 45          |
| 2.4.3 <i>Transmission Electron Microscopy</i> .....             | 45          |
| <br>  |             |
| <b>3 Results &amp; Discussion</b> .....                         | <b>46</b>   |
| 3.1 SAMPLE PREPARATION .....                                    | 46          |
| 3.2 GOLD SHELL .....  | 50          |
| 3.2.1 <i>Method 1</i> .....                                     | 50          |
| 3.2.2 <i>Method 2</i> .....                                     | 56          |
| 3.2.3 <i>Gold shell conclusions</i> .....                       | 60          |

|          |  |            |
|----------|--|------------|
| 3.3      | TITANIA SHELL .....  | 61         |
| 3.4      | SILICA SHELL .....   | 67         |
| 3.5      | CUPROUS OXIDE SHELL.....                                   | 77         |
| 3.5.1    | <i>FDTD simulated results</i> .....                        | 78         |
| 3.5.2    | <i>Effect of reagent concentration</i> .....               | 83         |
| 3.5.3    | <i>Stepwise addition versus continuous injection</i> ..... | 86         |
| 3.5.4    | <i>Role of lactic acid</i> .....                           | 89         |
| 3.5.5    | <i>Continuous hydrazine injection</i> .....                | 91         |
| 3.5.6    | <i>Copper sulphate as precursor</i> .....                  | 96         |
| 3.5.7    | <i>Effect of cube coverage on optical properties</i> ..... | 102        |
| 3.5.8    | <i>Cuprous oxide conclusions</i> .....                     | 109        |
| <b>4</b> | <b>Conclusion</b> .....                                    | <b>110</b> |
| <b>5</b> | <b>References</b> .....                                    | <b>114</b> |

## List of Tables

|  |    |
|--|----|
| Table 1: Reaction parameters for Method 1 trials .....     | 50 |
| Table 2: Reaction parameters for Method 2 trials .....     | 50 |
| Table 3: Reaction parameters for titania experiments. .... | 61 |
| Table 4: Reaction parameters for silica shell growth.....  | 68 |
| Table 5: Reaction parameters for cuprous oxide growth..... | 78 |

## List of Figures

|  |    |
|--|----|
| Figure 1.1: Schematic illustration of morphological, chemical anisotropy and a particle that carries both types. ....  | 2  |
| Figure 1.2: Above: Schematic of biphasic particle formation. Middle: Schematic of ternary-structure particle formation. Both using microfluidics. M1 and M2 denote immiscible monomers and W indicates the emulsifier. Below: Optical microscopy of (a-c) Biphasic particles, (d) Ternary-structure particles. Insets show fluorescence microscopy of particles. Adapted with permission from Ref[13] Copyright 2006 American Chemical Society. .... | 4  |
| Figure 1.3: Schematic of the particle lithography method. (a) Cationic particle adhered to an anionic substrate. (b) Anionic polyelectrolyte interacts with the accessible portion of the colloid. (c) Particle is removed from substrate. (d) Selective interaction with an anionic particle. Reproduced with permission from Ref [14]. Copyright 2005 American Chemical Society. ....  | 5  |
| Figure 1.4: Schematic illustration of pathways from varied seed structures to their respective anisotropic nanostructures. The {100}, {110}, and {111} facets are shown in green, purple, and orange, respectively. The parameter R represents the ratio between the growth rates in the [100] and [111] directions. Reproduced with permission from Ref[19]. Copyright 2007 Wiley-VCH.....  | 7  |
| Figure 1.5: Schematic illustrations of (a) propagating surface plasmons along a metal film and (b) localized surface plasmons for a metal nanosphere. Reproduced with permission from Ref[29]. Copyright 2009 American Chemical Society. ....  | 9  |
| Figure 1.6: Illustration of the dipolar and quadrupolar modes of a silver nanocube. ....   | 10 |
| Figure 1.7: Plot of (A) the real and (B) the imaginary parts of the dielectric function of silver, gold, and silicon with respect to wavelength. Reproduced with permission from Ref[30]. Copyright 2011 American Chemical Society. ....   | 11 |
| Figure 1.8: Schematic illustration of (a) intrinsic cube modes with induced hybridization from the dielectric; (b) energy diagram of dielectric effect where the black dotted lines represent the pure dielectric screening effect and the thin blue lines represent the substrate mediated interaction; (c) charge distribution of fully hybridized modes. Reproduced with permission from Ref[35]. Copyright 2011 American Chemical Society.....   | 13 |
| Figure 1.9: FDTD simulations of (A) Scattering spectra of a silver nanocube as it approaches a glass substrate. Field intensities of (B) quadrupolar and (C) dipolar   |    |

|  |    |
|--|----|
| modes. The substrate is represented by the horizontal white line. Reproduced with permission from Ref[33]. Copyright 2005 American Chemical Society. ....  | 13 |
| Figure 1.10: Extinction spectra of AgNCs suspended in ethanol (above) and supported on a PS substrate in air (below). E-field diagrams shown for the multipolar (blue), quadrupolar (green), and dipolar (red) modes. Reproduced with permission from Ref[37]. Copyright 2016 The Royal Society of Chemistry. ....   | 16 |
| Figure 1.11: Extinction spectra of AgNCs as they are progressively embedded into PS. Each stage of embedment is numbered on the right. The blue, green, and red bands denote the shift of the multipolar (M), quadrupolar (Q), and dipolar (D) modes, respectively. Reproduced with permission from Ref[37]. Copyright 2016 The Royal Society of Chemistry.....  | 17 |
| Figure 1.12: Structure of ascorbic acid. ....  | 24 |
| Figure 1.13: Illustration of the two possible routes for Au reduction. Route I is dominated by galvanic exchange whereas Route II is dominated by reduction by AA. Reproduced with permission from Ref[59]. Copyright 2014 American Chemical Society.....  | 24 |
| Figure 1.14: Schematic representation of (A) $\text{TiO}_6$ octahedron of anatase and rutile $\text{TiO}_2$ ; (B) Tetragonal structure of anatase; (C) Tetragonal structure of rutile. Titanium and oxygen atoms are represented by gray and red spheres, respectively. Adapted with permission from Ref[69]. Copyright 2014 American Chemical Society. ....   | 27 |
| Figure 1.15: Schematic illustration of PVP chains integrated into the silica shell that coats an AgNC. The structure of PVP is shown on the right. ....  | 29 |
| Figure 1.16: Crystal structure of $\text{Cu}_2\text{O}$ . Reproduced with permission from Ref[98]. Copyright 2009 WILEY-VCH.....   | 32 |
| Figure 1.17: (A) XRD pattern of a $\text{Cu}_2\text{O}$ coated silver nanowire and (B,C) a schematic representation of the silver and cuprous oxide lattice interface. Brown spheres are the Cu atoms, red spheres are O atoms, and gray spheres are Ag atoms. Reproduced with permission from Ref[99]. Copyright 2014 American Chemical Society. ....   | 33 |
| Figure 1.18: SEM images of $\text{Cu}_2\text{O}$ nanoparticles synthesized with (a-g) increasing amounts of reducing agent and (h) reduced amount of NaOH. Scale bar = $1\mu\text{m}$ . (a) cubes, (b) truncated cubes, (c) cuboctahedra, (d) type I truncated octahedra, (e) type II truncated octahedra, (f) octahedra, (g) short hexapods, and (h) extended hexapods. Reproduced with permission from Ref[106]. Copyright 2009 American Chemical Society..... | 36 |
| Figure 1.19: Structure of lactic acid.....   | 38 |
| Figure 3.2: Extinction spectra of (left) growth of AgNC and (right) quenched AgNC suspended in ethanol. ....   | 47 |
| Figure 3.1: TEM image of silver nanocubes.....   | 47 |
| Figure 3.3: AFM images of (left) a PS thin film and (right) a scratched PS thin film for thickness measurements.....   | 48 |
| Figure 3.4: Left: Extinction spectrum of AgNC on PS thin film. Right: AFM image of the AgNC monolayer on PS.....   | 48 |
| Figure 3.5: Extinction spectra of progression of AgNC embedment into PS. Heating time shown in legend. ....  | 49 |

|  |    |
|--|----|
| Figure 3.6: Apparatus used for method 1.....   | 51 |
| Figure 3.7: Extinction spectra of (left) embedded AgNC before (black) and after (red) reaction and (right) particles removed from substrate and suspended in toluene. Parameters for each sample is described in Table 1. .... | 51 |
| Figure 3.8: TEM images of reacted AgNC from sample (A) Gm1-1; (B) Gm1-2.....   | 52 |
| Figure 3.9: AFM of (A) before and (B) after of reaction on a PS control. Experiment conditions were identical to those of sample Gm1-3.....  | 55 |
| Figure 3.10: Apparatus used for method 2. Syringe pump not pictured.....   | 56 |
| Figure 3.11: Extinction spectra of embedded AgNC before (black) and after (red) reaction. Parameters for each sample is described in Table 2. ....   | 57 |
| Figure 3.12: Extinction spectra of particles removed from substrate and suspended in toluene.....  | 58 |
| Figure 3.13: Extinction spectra of supported AgNC before (black) and after (red) reaction. Parameters for each sample is described in Table 2. ....  | 59 |
| Figure 3.14: Representative TEM image of Au nanocages formed after reaction using method 2. Some AgNCs still present.....  | 59 |
| Figure 3.15: Extinction spectra of embedded AgNC before (black) and after (red) reaction without stirring. Parameters for each sample is described in Table 3.....   | 62 |
| Figure 3.16: Extinction spectra of embedded AgNC before (black) and after (red) reaction with increasing amounts of TTIP.....  | 63 |
| Figure 3.17: AFM images of embedded particles (A) before reaction; (B) after reaction with 3mM TTIP; (C) after reaction with 4mM TTIP. The 3mM TTIP trial is representative of the 1mM-3mM trials. ....                        | 64 |
| Figure 3.18: Extinction spectra of AgNC suspended in toluene before (black) and after (red). Parameters for each sample is described in Table 3. ....  | 65 |
| Figure 3.19: TEM images of samples T6 and T8. ....   | 65 |
| Figure 3.20: Extinction spectra of embedded AgNC before (black) and after (red) reaction with 5mM TTIP. ....   | 66 |
| Figure 3.21: Extinction spectra of embedded particles before (black) and after (red) the silica growth reaction. Parameters for each sample is described in Table 4.....   | 69 |
| Figure 3.22: AFM images of (A) bare AgNC; (B, C) sample S1 after reaction. (B) is a 5 $\mu$ m x 5 $\mu$ m image and (C) is a 2.5 $\mu$ m x 2.5 $\mu$ m image of the same sample.....   | 69 |
| Figure 3.23: Left: Extinction of suspended particles. Right: TEM image of sample S3..  | 70 |
| Figure 3.24: Extinction spectra of embedded particles before (black) and after (red) reaction. Parameters for each sample is described in Table 4. ....  | 72 |
| Figure 3.25: Left: Extinction spectra of particles suspended in toluene. Right: TEM images of samples S7 and S8.....   | 72 |
| Figure 3.26: Extinction spectra of suspended particles before (black) and after (red) reaction.....  | 74 |
| Figure 3.27: TEM images of AgNC/SiO <sub>2</sub> particles. (A) Control; (B) Particles with PDT; (C) Higher magnification, control sample. ....  | 74 |
| Figure 3.28: Extinction spectra of embedded particles before (black) and after (red) reaction. Parameters for each sample is described in Table 4. ....  | 75 |
| Figure 3.29: TEM images of samples S25-S27. ....   | 75 |

|  |    |
|--|----|
| Figure 3.30: Extinction spectra of embedded particles before (black) and after (red) reaction. Parameters for each sample is described in Table 4. ....  | 76 |
| Figure 3.31: Extinction spectra of embedded particles before (black) and after (red) completion of control experiments. Parameters for each sample is described in Table 4.....  | 77 |
| Figure 3.32: FDTD simulation of (left) bare AgNC and (right) AgNC with pyramidal Cu <sub>2</sub> O half-shell.....   | 79 |
| Figure 3.33: E-fields of 60nm AgNC with pyramidal Cu <sub>2</sub> O half-shell for the dipolar and quadrupolar resonances. Top: Particle embedded in PS. Bottom: Particle suspended in solution.....   | 80 |
| Figure 3.34: FDTD simulated extinction of 60nm AgNC with pyramidal Cu <sub>2</sub> O shell with varied AgNC surface coverage. The legend indicates the amount of AgNC covered from the top of the cube (labeled x in the illustration).....  | 81 |
| Figure 3.35: FDTD simulated extinction of 60nm AgNC with cubic Cu <sub>2</sub> O shell of varied thickness. The legend indicates shell thickness (labeled x in the illustration). These spectra are for particles half-way embedded in polystyrene.....  | 82 |
| Figure 3.36: FDTD simulated extinction of 60nm AgNC with cubic Cu <sub>2</sub> O shell of varied thickness. The legend indicates shell thickness (labeled x in the illustration). These spectra are for particles suspended in solution. ....  | 82 |
| Figure 3.37: Extinction spectra of embedded AgNC in PS, before (black) and after (red) reaction.....   | 84 |
| Figure 3.38: Above: TEM images of AgNC/Cu <sub>2</sub> O nanoparticles. Below: Extinction spectra of particles suspended in toluene. Black curve indicates bare AgNC, red curves indicate AgNC/Cu <sub>2</sub> O nanoparticles. (A) 450μL NaOH, LA and 22.5mM Cu(NO <sub>3</sub> ) <sub>2</sub> ; (B) 650μL NaOH, LA and 32.5mM Cu(NO <sub>3</sub> ) <sub>2</sub> ; (C) 850μL NaOH, LA and 42.5mM Cu(NO <sub>3</sub> ) <sub>2</sub> , with the Q mode present at 407 nm and the D mode present at 683 nm.....        | 86 |
| Figure 3.39: Extinction spectra of embedded AgNC before (black) and after (red) reaction. (A) Stepwise Cu(NO <sub>3</sub> ) <sub>2</sub> addition (B) Continuous Cu(NO <sub>3</sub> ) <sub>2</sub> addition, 10mL added at 0.2mL/min (C) Continuous Cu(NO <sub>3</sub> ) <sub>2</sub> addition, 5mL added at 0.1mL/min88   |    |
| Figure 3.40: Above: TEM images of AgNC/Cu <sub>2</sub> O nanoparticles. Below: Extinction spectra of particles suspended in toluene. Black curve indicates bare AgNC, red curves indicate AgNC/Cu <sub>2</sub> O nanoparticles. (A) Stepwise addition of 32.5mM Cu(NO <sub>3</sub> ) <sub>2</sub> , 10mL, 1mL every 5 minutes; (B) Continuous addition of 32.5mM Cu(NO <sub>3</sub> ) <sub>2</sub> , 10mL at 0.2mL/min; (C) Continuous addition of 32.5mM Cu(NO <sub>3</sub> ) <sub>2</sub> , 5mL at 0.2mL/min. .... | 89 |
| Figure 3.41: Extinction spectra of embedded AgNC before (black) and after (red) reaction with and without lactic acid. ....  | 90 |
| Figure 3.42: Above: TEM images of AgNC/Cu <sub>2</sub> O nanoparticles. Below: Extinction spectra of particles suspended in toluene.....   | 91 |
| Figure 3.43: TEM images of AgNC/Cu <sub>2</sub> O particles for the following volumes of each 5M NaOH and 0.5M Cu(NO <sub>3</sub> ) <sub>2</sub> (A) 450μL; (B) 550μL; (C) 650μL; (D) 750μL. (D-1) Cubic morphology; (D-2) Amorphous morphology. ....  | 93 |

|   |     |
|---|-----|
| Figure 3.44: Left: Extinction spectra of Cu <sub>2</sub> O reaction with slow addition of hydrazine without lactic acid, before reaction (black) and after reaction (red). Right: Extinction spectra of particles suspended in toluene. Volume in legend indicates the amount of 5M NaOH and 0.5M Cu(NO <sub>3</sub> ) <sub>2</sub> added. ....             | 94  |
| Figure 3.45: Extinction spectra of embedded AgNC/Cu <sub>2</sub> O particles synthesized with the following volumes of each 5M NaOH, 4M LA, and 0.5M Cu(NO <sub>3</sub> ) <sub>2</sub> (left) 450μL; (right) 650μL. ....  | 95  |
| Figure 3.46: Extinction spectra of suspended AgNC/Cu <sub>2</sub> O particles synthesized with the following volumes of each 5M NaOH, 4M LA, and 0.5M Cu(NO <sub>3</sub> ) <sub>2</sub> (left) 450μL; (right) 650μL. ....   | 95  |
| Figure 3.47: TEM images of AgNC/Cu <sub>2</sub> O particles synthesized with the following volumes of each 5M NaOH, 4M LA, and 0.5M Cu(NO <sub>3</sub> ) <sub>2</sub> (A) 450μL; (B) 650μL. 96  |     |
| Figure 3.48: Extinction spectra of embedded AgNC before (black) and after (red) reaction. Synthesis used ascorbic acid as reducing agent. (A) Without lactic acid; (B) With lactic acid. ....   | 98  |
| Figure 3.49: Above: TEM images of AgNC/Cu <sub>2</sub> O nanoparticles. Below: Extinction spectra of particles suspended in toluene. Black curve indicates bare AgNC, red curves indicate AgNC/Cu <sub>2</sub> O nanoparticles. Synthesis used ascorbic acid as reducing agent. (A) Without lactic acid; (B) With lactic acid. ....                         | 99  |
| Figure 3.50: Extinction spectra of embedded AgNC before (black) and after (red) reaction. Synthesis used hydrazine as reducing agent. (A) CuSO <sub>4</sub> added last, continuously; (B) CuSO <sub>4</sub> added first, quickly; (C) Hydrazine added last, continuously. ....  | 101 |
| Figure 3.51: Above: TEM images of AgNC/Cu <sub>2</sub> O nanoparticles. Below: Extinction spectra of particles suspended in toluene. Black curve indicates bare AgNC, red curves indicate AgNC/Cu <sub>2</sub> O nanoparticles. (A) Reduced with hydrazine, CuSO <sub>4</sub> added first; (B) Reduced with hydrazine, added slowly, with lactic acid. .... | 101 |
| Figure 3.52: Illustration for experiment concept. ....  | 102 |
| Figure 3.53: AFM images of bare AgNCs embedded in PS. The amount of AgNC exposed is (A) 46 nm; (B) 33 nm; (C) 30 nm; (D) 24 nm. ....  | 103 |
| Figure 3.54: Extinction spectra of embedded particles for the 450uL trials before (black) and after (red) Cu <sub>2</sub> O reaction. ....  | 104 |
| Figure 3.55: Extinction spectra of embedded particles for the 650uL trials before (black) and after (red) Cu <sub>2</sub> O reaction. ....  | 104 |
| Figure 3.56: TEM images of AgNC/Cu <sub>2</sub> O particles for (A) least embedded, (B) mid-way embedded, (C) most embedded particles from the 450μL trials. ....   | 105 |
| Figure 3.57: Extinction spectra of 450uL, 22.5mM trials removed from slide, in toluene. ....  | 106 |
| Figure 3.58: Relationship of shell growth and peak splitting with amount of AgNC exposed, 450uL trial. ....   | 106 |
| Figure 3.59: TEM images of AgNC/Cu <sub>2</sub> O particles for (A) least embedded, (B) mid-way embedded, (C) most embedded particles from the 650μL trials. ....   | 107 |
| Figure 3.60: Extinction spectra of 650uL, 32.5mM trials removed from slide, in toluene. ....  | 108 |

|  |     |
|--|-----|
| Figure 3.61: Relationship of shell growth and peak splitting with amount of AgNC exposed, 650uL trial..... | 108 |
|--|-----|

## Abbreviations

- AA – Ascorbic acid  
AFM – Atomic force microscopy  
AgNCs – Silver nanocubes  
CTAB – Cetyltrimethylammonium bromide  
DET – Direct electron transfer  
EDS – Energy-dispersive x-ray spectroscopy  
EG – Ethylene glycol  
GA – Glycoaldehyde  
HSR – Hollow-shell-refilled  
IPA – Isopropanol  
LA – Lactic acid  
LSPR – Localized surface plasmon resonance  
MBA – Mercaptobenzoic acid  
NPs – Nanoparticles  
PIRET – Plasmon-induced resonant energy transfer  
PS – Polystyrene  
PVP – Poly(vinyl)pyrrolidone  
SDS – Sodium dodecyl sulfate  
SERS – Surface-enhanced Raman spectroscopy  
TEM – Transmission electron microscopy  
TEOS – Tetraethyl orthosilicate  
TTIP – Titanium (IV) isopropoxide  
XRD – X-ray diffraction

## 1 Introduction

For many decades, researchers have sought out the synthesis of novel nanoparticles with the intent of creating solutions to existing problems. Anisotropic particles have been top of mind throughout, owing to their nearly endless applications. The objective of this work is the synthesis of morphologically and chemically anisotropic nanoparticles with a distinct core/half-shell morphology. Their synthesis and plasmonic properties are also investigated. The nanoparticles were made up of a silver nanocube core with varied shell materials attempted, of which gold, titania, silica, and cuprous oxide were chosen. The goal is deemed to be achieved if certain properties are satisfied. For particles where the electromagnetic or plasmonic properties are of interest, the objective is considered successful if the half-shell is thick enough to provide a desired electromagnetic or plasmonic response, such is the case for high refractive index shells ( $\text{TiO}_2$ ,  $\text{Cu}_2\text{O}$ ) where in-solution plasmon hybridization is anticipated. For particles that are to be used for directed assembly or regiospecific surface chemistry ( $\text{Au}$ ,  $\text{SiO}_2$ ), the aim of the research is achieved if the half-shells are complete, such that interaction with the core is limited to only one side of the particle.

In this introduction, anisotropic particles and the field of plasmonics will be explained in order to provide an understanding and appreciation of how these novel nanoparticles may contribute to existing knowledge. The embedment process of the silver nanocube core into polymer film will be detailed. This is a key step to achieving this unique particle morphology and provides a widely usable technique from which other core/shell combinations can be created. Following this, the concept and formation of core/shell

particles will be explored with emphasis on the core and shell materials used in this work. Being that the cuprous oxide shell yielded the most significant results, a larger weight is put on this shell material in this thesis.

## 1.1 Anisotropic particles

Anisotropic particles have been studied at great length for their long list of applications in material science. Some of which include their use as self-motile micro-particles,<sup>1</sup> optical sensors,<sup>2</sup> and building blocks for complex nanostructures,<sup>3</sup> amongst many others. Anisotropy can be classified into morphological and chemical anisotropy. Morphological

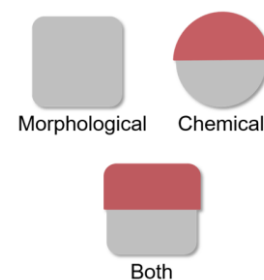


**Figure 1.1:** Schematic illustration of morphological, chemical anisotropy and a particle that carries both

anisotropy pertains to any particle that has asymmetric axes (i.e. non-spherical particles). Chemical anisotropy on the other hand describes particles that have varied chemical composition and surface chemistry.<sup>4</sup> These two types of anisotropy can then be combined to offer greater control of chemistry at the nanoscale, some even allowing multiple chemical reactions to occur on a single particle. Figure 1.1 illustrates a schematic representation of these classifications of anisotropy.

### 1.1.1 Chemical anisotropy

Chemically anisotropic particles come in many forms: Janus,<sup>5</sup> patchy,<sup>6</sup> and multicompartments<sup>7</sup> particles to list a few. There is often a lot of crossover of the terms and definitions of these anisotropic particles. For clarity, each type will be defined in this thesis however it is understood that they are not exhaustive definitions. The term Janus particle was first used by C. Casagrande et al. in 1988 wherein they synthesized silica beads that

each had one hydrophobic hemisphere and one hydrophilic hemisphere achieved through masking and subsequent functionalization.<sup>8</sup> The term was adopted from the two-faced Roman god Janus since these particles contain that same duality. “Janus particle” has most often been used to describe particles that have 50:50 distinct coverage in shape, composition, and chemistry<sup>9</sup> making them very useful given their ability to form size/shape-controlled clusters, their unique surface properties, and their response to stimuli.<sup>10</sup> The three main methods for fabricating these particles are masking, self-assembly, and phase separation.<sup>10</sup> Masking involves blocking off one portion of the nanoparticle surface from reagents leaving the exposed portion available for functionalization. Self-assembly, as the name implies, relies on the spontaneous organization of components. Usually, Janus particles made through this route are composed of block co-polymers and mixtures of ligands. The final method utilizes either the phase separation of two polymers or two inorganic components, or the phase segregation of inorganic material inside or outside a polymer matrix.<sup>10</sup> The seemingly endless variety of Janus particle composition and combination means that their potential uses are limited only by what can be controlled or altered as it pertains to their shape, composition, chemistry, polarity, functionality, electrical and other properties. Some of these applications include self-motile micro-particles,<sup>1</sup> biological sensors,<sup>11</sup> optical sensors,<sup>2</sup> and building blocks for complex structures.<sup>3</sup>

Obtaining the perfect biphasic structure of Janus particles proved difficult and so research shifted towards patchy and multicompartment particles. Patchy particles are those that have surface patterning through which the particle can undergo highly directional

interaction.<sup>6</sup> In general, surface modification techniques are classified under two categories: liquid-phase deposition, and vapour-phase deposition. From the class of liquid-phase deposition, particle lithography has proven effective in patchy particle formation. As for vapour-phase deposition methods, glancing angle deposition has been used. These, in addition to capillary flow techniques, have been successful in the synthesis of these particles. Templating may also be coupled with some of the above techniques to obtain patchiness – as would be the case for liquid-phase deposition. Templating involves the following steps: 1) partial covering of the particle surface with a

template; 2) exposed areas interact with reagents and the surface is modified; 3) the template is removed.<sup>6</sup> When using capillary flow techniques for patchy particle formation, microfluidics is often a method that is exploited.<sup>6</sup> Microfluidics involve the movement of fluid using capillary forces through microchannels.<sup>12</sup> By utilizing multiple channels with specific placement, the reagents can be introduced such that biphasic or ternary particles can be made (Figure 1.2).<sup>13</sup> Glancing angle deposition is a method wherein vapour-phase deposition is performed at an inclined angle in relation to the monolayer plane, resulting in

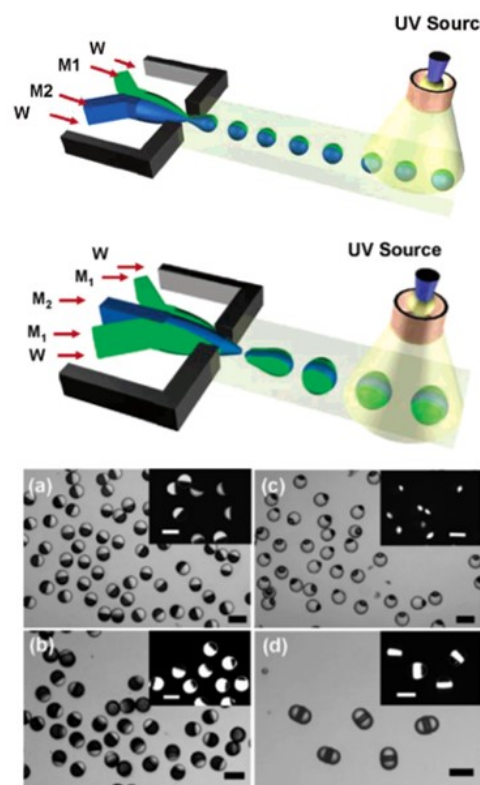


**Figure 1.2:** Above: Schematic of biphasic particle formation. Middle: Schematic of ternary-structure particle formation. Both using microfluidics. M1 and M2 denote immiscible monomers and W indicates the emulsifier. Below: Optical microscopy of (a-c) Biphasic particles, (d) Ternary-structure particles. Insets show fluorescence microscopy of particles. Adapted with permission from Ref[13] Copyright 2006 American Chemical Society.

particles within the same monolayer acting as shadow masks for adjacent particles.<sup>6</sup> Particle lithography is a liquid-phase deposition-based method that uses individual particles for site-specific patterning (Figure 1.3).<sup>14</sup> Patchy particles induce directionality in assembly processes. This therefore lends to the potential of these patchy particles to serve in field-induced assembly and supramolecular assembly.<sup>6</sup>

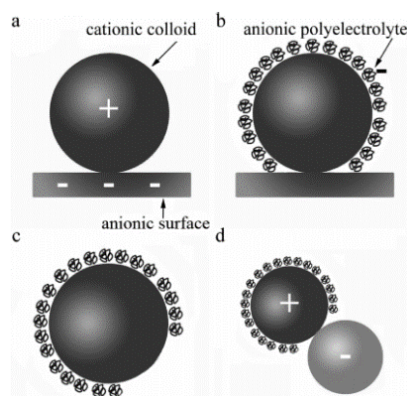


**Figure 1.3:** Schematic of the particle lithography method. (a) Cationic particle adhered to an anionic substrate. (b) Anionic polyelectrolyte interacts with the accessible portion of the colloid. (c) Particle is removed from substrate. (d) Selective interaction with an anionic particle. Reproduced with permission from Ref [14]. Copyright 2005 American Chemical Society.

Multicompartment particles are a class of particles that are composed of multiple phase-separated domains.<sup>9</sup> This type of particle is often produced using hydrocarbon-fluorocarbon hybrid systems or block terpolymers.<sup>9</sup> Additionally, multiblock copolymers have been used in conjunction with other materials, such as silica, to form these multicompartment particles.<sup>15</sup>

Particles can also have a mix of the above types, combining patchiness with Janus or multicompartment particles and resulting in bi- or multi-phasic particles with functionalized surface sections which then lends itself to a whole array of possible applications.<sup>9</sup> It is important to note that these chemically anisotropic particles are typically in the micron scale and there exist significant difficulties in synthesizing these particles on

the nano scale (<100 nm) with inorganic materials.<sup>9</sup> In this work, it will be shown that a straightforward technique for synthesizing nanoparticles with chemical anisotropy has been achieved.

### **1.1.2 Morphological anisotropy**

As briefly explained above, morphologically anisotropic particles are those that have asymmetric axes.<sup>4</sup> A few examples of these are rods, cubes, triangular prisms, and disks. There are a wide variety of synthesis techniques that exist for creating particles with morphological anisotropy. The approaches of seed-mediated growth and templating will be described in this work.

Traditionally, a one-pot approach is used for colloidal metal nanocrystal synthesis wherein homogeneous nucleation and seed-mediated growth take place simultaneously. However, these two competing processes typically result in polydispersity, varied shape, and crystallinity.<sup>16</sup> This therefore led to the need for separating nucleation from the seeded growth steps, thus utilizing heterogeneous nucleation. Homogeneous and heterogeneous nucleation differ in that the former is a self-nucleation that generate nuclei and the latter involves the deposition of atoms onto an existing seed surface.<sup>16</sup> In heterogeneous nucleation, the atoms will interact with preferential sites (e.g. phase boundaries, impurities), meaning the areas where the effective surface energy is lower and as such the activation energy is also lower. This therefore results in a more probable growth route than homogeneous nucleation.<sup>17</sup> The seed-mediated growth technique involves preformed seeds with well-defined attributes that are exposed to a supersaturated solution, resulting in further growth into nanocrystals of specific shape and size.<sup>16</sup> In the case of single-crystal

seeds, octahedra, octagonal rods, cubes, rectangular bars, or cuboctahedra are formed. If singly twinned seeds are present, right bipyramids are grown, whereas if multiply twinned seeds are used decahedra, icosahedra, and penta-twinned rods are synthesized. Triangular or hexagonal plates are made if the seeds have stacking faults.<sup>18</sup> Figure 1.4 shows a schematic illustration of pathways from varied seed structures to their respective anisotropic nanostructures.

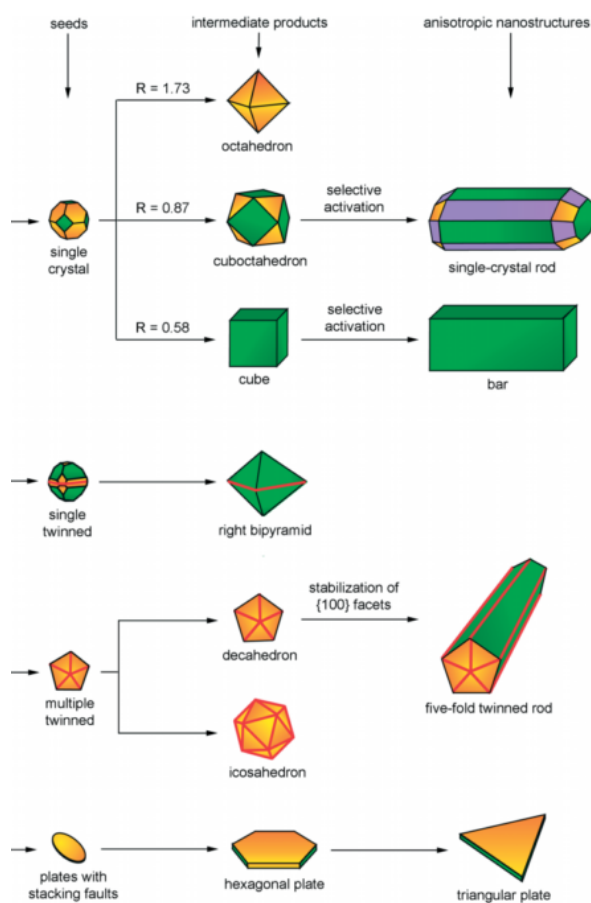


**Figure 1.4:** Schematic illustration of pathways from varied seed structures to their respective anisotropic nanostructures. The  $\{100\}$ ,  $\{110\}$ , and  $\{111\}$  facets are shown in green, purple, and orange, respectively. The parameter  $R$  represents the ratio between the growth rates in the  $[100]$  and  $[111]$  directions. Reproduced with permission from Ref[19]. Copyright 2007 Wiley-VCH.

Templated synthesis, using soft or hard templates, can be used for the formation of morphologically anisotropic particles by encouraging shape specificity and once again

exploiting heterogeneous nucleation. Hard templates can be rigid nanostructures within which the anisotropic particles are grown; for example, using a porous membrane as a template.<sup>20</sup> The anisotropic particles can also be grown on the outside of the rigid template. Such is the case of core/shell particles containing anisotropic cores.<sup>4</sup> As for soft templates, typically microemulsions or micelles are used by utilizing the solubility differences of the precursor and monomers between the emulsion droplet or micelle and the surrounding matrix.<sup>4</sup> While these templates are often isotropic in shape, nanorods have been successfully synthesized with this method. This anisotropic growth occurs because the precursor has higher solubility in the emulsion droplets resulting in a one-sided supply of reagents and thus forcing the particle to grow in only one direction.<sup>21</sup>

A significant attribute of these morphologically anisotropic particles is the potential for regiospecific surface chemistry.<sup>4</sup> Since many of these particles have different crystal facets exposed at different areas on the same particle, their varied reactivities can be exploited for specific functionalization.<sup>22</sup>

### **1.1.3 Combining the two anisotropies**

Many anisotropic particles have a combination of both types of anisotropy, offering a wide array of applications. Janus particles can have both anisotropies; for example, a rod that has length-ways chemical division.<sup>5</sup> The type of particles proposed in this research exhibit this dual anisotropy on the nano scale. By combining a silver nanocube core with a metal or oxide Janus-like half-shell, the door to new applications is opened. For shell materials of a high-refractive index, it is possible to obtain in-solution hybridization of the plasmon modes. Additionally, the exposed core or the shell could be selectively

functionalized leading to usefulness in directed assembly and regiospecific surface chemistry. This would as well be a key component of reliable dimer formation for the creation of hot-spots that would be useful for SERS sensing. Due to their similarity with core/shell particles, the proposed research will use the term core/half-shell nanoparticles to designate these new particles.

There are only a few existing instances of this inorganic core/half-shell morphology and of them, only gold cores with polymer, palladium, or silica shells have been synthesized.<sup>23, 24, 25, 26, 27, 28</sup> This work provides a reliable method for the formation of these types of particles which could be applied to any number of core and shell compositions. In this thesis, silver nanocube cores have been tested with gold, titania, silica, and cuprous oxide half-shells.

## 1.2 Plasmonics

Plasmonics is the study of the interaction between an electromagnetic field and free electrons in a metal wherein plasmon resonance is the collective oscillation of electrons in the conduction band of a metal. This oscillation is induced by the alternating electric field in electromagnetic waves where the wave's depth of penetration on a metal surface is less than 50 nm (for Ag). Here, only

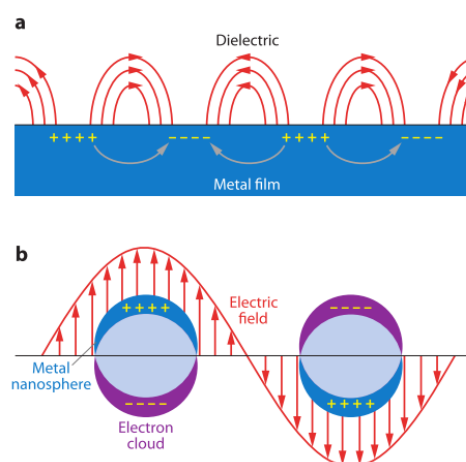
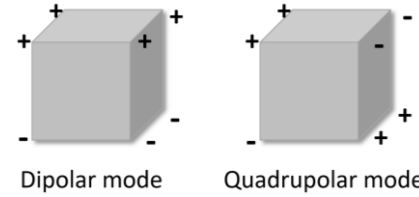


**Figure 1.5:** Schematic illustrations of (a) propagating surface plasmons along a metal film and (b) localized surface plasmons for a metal nanosphere. Reproduced with permission from Ref[29]. Copyright 2009 American Chemical Society.

the plasmons from the surface electrons, referred to as surface plasmons, are excited.<sup>29</sup> The

two types of surface plasmons are propagating surface plasmons, where the plasmons occur along an extended metal, and localized surface plasmons, that deal with the oscillations of the electrons



Dipolar mode      Quadrupolar mode  
**Figure 1.6:** Illustration of the dipolar and quadrupolar modes of a silver nanocube.

confined within a metal nanoparticle that is smaller than the wavelength of the incident light (Figure 1.5). Localized surface plasmons are of importance in this study. A dipole is created when the electric field causes the electrons to move collectively in one direction. This dipole can change direction with the change in electric field. This oscillation will be in resonance with the incident light at a particular excitation frequency. This will result in a strong electron oscillation. This resonance condition is called localized surface plasmon resonance (LSPR). Larger particles (diameters or edge lengths greater than 30 nm) can present higher order modes, such as quadrupolar plasmon resonance (Figure 1.6). This occurs when there are two negatively charged poles and two positively charged poles.<sup>29</sup>

The dielectric function of a metal nanoparticle will determine whether it will support surface plasmon resonance. The dielectric function,  $\epsilon$ , includes an imaginary part  $\epsilon_i$  and a real part  $\epsilon_r$  and both will change with the excitation wavelength,  $\lambda$ , of incident light.<sup>30</sup> The following formula from Mie theory provides a simple description of LSPRs through the calculation of the extinction cross section,  $C_{ext}$ , of a metal nanosphere:<sup>31</sup>

$$C_{ext} = \frac{24\pi^2 R^3 \epsilon_m^{3/2}}{\lambda} \left[ \frac{\epsilon_i}{(\epsilon_r + 2\epsilon_m)^2 + \epsilon_i^2} \right] \quad (1.1)$$

Here,  $R$  is the particle radius and  $\epsilon_m$  is the dielectric constant of the medium surrounding the particle. In order to have a large  $C_{ext}$ , the resonance condition must be satisfied. This means that  $\epsilon_r$  must be close to  $-2\epsilon_m$  so that the denominator of the bracketed expression

approaches zero.<sup>30</sup> Therefore, materials that have a negative  $\epsilon_r$  and a small positive  $\epsilon_i$  will be able to support surface plasmon resonance.<sup>32</sup> For standard dielectrics and non-metals, this is not possible. Figure 1.7 shows the plots for the real and imaginary parts of the dielectric function of silver, gold, and silicon. Si is representative of other non-metals in that it has large positive values for  $\epsilon_r$ .<sup>30</sup>

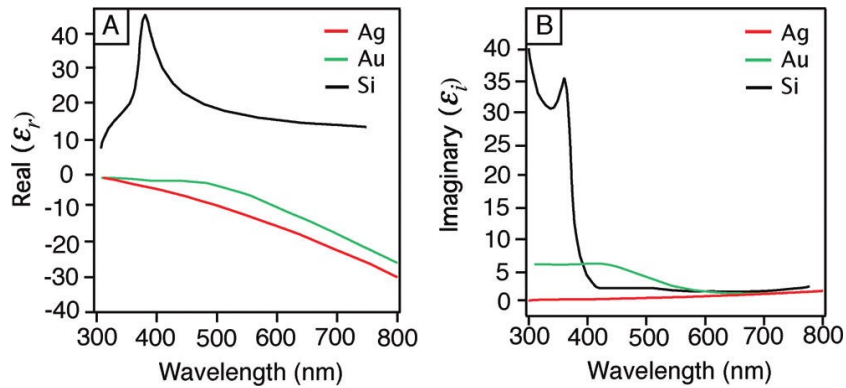


**Figure 1.7:** Plot of (A) the real and (B) the imaginary parts of the dielectric function of silver, gold, and silicon with respect to wavelength. Reproduced with permission from Ref[30]. Copyright 2011 American Chemical Society.

The plasmonic response of these nanoparticles are also extremely sensitive to their local environment since the LSPR extinction wavelength maximum,  $\lambda_{\max}$ , is sensitive to the dielectric constant,  $\epsilon$ , or refractive index,  $n$ , where  $\epsilon = n^2$ . Therefore, if the local environment changes then the  $\lambda_{\max}$  will shift. The following applies to the presence of an adsorbed species onto the nanoparticle.<sup>32</sup>

$$\Delta\lambda_{\max} = m\Delta n[1 - e^{(-2d/l_d)}] \quad (1.2)$$

Where  $m$  is the bulk refractive index response of the nanoparticles,  $\Delta n$  is the change in refractive index as a result of the adsorbate,  $d$  is the effective adsorbate layer thickness, and  $l_d$  is the EM-field decay length.<sup>32</sup>

Beyond just having a  $\lambda_{\max}$  shift when an adsorbate species is present on the surface of the nanoparticle, more dramatic changes can occur when a particle is supported on a

dielectric substrate. When a nanocube is suspended in solution it exhibits primarily one dipolar mode. However, when this cube approaches a dielectric substrate, the existing dipolar mode becomes red-shifted and a new peak emerges at a higher energy (Figure 1.9A).<sup>33</sup> The particle's anisotropic environment induces symmetry-breaking and results in a system that introduces coupling of dark and bright modes.<sup>34, 35</sup> A bright mode is one that can be excited by light because of the dipole moment generated upon exposure to light. It can be probed and observed through UV-vis spectrometry. A dark mode is one where the overall dipole vanishes and cannot be directly excited by a planar electromagnetic wave. The intrinsic plasmonic modes that are relevant in the case of nanocubes are the dipolar  $D^0$ , the bright mode, and the quadrupolar  $Q^0$ , the dark mode. Their interaction can be described by plasmon hybridization, which can be represented analogously to molecular orbital theory. The intrinsic modes will interact to form the bonding mode ( $D = D^0 + Q^0$ ) and the antibonding mode ( $Q = D^0 - Q^0$ ).<sup>35</sup> Figure 1.8 illustrates the substrate-mediated hybridization of the  $D^0$  and  $Q^0$  modes. In Figure 1.8A, the  $D^0$  and  $Q^0$  modes are shown as being mediated by the dielectric. Figure 1.8B shows an energy diagram that qualitatively explains how the bonding  $D$  and antibonding  $Q$  modes are formed from the substrate-mediated interaction. Figure 1.8C provides the charge distribution of fully hybridized modes and highlights the spatial separation of the bonding  $D$  and antibonding  $Q$  modes. It should be noted that this figure assumes perfect mixing of the modes. The distance from the dielectric and the dielectric constant will dictate the degree of mixing. The dielectric constant,  $\epsilon_s$ , of the substrate will affect the nanoparticle's plasmon resonance as  $(\epsilon_s - 1)/(\epsilon_s + 1)$ , thus with a larger dielectric constant the interaction increases.<sup>35</sup>

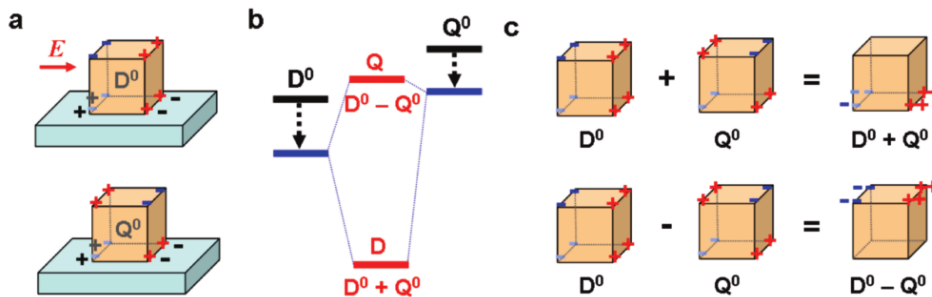


**Figure 1.8:** Schematic illustration of (a) intrinsic cube modes with induced hybridization from the dielectric; (b) energy diagram of dielectric effect where the black dotted lines represent the pure dielectric screening effect and the thin blue lines represent the substrate mediated interaction; (c) charge distribution of fully hybridized modes. Reproduced with permission from Ref[35]. Copyright 2011 American Chemical Society.

The change in interaction with change in distance is observed in the finite difference time domain simulated scattering in Figure 1.9A. As the nanocube approaches the glass substrate, the dipolar and the quadrupolar modes become more resolved.<sup>30,36</sup> Also shown are the field intensities of the hybrid quadrupolar (Q) mode and the dipolar (D) mode where the white horizontal line represents the substrate (Figure 1.9B, C).<sup>33</sup> These modes are spatially separated on the nanocube. The D mode is oriented toward the substrate (area of higher refractive index) and the higher energy mode, the Q mode, is oriented toward the superstrate (area of lower refractive index).<sup>35, 33</sup>

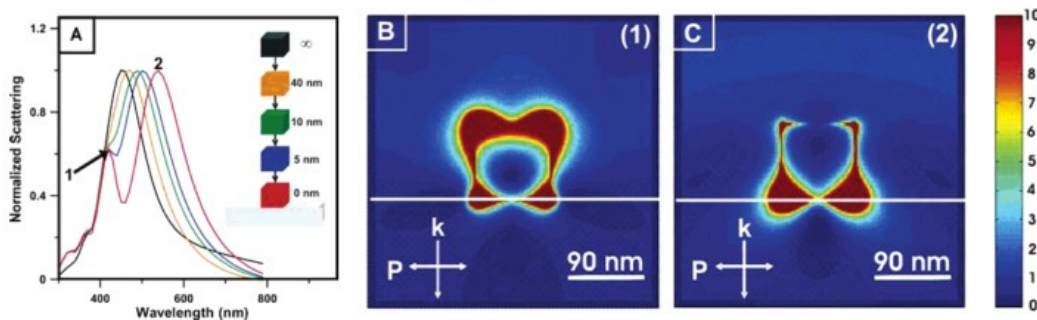


**Figure 1.9:** FDTD simulations of (A) Scattering spectra of a silver nanocube as it approaches a glass substrate. Field intensities of (B) quadrupolar and (C) dipolar modes. The substrate is represented by the horizontal white line. Reproduced with permission from Ref[33]. Copyright 2005 American Chemical Society.

The concept of substrate-induced hybridization is relevant to this thesis because dielectric half-shells could act in place of a dielectric substrate and provide in-solution plasmon hybridization, creating a new avenue to exploit their valuable optical properties.

### 1.3 Embedment of silver nanocubes into polymer thin films

The embedment of AgNCs into a polymer film is one of the key intermediate steps for our half-shell synthesis technique. The AgNC are first deposited onto the surface of a polystyrene (PS) film using Langmuir-Schaeffer deposition and are then gradually embedded into the PS film via heating until a desired depth is achieved. The fine-tuning and understanding of the embedment process of AgNC in polystyrene was recently completed by our group.<sup>37, 38, 39</sup>

Deak et al. also utilized polystyrene as a mask for their gold/silica “mushroom” particles, however they casted a mixed solution of PS and nanoparticles (NP) via spin coating. They controlled the degree of particle coverage by optimizing the concentration of polystyrene in their casting solution and the spin speed.<sup>23</sup> This method provides little control over the embedment depth and interparticle spacing. There is also the concern that an ultra thin film of PS coats the exposed surface of the particle. By using a two-step process of particle deposition then subsequent embedding, instead of a casted PS/NP mix, the depth of embedment can be well controlled.

Utilizing a polymer as a substrate and sacrificial template is useful due to the polymer’s ability to change from a hard “glassy” state to a more viscous and rubbery one by simply applying heat. This phenomenon is called *glass transition* and occurs at a polymer’s *glass transition temperature* ( $T_g$ ).<sup>40</sup> In this work, the polymer in question is polystyrene. This polymer is suitable for our purposes since its  $T_g$  of 100-110°C<sup>41</sup> is lower than the temperature at which the AgNC starts to breakdown (~150°C). As the polymer is heated to its  $T_g$ , the polymer chains are more mobile, allowing them to flow around the

embedding particle. Not only does the polymer have to be at its  $T_g$  for a particle to embed but the surface energy argument must also be satisfied. This can be modeled using Helmholtz free energy. The embedment driving force, determined by Kovacs et al., is described by the decrease in free energy of the system.<sup>42</sup> If we consider a single rigid particle on a flexible polymer, where the particle of surface area  $a$ , with surface tension  $\gamma_p$ , is above the polymer surface with tension  $\gamma_s$ , and together they have the interfacial tension of  $\gamma_{ps}$ , then the Helmholtz surface free energy  $\Delta A_s$  is:<sup>42</sup>

$$\Delta A_s = a(\gamma_{ps} - \gamma_p) \quad (1.3)$$

Embedment will occur if  $\Delta A_s < 0$  (and  $T > T_g$ ), thereby satisfying:

$$\gamma_p > \gamma_{ps} \quad (1.4)$$

The above inequality only applies to the requirements that particles need to overcome to begin embedding. Another inequality must be satisfied for the particle to become fully incorporated and that is expressed as:

$$\gamma_p > \gamma_{ps} + \gamma_s \quad (1.5)$$

This is explained as the free energy of the particle being greater than that of the interfacial energy and the free energy of the surface combined.<sup>42</sup> The AgNCs used in this work were passivated with poly(vinylpyrrolidone) (PVP) thus the surface energy used in the above must be that of PVP ( $\sim 43 \text{ mJ/m}^2$ ).<sup>43</sup> Since the surface free energy of polystyrene is lower at  $33 \text{ mJ/m}^2$ ,<sup>44</sup> then the particles will begin to embed.

A method was developed to controllably embed AgNCs into PS through monitoring of the plasmonic modes via UV-vis spectroscopy.<sup>37</sup> AgNCs of 60-65nm edge length supported on a PS film will exhibit three distinct extinction peaks. The lowest wavelength peak at approximately 340nm corresponds to the multipolar mode (M). The other two

higher wavelength peaks are the hybrid quadrupolar (Q) at  $\sim 390\text{nm}$  and hybrid dipolar modes (D) at  $\sim 450\text{nm}$ . The plasmonic modes of AgNCs supported on high refractive index substrates are spatially separated; namely, the D mode is localized toward the area of higher refractive index – in this case PS – and the Q mode is localized toward the area of lower refractive index, ie. the air (Figure 1.10).<sup>37, 39</sup>

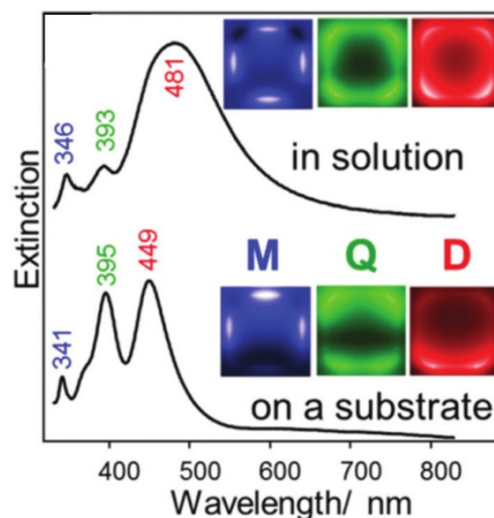


**Figure 1.10:** Extinction spectra of AgNCs suspended in ethanol (above) and supported on a PS substrate in air (below). E-field diagrams shown for the multipolar (blue), quadrupolar (green), and dipolar (red) modes. Reproduced with permission from Ref[37]. Copyright 2016 The Royal Society of Chemistry.

Due to this spatial separation of the plasmonic modes, the wavelength shift of each mode will occur at different embedment stages and is shown in Figure 1.11. As the cubes embed, the refractive index of the local environment increases and is observed as a red-shifting of the peaks.<sup>39</sup> In stages 1 and 2 of Figure 1.11, the cubes are embedded until nearly halfway. Since the D mode is localized toward the PS, it will exhibit a significant red shift from approximately  $450\text{nm}$  to  $480\text{nm}$ . In the multipolar region, a second peak appears at around  $350\text{nm}$ . The Q mode red shifts by only a few nanometers. In stage 3, the cubes experience some tilting on either an edge or corner. Spectrally, the D mode reaches a maximum shift just above  $480\text{nm}$  and the Q mode red shifts the most to around  $410\text{nm}$ . The M mode at  $350\text{nm}$  dominates and the  $340\text{nm}$  peak depletes. In stage 4, the M and D modes do not change and the Q mode continues to red shift until it is obscured by the D mode peak.<sup>37</sup> This Q and D mode overlap represents a near-isotropic environment.<sup>39</sup> It is

at this point that nearly all of the particles are submerged and only one corner of each cube is exposed at the surface.<sup>37</sup> With the above knowledge, the embedment process can be stopped at any desired point.

#### 1.4 Core/shell particles

Core/shell nanoparticles are defined as those having an inner material and an outer layer material and can have any mix of inorganic or organic components as well as any size and shape. The choice of materials is

dependent on the desired application. These particles are highly functional materials whose properties – that arise from either the core or the shell material – can be extremely varied; for example, reactivity, stability, and dispersibility. For this reason, the purpose of the shell could be for surface modification, controlled release of the core, reduced consumption of a precious material, etc. Shells can also become hollow nanoparticles by removing the core, which could be useful as microvessels.<sup>45</sup>

The synthesis methods of these particles are divided by either “top-down” or “bottom-up” approaches. “Top-down” involves microfabrication techniques such as cutting, milling, and shaping materials. “Bottom-up” involves the self-assembly of molecules by exploiting their chemical properties. This approach allows for much smaller particles to be produced compared to the “top-down” approach.<sup>45</sup> An important concept in

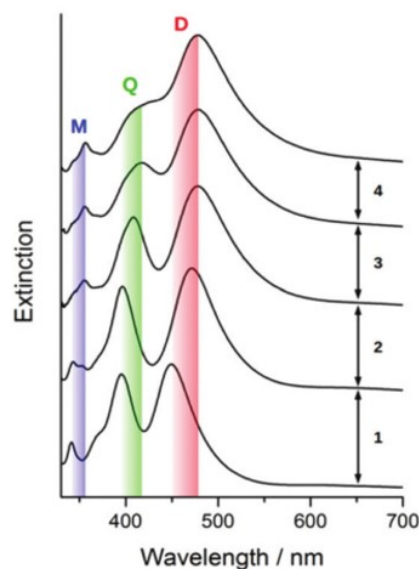


**Figure 1.11:** Extinction spectra of AgNCs as they are progressively embedded into PS. Each stage of embedment is numbered on the right. The blue, green, and red bands denote the shift of the multipolar (M), quadrupolar (Q), and dipolar (D) modes, respectively. Reproduced with permission from Ref[37]. Copyright 2016 The Royal Society of Chemistry.

the “bottom-up” approach is heterogeneous growth, where growth occurs on the existing surface of a compound of different composition/material. Heterogeneous growth occurs preferentially because the energy barrier required for growth to start is lower than that of homogeneous growth.<sup>16</sup> However, homogeneous growth will still occur if concentrations surpass a certain threshold.<sup>46</sup>

This section will explore the synthesis and properties of the silver nanocube core as well as the growth mechanism and purpose of each shell material tested.

#### **1.4.1 Silver nanocube core**

Silver is a desirable material for this study due to its strong plasmonic properties. It is known to support strong surface plasmons in the visible and near-infrared regions, from 300 to 1200 nm. Nanocubes are desirable since their shape supports higher order modes at smaller sizes and they have a higher contact area with the substrate.<sup>30</sup> These attributes make it viable for LSPR sensing,<sup>30</sup> SERS sensing,<sup>30</sup> and as a plasmonic sensitizer for photocatalysis.<sup>47</sup>

Employing silver nanocubes as LSPR sensors can be done through many avenues, be it through changing the dielectric environment, observing structural change with time and temperature, coupling resonant molecules to the resonance frequency of the AgNC, or the manipulation of distance-dependent coupling. These sensors are typically based on a measured shift of the LSPR. By changing the dielectric environment, such as with an analyte molecule, the resonance frequency of the LSPR will shift; this is the detectable response.<sup>30</sup> The structural change of a nanostructure is also a detectable alteration since time and temperature will affect the higher energy surfaces of the nanostructure and cause

an LSPR shift; for example, rounding of AgNC corners with exposure to air over time resulting in a loss of the cubes' LSPRs.<sup>48</sup> This will also cause a colour change that can be visible to the naked eye.<sup>30</sup> An LSPR sensor with increased sensitivity can be made by coupling a resonant molecule to the resonance frequency of a nanostructure. When there is a spectral overlap of the two resonances, the magnitude of the LSPR peak shift increases.<sup>49</sup> The final LSPR sensor here is accomplished through distance-dependent coupling between nanoparticles. In this case, nanoparticles are modified with proteins or ligands that will force their aggregation. This aggregation will result in LSPR shifts that are dependent on the distance between the particles. These sensors are often called plasmon rulers.<sup>50</sup>

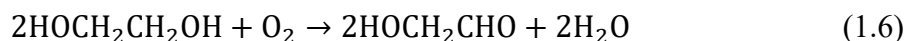
Using AgNC as SERS sensors is different to LSPR sensing in that it is the enhanced E-fields near plasmonic nanostructure surfaces that are exploited. This technique can also provide the identity of the molecule in question since SERS measures the unique vibrational spectrum of a molecule, called a Raman fingerprint. These enhanced E-fields can dramatically increase the Raman scattering of molecules in their vicinity, with measured enhancements ranging from  $10^4$ - $10^{15}$ .<sup>51</sup> It is also possible to obtain single molecule detection with this method through the use of dimers of plasmonic nanoparticles.<sup>30</sup> Two mechanisms occur that provide the significant enhancement of the SERS signal and those are electromagnetic enhancement and chemical enhancement. The electromagnetic enhancement, which contributes the most to the total enhancement, arises from the LSPR modes that focus light into nanosized volumes. This increases the intensity of the E-field around the nanoparticle. Nanoparticle dimers and nanostructures with sharp features are strong candidates for light focusing. The chemical enhancement, on the other

hand, comes from the interactions between the molecule and the nanoparticle that leads to resonant enhancement from molecular excitations or charge transfers.<sup>30</sup> The choice of AgNCs for this thesis is due to the fact that silver exhibits higher enhancement than other metals (e.g. higher than gold and copper)<sup>51</sup> and cubes provide stronger SERS signals (particularly when compared to spheres).<sup>52</sup>

Silver nanoparticles have also been used as plasmon sensitizers for photocatalysis. Metal oxide semiconductors are often used as photocatalysts; however, they have wide band gaps, limiting their light absorption to a small spectral region. In order to expand this usable spectral region, photosensitizers have been developed (e.g. organic dyes, inorganic quantum dots), although there have been issues with their stability. Traditionally, these sensitizers work based on excited electrons relaxing to the band edge followed by a transfer to the semiconductor in a process called thermalized electron transfer and requires energetically favourable band alignment.<sup>47</sup> More recently, plasmon sensitizers have been studied since their plasmon oscillations have a broad resonance and short lifetime. This permits significantly different energy transfer processes, such as energy transfer through nonradiative coupling of the metal and semiconductor. In this type of photocatalyst, the electron-hole pair in the semiconductor is formed from the transfer of photoexcited plasmonic energy from the metal to the semiconductor. In particular, this has been shown to occur for Ag/Cu<sub>2</sub>O core/shell nanoparticles.<sup>47</sup>

The formation of silver nanocubes (AgNCs) can be accomplished via the sulfur-mediated polyol synthesis wherein AgNO<sub>3</sub> is the precursor, ethylene glycol (EG) is the reducing agent, poly(vinyl)pyrrolidone (PVP) is the capping agent, NaCl is an etchant, and

Na<sub>2</sub>S act as a catalyst.<sup>30</sup> In this synthesis, the primary reducing agent, glycoaldehyde (GA), forms in the presence of O<sub>2</sub> when EG is heated.<sup>30,54</sup>



The reduction of the silver cations forms highly reactive nuclei. As these nuclei grow, they stabilize and three dominant structures emerge: single crystalline, singly twinned, and multiply twinned. Nanocubes are formed from single crystalline seeds. To encourage only single crystalline seeds, Cl<sup>-</sup> in conjunction with O<sub>2</sub> is utilized. The chloride and oxygen pair will etch and dissolve the multiply and singly twinned seeds.<sup>30</sup> This oxidative etching and dissolution occurs primarily to the twinned seeds because they have higher activity and reactivity than the single crystalline morphology. The active sites for oxidative dissolution are present in the form of defects in the twinned particles. Since single crystalline structures do not have these defects, they are not dissolved and remain to form cubes.<sup>55</sup> Another ion impacting the polyol system is S<sup>2-</sup>. It increases the reduction rate of AgNO<sub>3</sub>, making large scale production easier. The Ag<sub>2</sub>S that forms immediately from the interaction between Na<sub>2</sub>S and AgNO<sub>3</sub> serves as a seed for further growth, nucleating the formation of silver nanostructures. Na<sub>2</sub>S forces single crystalline morphology since the reaction is too fast to allow the formation of twin defects.<sup>31, 54</sup>

Another factor affecting the final morphology of the nanocrystal is PVP. The resulting cubes are capped by {100} faces due to favourable binding energy of PVP to the Ag(100) surface.<sup>30</sup> The {100} facets are tightly passivated and stabilized by PVP through chemical adsorption with the oxygen in the pyrrolidone (Figure 1.15). The other facets, such as the {111} facets, remain uncovered by PVP and are therefore available for

continuous reaction and growth with the silver atoms through Ostwald ripening.<sup>56</sup> These truncated silver nanocubes have a face-centered cubic crystal lattice with the {100}, {110}, and {111} facets exposed at the faces, edges, and corners of the nanocube, respectively.<sup>57</sup>

#### 1.4.2 Gold shell

The choice of a gold shell was based on the possibility of an improved biological SERS sensor. The toxicity of the  $\text{Ag}^+$  ion limits the AgNC's biological applications even though coupled AgNCs have strong electromagnetic field enhancements which make them ideal for SERS detection and imaging.<sup>58</sup> Gold's biocompatibility and stronger adsorption with SERS probes makes its pairing with AgNC desirable.<sup>59</sup> The half-shell morphology of the particle allows for the unencumbered coupling of AgNCs for signal enhancement. Otherwise, it could be further exploited to grow a secondary shell on the remaining exposed silver.

Typically, the interaction of gold ions with silver metal results in galvanic replacement. Galvanic replacement (or galvanic exchange) is an electrochemical process wherein there occurs the oxidation of one metal – the “sacrificial template” – by another having a higher reduction potential. When the two metals come in contact within a solution phase, the sacrificial metal is oxidized and subsequently dissolved into solution while the ions of the second metal are reduced onto the outer surface of the template. For this reaction to occur, there only requires a sufficient difference in reduction potential of two metals.<sup>60</sup> While this technique is extremely useful for the formation of hollow particles, it is detrimental to the successful synthesis of Ag/Au core/shell nanoparticles since a galvanic reaction will spontaneously occur when silver nanoparticles are immersed in an aqueous

HAuCl<sub>4</sub> solution. There have, however, been a few attempts at gold coated silver through the retardation of the galvanic reaction, namely by Kitaev et al.,<sup>61</sup> Mirkin et al.,<sup>62</sup> Xue et al.,<sup>63</sup> and Yin et al.<sup>64</sup> Kitaev et al. used a slow injection of a dilute HAuCl<sub>4</sub> solution over a period of 12 hours to form uniform layers of Au on Ag nanoparticles. However, the presence of conformal shells was not proven.<sup>61</sup> Mirkin et al. used ascorbic acid (reducing agent) and cetyltrimethylammonium bromide (capping agent) for the deposition of Au onto Ag nanoprisms, yet they still saw the occurrence of galvanic exchange on the corners of the nanoprisms.<sup>62</sup> Xue et al. used hydroxylamine as the reducing agent for the synthesis of Au-coated Ag-Au alloy nanoprisms. While galvanic replacement still occurred in this case, the dissolved Ag<sup>+</sup> ions were reduced back onto the nanoprisms by the hydroxylamine.<sup>63</sup> Finally, Yin et al. decreased the reduction potential of the Au<sup>3+</sup> ions through complexation with I<sup>-</sup> ions, although there was still the formation of small voids due to galvanic exchange taking place.<sup>64</sup>

Recently, Dong et al. were able to coat Ag nanocubes with ultrathin layers of Au through a fast parallel reduction of HAuCl<sub>4</sub> by ascorbic acid (AA) and an optimization of the pH with NaOH.<sup>59</sup> By having a competing reducing agent, in this case ascorbic acid (Figure 1.12), two separate reduction pathways are formed: one which is governed by the reduction rate of ascorbic acid and the other by the reduction rate of silver. Figure 1.13 illustrates these two reduction pathways. The reduction by Ag, with its rate labeled  $R_{gal}$ , since it is driven by a galvanic reaction, will produce hollow Au-Ag structures. Meanwhile, the reduction by AA, with a rate of  $R_{red}$ , will result in the epitaxial growth of Au on the

AgNPs. The dominant reduction rate is controlled by pH. When the pH is low,  $R_{gal}$  reigns, whereas when the pH is high,  $R_{red}$  governs. The reduction of  $Au^{3+}$  to  $Au^+$

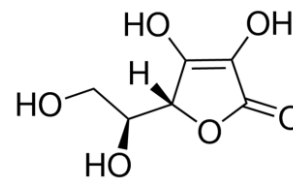


Figure 1.12: Structure of ascorbic acid.

by AA is fast but, at low pH, the further reduction of  $Au^+$  to  $Au^0$  is very slow.<sup>65</sup> As the pH is increased the reducing ability of AA increases.<sup>66</sup> To elaborate on this, ascorbic acid is a weak diprotic acid with  $pK_{a1} = 4.2$  and  $pK_{a2} = 11.6$ , at 25°C, and it is actually the ascorbate monoanion ( $AscH^-$ ) that can effectively donate electrons, thereby acting as the reductant instead of the parent ascorbic acid.<sup>67</sup> In this system, NaOH becomes important because adding  $OH^-$  to ascorbic acid will facilitate the dissociation of AA to form more  $AscH^-$ , thereby increasing  $R_{red}$ .<sup>68</sup> Additionally,  $AuCl_4^-$  can interact with  $OH^-$  to form  $Au(OH)_4^-$ , resulting in the decrease of the reduction potential of the Au(III) precursor. This slows down both reduction pathways.<sup>68</sup> Finally, as the Ag is oxidized to  $Ag^+$ , the  $OH^-$  can interact with the cation to form  $Ag_2O$  which is insoluble in alkaline solutions. The  $Ag_2O$  that gets deposited onto the AgNP can act as a mediator to the further dissolution of Ag.<sup>68</sup>

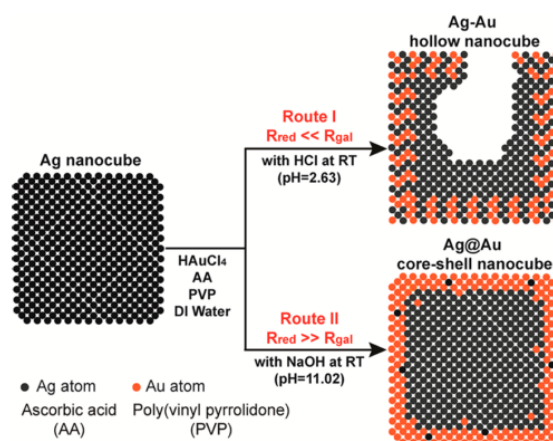


Figure 1.13: Illustration of the two possible routes for Au reduction. Route I is dominated by galvanic exchange whereas Route II is dominated by reduction by AA. Reproduced with permission from Ref[59]. Copyright 2014 American Chemical Society.

### 1.4.3 Titania shell

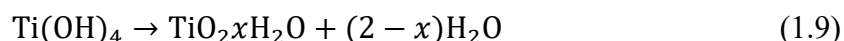
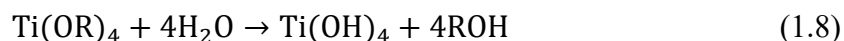
Titania has been widely used in the photocatalytic process and in photoelectrochemistry for use in hydrogen production and the degradation of environmentally harmful organic compounds, and in photovoltaic cells.<sup>69</sup> For our purposes, the prospect of having a novel photocatalyst is attractive since the silver can act as a plasmonic sensitizer.<sup>70</sup>

Furthermore, silver/titania nanoarrays have shown SERS activity when undergoing charge transfer with target molecules, such as 4-mercaptobenzoic acid (4-MBA) – a common SERS probe.<sup>71, 72</sup> This SERS activity is higher than the signal enhancement of 4-MBA on pure TiO<sub>2</sub> nanoparticles.<sup>71</sup> The proposed AgNC/TiO<sub>2</sub> core/half-shell morphology would therefore be a promising candidate for SERS signal enhancement due to the further enhancement through the hot-spots formed following dimerization of the core/half-shell nanoparticles.

The sol-gel process is often used when TiO<sub>2</sub> nanoparticles and shells are synthesized. The sol-gel process can be used for either inorganic precursors or alkoxides. The term sol-gel refers to the formation of a colloidal solution (sol) from monomers wherein the colloids then further interact to form an interconnected network (gel).<sup>73</sup> The general process involves a molecular precursor from which an oxide network is obtained following polymerization reactions.<sup>74</sup> The process begins with hydrolysis of the precursor followed by condensation to form a three-dimensional oxide network. The reactions specific to TiO<sub>2</sub> formation are shown below: the first reaction is hydrolysis, where M-OH

bonds are formed, and the second is condensation, where there is the departure of water:

74, 75



Where R is an alkyl chain. Chelating agents (e.g. diols, carboxylic acids, diketonates) may be added to assist in the control of the hydrolysis.<sup>76</sup> Condensation for TiO<sub>2</sub> formation is usually accomplished by gelization and calcination. Condensation pulls together the constitute particles of the gel into a compact mass although crystalline TiO<sub>2</sub> is not achieved until the calcination step is performed.<sup>76</sup> Calcination is the process by which the compound is heated to high temperatures, usually with the aim of removing organic molecules from the final product. This technique also completes the crystallization of titania, wherein either anatase phase or rutile phase can be formed.<sup>76</sup> Both crystal phases are formed by chains of distorted TiO<sub>6</sub> octahedra (Figure 1.14 A). In a conventional unit cell of the anatase phase, there are four TiO<sub>2</sub> units, meaning 12 atoms total, where each oxygen atom is coordinated to three titanium atoms lying in the same plane through one long apical bond and two short equatorial bonds (Figure 1.14 B). As for the rutile phase, the organization and coordination of the atoms are the same although only two titania units are contained within the unit cell, meaning a total of 6 atoms per unit cell (Figure 1.14 C).<sup>69</sup> It is important to take into consideration the crystal phase of TiO<sub>2</sub> when establishing the end purpose of the material. For example, the crystal phase of TiO<sub>2</sub> greatly impacts its photocatalytic properties; namely, anatase TiO<sub>2</sub> is typically more active than rutile TiO<sub>2</sub>.<sup>77</sup>

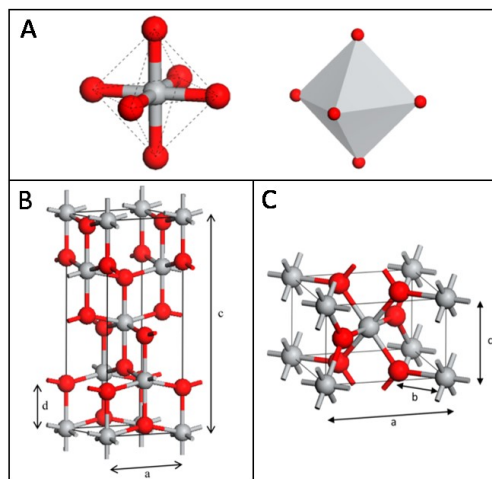


**Figure 1.14:** Schematic representation of (A)  $\text{TiO}_6$  octahedron of anatase and rutile  $\text{TiO}_2$ ; (B) Tetragonal structure of anatase; (C) Tetragonal structure of rutile. Titanium and oxygen atoms are represented by gray and red spheres, respectively. Adapted with permission from Ref[69]. Copyright 2014 American Chemical Society.

A couple of studies by Masahiko et al. found that preparing  $\text{TiO}_2$  from titanium oxysulfate sulfuric acid hydrate or titanium(IV) isopropoxide (TTIP) in the presence of the cationic surfactant cetyltrimethylammonium bromide (CTAB) resulted in mesoporous  $\text{TiO}_2$  with anatase crystallinity.<sup>78, 79</sup> They subsequently followed up this work with  $\text{TiO}_2$  coated Ag using TTIP as the precursor and CTAB as a protective agent for Ag. They concluded that the sol-gel reaction occurred selectively on the CTAB-Ag surface and that the reaction was catalyzed by CTAB.<sup>80</sup> Imhof et al. also showed that PVP-capped silver particles allowed the growth of a titania shell,<sup>81</sup> thus confirming that, while CTAB is not required, some capping agent is. It was also found that there must be careful manipulation of other parameters, such as Ti:Ag mole ratio,<sup>82</sup> in order to have well-defined shell growth. Below 10% Ti:Ag mole ratio, complete  $\text{TiO}_2$  shells around Ag nanospheres were formed. However, at and above 10% Ti:Ag mole ratio, there were Ag particles randomly dispersed in a  $\text{TiO}_2$  matrix.<sup>82</sup>

While titanium(IV) isopropoxide (TTIP) is an effective precursor for coating silver nanoparticles, it was found that its hydrolysis is too rapid for the proper formation of gold/TiO<sub>2</sub> core/shell nanoparticles and will only form TiO<sub>2</sub> colloids.<sup>83</sup> The knowledge that the reaction rates will determine whether heterogeneous or homogeneous growth occurs, dependent on the core material chosen, is important for the understanding of how it may affect the other components in our system.

#### 1.4.4 Silica shell

Silica particles have long been studied due to their ability to enhance the thermal, mechanical, optical, abrasion resistance and surface hardness properties of composite coatings.<sup>73</sup> In their mesoporous form, they have been of interest for their large surface area and superior thermal stability. This makes them attractive for a variety of applications in diverse fields such as drug delivery, biosensors, molecular separations, catalysis, and high-performance liquid chromatography.<sup>73</sup> As mentioned in section 1.1.3, there have been attempts to form metal/silica core/half-shell nanoparticles.<sup>23, 24, 25</sup> Moreover, the research into silica coated silver particles is long-standing.<sup>84, 85, 86, 87, 88, 89</sup> However, there has not yet been the synthesis of AgNC with a silica half-shell coating. The value of this combination lies once again in the SERS enhancement of AgNC as well as in the chemical stability of silica, to be used as a versatile SERS sensor through dimer formation. Often, the method for dimer and multimer formation of silver nanoparticles is through the manipulation of particle and linking molecule concentrations.<sup>90</sup> This however is insufficient since it results in an arbitrary mix of dimers, trimers, and multimers of various orientations. Through our proposed core/half-shell morphology, we aim to control the number of particles that form

the multimer and the monomer's orientation by selectively functionalizing the exposed silver. In addition to the above-mentioned uses, our proposed particles will also be useful for the formation of complex nanostructures.

Silica nanoparticles are typically synthesized via the Stöber method, a sol-gel technique specific to  $\text{SiO}_2$ , that was developed by Werner Stöber, Arthur Fink, and Ernst Bohn in 1968. This method was designed to synthesize monodisperse suspensions of silica microparticles and involved the use of ammonia as a base catalyst, an alcohol solvent, water for hydrolysis, and an alkyl silicate as the precursor.<sup>91</sup> This method has remained largely unchanged due to its simplicity and short reaction times. It has however been adapted to accommodate silica growth onto other particles. For example, in order to promote growth on silver nanoparticles, a coating of poly(vinylpyrrolidone) (PVP) is required. PVP is an amphiphilic polymer that is soluble in water and many non-aqueous solvents. This behavior arises from the presence of a highly polar amide group within the pyrrolidone ring and apolar methylene and methine groups in the ring and along its backbone. This polymer also makes the affinity of the AgNC surface to silica sufficiently high and results in silica shells that have PVP polymer chains dispersed within it (Figure 1.15).<sup>81, 92</sup>

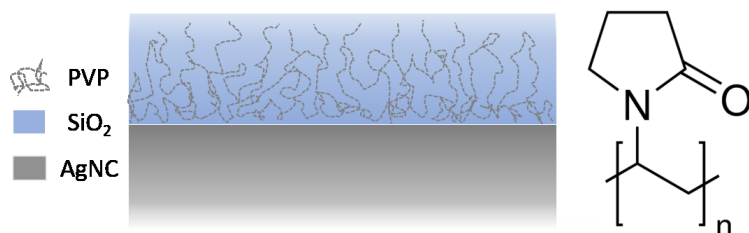


**Figure 1.15:** Schematic illustration of PVP chains integrated into the silica shell that coats an AgNC. The structure of PVP is shown on the right.

The sol-gel method involves four main steps: hydrolysis, condensation, growth, and aggregation.<sup>73</sup> In our case, in the presence of ammonia and alcohol, tetraethyl orthosilicate (TEOS) is used as the precursor and water is needed for hydrolysis. It is base catalysed by ammonia, providing particles with a negative, stabilizing surface charge.<sup>93</sup> The following reactions are a commonly shown, simplified explanation of the hydrolysis (1.10) and condensation (1.11) steps. It begins with an alkyl silicate reacted with water to form orthosilicic acid,  $\text{Si}(\text{OH})_4$ , which then produces  $\text{SiO}_2$  and water.<sup>93</sup> R is substituted for the alkyl chain ( $\text{C}_2\text{H}_5$  for TEOS).

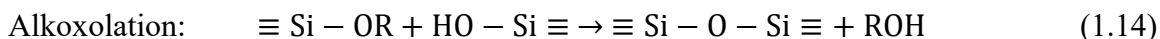
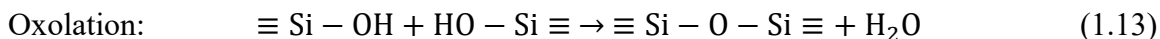


The complete hydrolysis that is required to form  $\text{Si}(\text{OH})_4$  is unlikely to be achieved and, more often, condensation will occur between either two Si-OH groups or an Si-OH group and an alkoxy group to form bridging oxygen and a water or alcohol. Oxolation occurs when there is condensation between two hydroxylated metal species that produces compounds with Si-O-Si bonds and the release of water. Alkoxolation occurs when there is condensation between a hydroxide and an alkoxide that produces compounds with Si-O-Si bonds and the release of alcohol.<sup>73, 94</sup> Below are the more accurate hydrolysis and polycondensation reactions:

**Hydrolysis:**



**Condensation:**



Colloidal particles will form once enough interconnected Si-O-Si bonds are formed in close proximity. These colloids will then link together to form the three-dimensional oxide network.<sup>73</sup>

A side effect of using ammonium as a catalyst is that it can cause the breakdown of the AgNC since the reaction of silver and ammonium will form  $\text{Ag}(\text{NH}_3)_2^+$  which dissolves in the water/alcohol solution.<sup>85, 86</sup>



This reaction can be avoided through the use of a different base catalyst such as dimethylamine.<sup>86</sup> Additionally, the use of base may be avoided all together if the acid-catalyzed route is taken. However, the structure of the oxide network changes dependent on which catalyst is used. For acid-catalyzed reactions, the product is composed of weakly cross-linked, linear polymers and have fewer pores. For base-catalyzed reactions, the rapid hydrolysis results in highly branched clusters. This difference in structure is due to the silicon oxide's increased solubility in alkaline medium; this favours the inter-linking of silica clusters.<sup>73</sup>

#### 1.4.5 Cuprous oxide shell

The growth of cuprous oxide (copper (I) oxide,  $\text{Cu}_2\text{O}$ ) on noble metals, such as gold and silver, has been studied at length due to its potential for use in clean energy conversion, gas sensing, CO oxidation, catalysis, photochemical evolution of  $\text{H}_2$  from water, and photocurrent generation.<sup>95,96</sup> In this work,  $\text{Cu}_2\text{O}$  was chosen in part for its high refractive index, allowing in-solution hybridization.

Since  $\text{Cu}_2\text{O}$  is a p-type semiconductor with a band gap of  $2.17\text{eV}$ ,<sup>95</sup> the combination of silver and cuprous oxide would also be extremely beneficial for photocatalysis wherein the silver acts as a plasmonic sensitizer as seen in the work by Wu et al.<sup>47</sup> As mentioned previously,  $\text{Ag}/\text{Cu}_2\text{O}$  core/shell nanoparticles have been used as enhanced photocatalysts due to the silver core acting as a plasmonic sensitizer. In this type of photocatalyst, the electron-hole pair in the semiconductor is formed from the transfer of photoexcited plasmonic energy from the metal to the semiconductor.<sup>47</sup> This can occur through two pathways: direct electron transfer (DET) or plasmon-induced resonant energy transfer (PIRET). In DET, there is the transfer of hot electrons from the metal to the semiconductor.<sup>97</sup> In PIRET, however, the energy transfer occurs from near-field electromagnetic interaction between the interband transition dipole of the semiconductor and the LSPR dipole of the metal.<sup>97</sup> Both of these mechanisms contribute to the occurrence of the LSPR-induced charge separation in the semiconductor.<sup>47</sup>

#### 1.4.5.1 Growth mechanism

The growth of cuprous oxide on silver metal nanocrystals has been shown to be epitaxial. Truncated silver nanocubes have a face-centered cubic crystal lattice with the  $\{100\}$ ,  $\{110\}$ , and  $\{111\}$  facets exposed at the faces, edges, and corners of the nanocube, respectively.<sup>57</sup> Cuprous

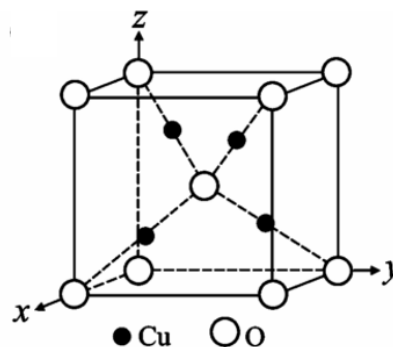


**Figure 1.16:** Crystal structure of  $\text{Cu}_2\text{O}$ . Reproduced with permission from Ref[98]. Copyright 2009 WILEY-VCH.

oxide has a cuprite structure: body-centered cubic packing of oxygen atoms with copper atoms occupying one-half of the tetrahedral sites (Figure 1.16).<sup>95, 98</sup> Silver and cuprous

oxide have the lattice parameters of 4.090Å and 4.269Å, respectively, resulting in a lattice mismatch of 4.4%.<sup>99</sup> It has been proven that Cu<sub>2</sub>O grows epitaxially from the {111} and the {100} facets of the AgNC.<sup>99,100</sup> An X-ray diffraction (XRD) pattern of a Cu<sub>2</sub>O coated silver nanowire and a schematic representation of the silver and cuprous oxide lattice interface is shown in Figure 1.17. Two growth processes have been proposed for this metal-cuprous oxide core-shell nanoparticle. The first, named hollow-shell-refilled (HSR), was first discovered by Kuo et al. in 2009. In this process, the outer shape of the shell is constructed first and is connected to the core via Cu<sub>2</sub>O bridges. The core is then able to guide growth and the shell is filled.<sup>101</sup> The second growth process, observed in this thesis, is more intuitive and is comprised of three steps:<sup>99</sup>

- 1) nucleation of Cu<sub>2</sub>O nanoparticles on the metal core;
- 2) Cu<sub>2</sub>O nanoparticle growth;
- 3) crystal reconstruction to relieve stress.

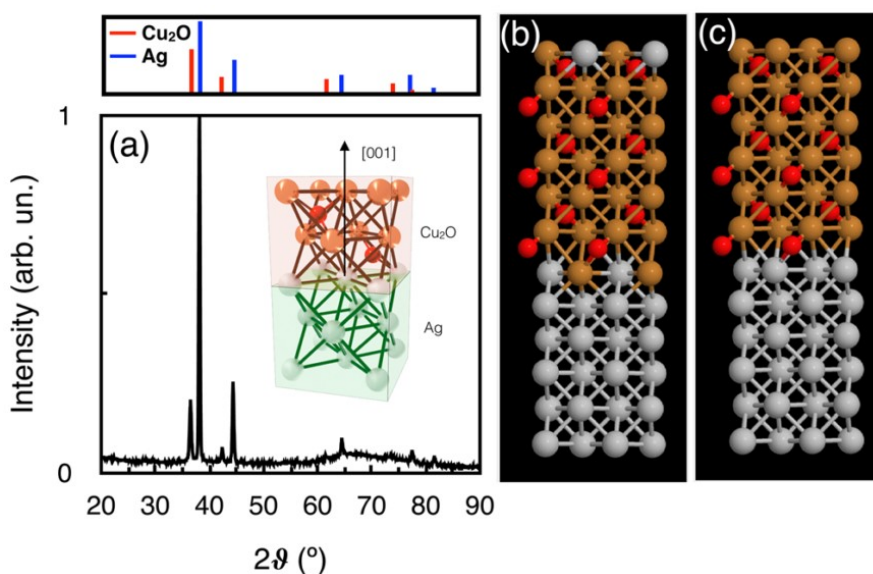
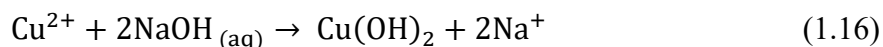
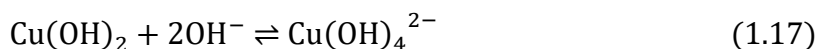


**Figure 1.17:** (A) XRD pattern of a Cu<sub>2</sub>O coated silver nanowire and (B,C) a schematic representation of the silver and cuprous oxide lattice interface. Brown spheres are the Cu atoms, red spheres are O atoms, and gray spheres are Ag atoms. Reproduced with permission from Ref[99]. Copyright 2014 American Chemical Society.

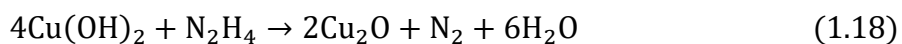
The reactions involved in this synthesis begin with the dissociation of the copper salt in water. The copper ion then goes on to react with the sodium hydroxide to form copper hydroxide:<sup>102</sup>



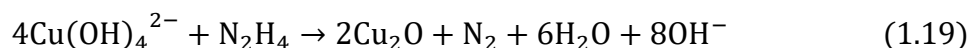
$\text{Cu}(\text{OH})_4^{2-}$  can also be formed in addition to  $\text{Cu}(\text{OH})_2$  since NaOH is added in excess to the copper salt:<sup>103</sup>



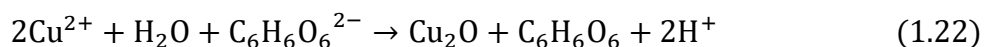
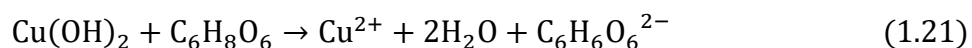
Both  $\text{Cu}(\text{OH})_2$  and  $\text{Cu}(\text{OH})_4^{2-}$  go on to react with hydrazine to form copper (I) oxide:<sup>102,103</sup>



and



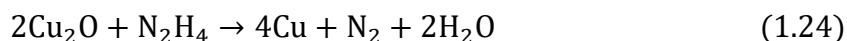
Ascorbic acid was used as an alternative reducing agent in this thesis. It can be understood that the formation process of  $\text{Cu}_2\text{O}$  NPs composes the following three consecutive reactions when ascorbic acid is used as the reducing agent:<sup>104</sup>



It is possible to produce cupric oxide (copper (II) oxide,  $\text{CuO}$ ) as opposed to, or in addition to, cuprous oxide. This occurs with longer reaction times and is seen in the form of black precipitate. It is produced from the dissociation of copper hydroxide:<sup>102</sup>



Copper metal can also be formed if the Cu<sub>2</sub>O is further reduced via the reactions shown below. The reactions involving hydrazine and ascorbic acid as reducing agents are shown in reaction (1.24) and (1.25).<sup>105</sup>



#### 1.4.5.2 Parameters affecting growth

There are many parameters that will affect the morphology of Cu<sub>2</sub>O nanoparticles and shells, such as reducing agent, pH, reagent concentrations, order of addition, shape of the core, and surfactant, amongst others.

By altering the amount of reducing agent added, Huang et al. found that they could synthesize Cu<sub>2</sub>O nanocrystals with cubic, truncated cubic, cuboctahedral, truncated octahedral, octahedral, and short hexapod morphologies.<sup>106</sup> They were also able to produce extended hexapods by decreasing the amount of NaOH and adjusting the solution to a pH of 7. Figure 1.18 presents SEM images of the varied morphologies obtained. Since the reducing agent used was hydroxylamine hydrochloride (NH<sub>2</sub>OH·HCl), the pH of the system decreased as they increased the volume of reducing agent. It is presumed that the amount of reducing agent influenced the growth rate along the [100] direction relative to the growth in the [111] direction.<sup>106</sup> Additionally, they were able to alter the morphology of the Cu<sub>2</sub>O nanocrystals by changing the order of addition of their reagents. Originally, to water they added, in order: CuCl<sub>2</sub>, sodium dodecyl sulfate (SDS), NH<sub>2</sub>OH·HCl, NaOH.<sup>107</sup> Upon modifying the order of addition to CuCl<sub>2</sub>, NaOH, SDS, and NH<sub>2</sub>OH·HCl they formed particles with sharper edges and had a wider variety of obtainable morphologies.<sup>106</sup> By

adding the NaOH second,  $\text{Cu}(\text{OH})_2$  and  $\text{Cu}(\text{OH})_4^{2-}$  were formed before the introduction of the reductant. This is important since the crystal growth rate is fast and the final particle shape is dependent on the initial crystal morphology.<sup>95</sup>

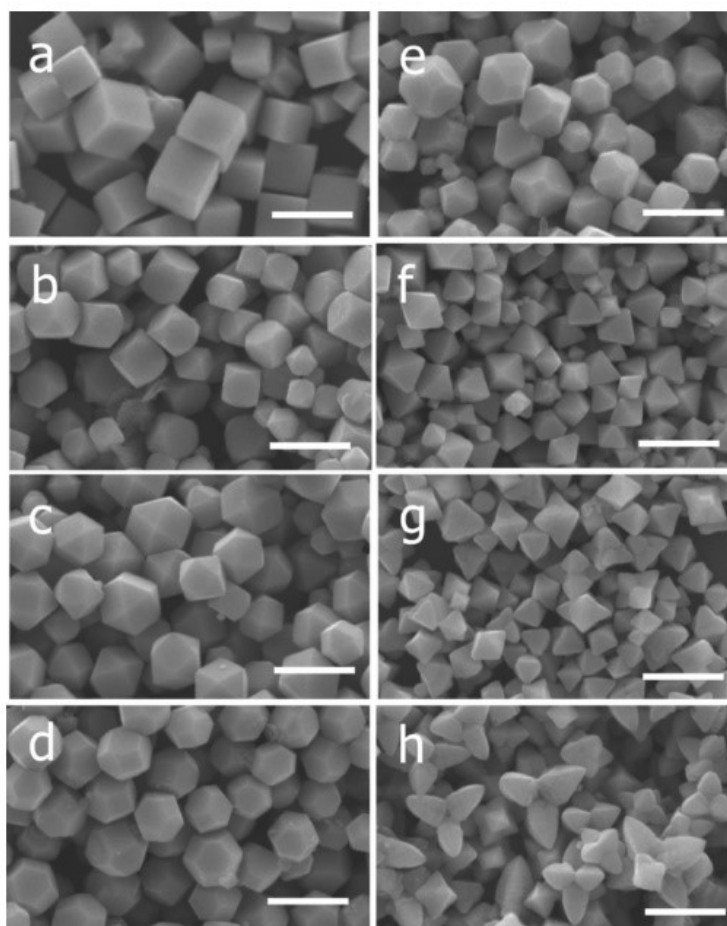


**Figure 1.18:** SEM images of  $\text{Cu}_2\text{O}$  nanoparticles synthesized with (a-g) increasing amounts of reducing agent and (h) reduced amount of NaOH. Scale bar =  $1\ \mu\text{m}$ . (a) cubes, (b) truncated cubes, (c) cuboctahedra, (d) type I truncated octahedra, (e) type II truncated octahedra, (f) octahedra, (g) short hexapods, and (h) extended hexapods. Reproduced with permission from Ref[106]. Copyright 2009 American Chemical Society.

As mentioned above, cuprous oxide grows epitaxially from the silver metal core. This therefore means that the shape and crystal structure of the core will heavily impact the resultant morphology of the shell. With quasi-spherical silver cores,  $\text{Cu}_2\text{O}$  shells that have rough outer surfaces have been produced. Silver quasi-spherical nanoparticles contain multitwined crystalline structures with boundaries between crystalline domains and are

enclosed by  $\{111\}$  and  $\{100\}$  facets aligned along different directions. Therefore, the  $\text{Cu}_2\text{O}$  shell formed will have nanoscale protrusions formed from the crystalline boundaries, resulting in surface roughness.<sup>100</sup> When using truncated silver nanocubes as the core, a truncated octahedral  $\text{Cu}_2\text{O}$  shell is grown due to the presence of the  $\text{Ag}\{111\}$  facets at the corners and the  $\text{Ag}\{100\}$  facets at the faces. A truncated octahedral shell is obtained because the  $\text{Cu}_2\text{O}\{100\}$  facet has a higher surface energy and so growth along the  $[100]$  direction is faster. This leads to a shell that is dominated by the  $\{111\}$  facet.<sup>100</sup> Additionally, when using a AgNC core with sharp corners, cubic shells are obtained due to the limited presence of the  $\text{Ag}\{111\}$  facet, allowing the  $\{100\}$  of the  $\text{Cu}_2\text{O}$  to dominate.<sup>100</sup> In this thesis, a similar geometry to the octahedrons are obtained, albeit only half octahedrons are formed, and will be called pyramidal half-shells. Cubic half-shells are also formed and will be named as such.

Surfactant is often employed in nanoparticle syntheses to direct the shape of the particle. The morphological control occurs because of anisotropy in the adsorption stability of the surfactant, meaning it will adsorb onto a crystallographic plane more strongly than others. When the surfactant adsorbs onto a plane it lowers the surface energy of this plane and interferes with the growth in the orthogonal plane. Therefore the area of the lower energy surfaces will increase and that of the higher energy surfaces will decrease.<sup>108</sup> Two examples of surfactants used in  $\text{Cu}_2\text{O}$  nanoparticle syntheses are sodium dodecyl sulfate (SDS) and poly(vinyl)pyrrolidone (PVP). The organization of the Cu and O surface atoms in the  $\text{Cu}_2\text{O}$  crystal will vary dependent on the crystallographic plane. The  $\{111\}$  surface is nonpolar whereas the  $\{100\}$  surface is polar.<sup>108</sup> Both the SDS and PVP will preferentially

bind to the {111} facets of the Cu<sub>2</sub>O, inhibiting growth on the {111} planes and allowing exclusive deposition on the {100} facets. This will lead to octahedral nanoparticles predominantly capped with {111} facets.<sup>95,108</sup>

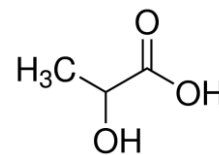
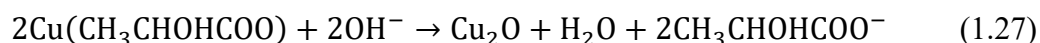


**Figure 1.19:** Structure of lactic acid.

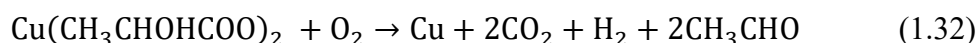
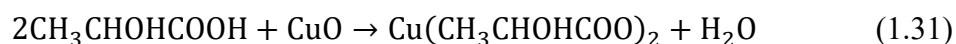
In E. Jorgenson's Masters thesis (Ianoul group, 2017), it was suspected that lactic acid (LA) (Figure 1.19) acted as a shape directing agent in a similar fashion to SDS and PVP. However, upon further experimentation it is hypothesized that it is affecting the growth kinetics of the reaction as opposed to simply binding to a certain crystallographic plane. Lactic acid has not often been used in the synthesis of Cu<sub>2</sub>O. However, in the cases where it has been employed, an electrochemical processes took place and followed the reactions detailed below:<sup>109</sup>



Additionally, while not for the production of cuprous oxide, lactate from lactic acid has been used in the production of cupric oxide (CuO) as such:<sup>110</sup>



LA has also been used as a stabilizer during the synthesis of copper metal in which copper lactate is formed from lactic acid and cupric oxide and is then reduced to Cu after annealing:<sup>111</sup>



A suspected effect of LA on the growth of Cu<sub>2</sub>O half-shells is through the pH change of the system. The pH of the Cu<sub>2</sub>O growth solution has been shown to affect the rate of reduction. S. Sun et al. showed that with increased pH, the reduction rate decreased, and thus affected the morphology in the sense that growth was incomplete.<sup>112</sup> Therefore, since LA is a weak acid its addition to the growth solution may sufficiently reduce the pH to increase the rate of reaction and ultimately affect the rate of growth of the crystallographic planes.

## **2 Experimental**

### **2.1 Substrate preparation**

#### **2.1.1 Silver nanocube synthesis**

The sulfide-mediated polyol method from Xia et al.<sup>53</sup> was used to synthesize silver nanocubes (AgNC) of approximately 60-70 nm in edge length. The AgNCs were made by initially combining 0.4082 g of poly(vinyl)pyrrolidone (PVP, Sigma-Aldrich, MW ~55 000) and 15 mL ethylene glycol (EG, Sigma-Aldrich, 99.8%) and heating the solution to 150 °C in an oil bath while stirring at 300 rpm for 1 hour. With maintained heating and stirring, 25 μL of a 0.5 M NaCl (Bioshop, >99%) solution in EG, 175 μL of a 3 mM Na<sub>2</sub>S (Sigma-Aldrich) solution in EG, and 1.5 mL of a 0.3 M AgNO<sub>3</sub> (Alfa Aesar, >99%) solution in EG were added to the above mixture. The Na<sub>2</sub>S and AgNO<sub>3</sub> solutions were prepared within an hour of use. The silver nitrate was added at a rate of approximately 1 mL/min. The reaction was monitored periodically with a Shimadzu UV-2450 UV-vis spectrophotometer. Once a peak at 350 nm was observed, another 1.5 mL of the AgNO<sub>3</sub> solution was added at approximately 1 mL/min. The reaction was quenched in an ice bath

once the desired spectrum was obtained (peaks present at around 350 nm and 470 nm). Fifteen millilitres of ethanol (Commercial Alcohols, 95%) was added to the cooled solution. The solution was then centrifuged at 12 000 rpm for 30 minutes, the supernatant was removed and the precipitate was redispersed in ethanol and centrifuged three times at 12 000 rpm for 10 minutes, removing the supernatant and redispersing the precipitate in ethanol each time.

### **2.1.2 Polystyrene spin coating**

A 3 wt% polystyrene (PS) solution was made by stirring 0.2523 g of polystyrene (Sigma-Aldrich, 192 000 g/mol) in 9.41 mL of toluene (Anachemia, ACS reagent grade) for 3 hours at room temperature. The solution was then passed through a 0.22  $\mu\text{m}$  filter. Next, glass slides were cleaned by sonicating them in methanol (VWR Analytical, ACS grade) for 3-5 minutes, rinsing them with methanol followed by deionized water (Milli-Q, 18.2 M $\Omega$ ), and then placing them in the oven at 100 °C until dry.

For spin coating, a homemade spin coater was used. The slide was taped to the spin coater and enough of the 3 wt% PS solution to just cover the entire slide surface was pipetted. The slide was spun at approximately 4000 rpm for 1 minute, removed and left to dry for 1 hour at room temperature. The slides were then placed in the oven overnight at 110 °C to anneal. The PS thin films were characterized using atomic force microscopy; surface roughness and film thickness were measured.

### **2.1.3 Langmuir-Schaeffer deposition**

Silver nanocube monolayers were made through the Langmuir-Schaeffer deposition technique. The Langmuir-Blodgett trough (NIMA) was first cleaned with a few

millilitres of chloroform (Alfa Aesar, >99%) and surfactant-free Kimwipes. Following this, a series of water-cleaning steps were performed. By filling the trough with deionized water (Milli-Q, 18.2 M $\Omega$ cm) and then removing the water with an aspirator two to three times, impurities were removed from the trough. A new Wilhelmy plate was added, the trough was filled with deionized water, and was left for 20 minutes before removing the water and refilling it a final time. A pressure-area isotherm at a barrier speed of 30 cm<sup>2</sup>/min was performed to confirm the cleanliness of the trough. If the pressure remained equal to or below 0.1 mN/m, the trough was deemed clean enough for the following steps. If not, the water-cleaning sequence was repeated.

The silver nanocubes were then prepared for deposition onto the surface of the water in the trough. A 0.735 mL aliquot of silver nanocubes (maximum extinction of undiluted sample was 314 a.u.) in ethanol were centrifuged at 12 000 rpm for 10 minutes. The ethanol supernatant was removed and the cubes were redispersed in chloroform and centrifuged at 12 000 rpm for 5 minutes. The supernatant was removed and the cubes redispersed in chloroform and centrifuged once more. The supernatant was then removed and the cubes were redispersed in chloroform. The cubes were transferred to a chloroform-rinsed glass vial and the chloroform was evaporated under a stream of N<sub>2</sub> gas. Once dry, 10  $\mu$ L of freshly prepared 1 mg/mL dioleoylphosphatidylcholine (Avanti Polar Lipids, Inc.) in ethanol and 200  $\mu$ L of chloroform were added to the vial. The vial was capped and quickly sonicated to remove the plated cubes from the glass walls.

The cubes were delicately deposited onto the surface of the water in the trough drop-wise with a syringe from a few millimeters above the water's surface. To allow the

chloroform to evaporate and the cubes to stabilize, it was left for 20-40 minutes. A forward and reverse isotherm was performed to compress the cubes to a liquid phase and then expand them to a gas phase. The pressure was kept at 0.5 mN/m for deposition. The polystyrene coated glass slides prepared earlier were horizontally tapped onto the surface of the AgNC-covered water and dried with N<sub>2</sub> gas. The monolayers were characterized with UV-vis spectrometry and atomic force microscopy.

#### **2.1.4 Silver nanocube embedding**

Silver nanocubes supported by polystyrene on glass slides were heated on a hot plate to just above the glass transition temperature of polystyrene, approximately 110-115°C. UV-vis extinction spectra were taken to monitor the extent of embedment. Atomic force microscopy was used to measure the height of nanocube exposed.

### **2.2 Half-shell growth**

Unless otherwise specified all shell growth methods were performed on AgNCs that were partially embedded into a polystyrene thin film supported on a glass slide.

#### **2.2.1 Gold**

Two methods were used in the gold shell growth trials.

The first method utilized a magnetic plastic puck upon which the 1cm x 1cm sample slide was immobilized. This puck was then spun at 200rpm for the duration of the experiment. To a beaker containing the puck and sample, varied amounts of deionized water, poly(vinyl)pyrrolidone, L-ascorbic acid (Bioshop, 99%), NaOH (Bioshop, 99%), and HAuCl<sub>4</sub> (Aldrich, >99%) were added. The HAuCl<sub>4</sub> solution was injected at a rate of

either 0.02mL/min or 0.04mL/min. The reaction times varied from 5-30 minutes. The parameters of each trial are detailed in section 3.2 Table 1.

The second method utilized a glass round bottom flask and glass stir rod as the support for the 1cm x 1cm sample slide. The slide was immobilized on the stir rod and spun vigorously for the duration of the experiment. All trials used 120mL deionized water as the solvent. Varied amounts of H<sub>Au</sub>Cl<sub>4</sub>, sodium citrate (Sigma-Aldrich, 99%), and hydroquinone (Sigma-Aldrich, 99%) were used, and the reaction times varied from 10 minutes to 1 hour. The parameters of each trial are detailed in section 3.2 Table 2.

### **2.2.2 Titania**

In a general reaction, a 1cm x 1cm slide sample was submerged into 20mL of a titanium(IV) isopropoxide (Aldrich, 97%) solution in anhydrous ethanol (Commercial Alcohols, 100%) for a set amount of time either with or without stirring at 300 rpm. The slide was then rinsed with anhydrous ethanol and dried under N<sub>2</sub>. The concentrations tested were 1, 2, 3, 4, and 5 mM. The reaction times tested were 1 hour, 5 hours, 19 hours and 25 minutes, and 24 hours. The parameters of each trial are detailed in section 3.3 Table 3.

### **2.2.3 Silica**

For the growth of the silica half-shell onto the silver nanocube core, a sol-gel technique is used. For slides that had dimensions of approximately 1cm x 1cm, the following procedure was used. The sample was immersed in a Nalgene bottle containing 20 mL isopropanol (Anachemia, ACS grade), 4 mL deionized water, 0.4 mL ammonia (Anachemia, 28%, reagent grade), and 160  $\mu$ L tetraethoxysilane (Aldrich, 99%). This solution was made immediately before each trial. The reaction was left for 30 minutes and

the slide was then rinsed with isopropanol and dried with  $N_2$ . The parameters of each trial are detailed in section 3.4 Table 4.

#### 2.2.4 Copper oxide

For this synthesis, the reaction took place under constant flow of  $N_2$  to limit the premature oxidation of the reducing agents used. Initially, 250mL of deionized water was purged with  $N_2$  for 15 minutes. The sample slide was then submerged and stirred vigorously. From here, the parameters varied dependent on the trial performed and are listed in Table 5 found in section 3.5 of this thesis. To summarize, varying amounts of aqueous solutions of sodium hydroxide, DL-lactic acid (Bioshop, 85-90%), copper precursor –  $Cu(NO_3)_2$  (Sigma-Aldrich, 99%) or  $CuSO_4$  (Sigma-Aldrich, 99%) – and reductant – hydrazine (Fluka, 25%) or ascorbic acid – were added to the purged  $dH_2O$ . Some experiments omitted lactic acid. In other trials, the reagents underwent “fast addition” in which each was added as a single, quick injection. Additionally, some reagent underwent “slow addition” wherein stepwise and continuous addition were tested for the copper precursor and hydrazine. In the case of stepwise addition, 1mL of the copper precursor solution was manually injected at 5-minute intervals, for a total of 10mL. In the case of continuous injection, 10mL of either the copper precursor or the hydrazine was injected via syringe pump, typically at a rate of 0.2mL/min. The concentration of the “slow addition” reagents were adjusted to match the amount that would have been added in a single fast injection. The order of addition varied between NaOH, LA,  $N_2H_4$ , and Cu precursor or NaOH, LA, Cu precursor, and  $N_2H_4$ . All trials had a reaction time of 50 or 55 minutes. The continuous injection method received the extra 5 minutes. Once the reaction

was complete, the sample slide was rinsed with dH<sub>2</sub>O, then ethanol and dried under a stream of N<sub>2</sub>.

### **2.3 Removal of nanocubes from glass-supported polystyrene**

The coated nanocubes were removed from the glass by sonicating the glass slide in a minimal amount of toluene to dissolve the polystyrene and disperse the AgNC/half-shells in solution.

## **2.4 Characterization**

### **2.4.1 UV-vis spectroscopy**

The extinction spectra of the samples on slide and in solution were measured with a Shimadzu UV-2450 UV-vis spectrophotometer.

### **2.4.2 Atomic Force Microscopy**

Topographical information of the AgNC on the substrate was acquired with a Ntegra (NTMDT, Russia) AFM in semi-contact mode in air at room temperature with 512x512 or 1024x1024 points per image. The measurement scan rate was typically from 0.6-0.71 Hz. The cantilever was made of silicon with a reflective gold coating, it had a tip height of 14-16  $\mu\text{m}$  and a tip curvature radius of 10 nm. The AFM images were processed by Nova image processing software.

### **2.4.3 Transmission Electron Microscopy**

The samples were dropcasted on 300 mesh Cu or Ni carbon support TEM-grids from Electron Microscopy Sciences. The transmission electron microscope used was a FEI Tecnai G2 TEM.

### 3 Results & Discussion

#### 3.1 Sample preparation

In the following section, representative results will provide an overview of the well-established procedures of the sample preparation. It will include the silver nanocube (AgNC) synthesis, the spin coating of the polystyrene (PS) thin films, the deposition of the AgNCs on the PS film through Langmuir-Schaeffer, and the embedment of the AgNCs into the PS.

The AgNCs were first synthesized using the sulfur-mediated polyol method. The extinction measurements (Figure 3.1) show an initial dipolar mode which red shifts as the particles increase in size. At a reaction time of approximately 1 hour, a shoulder appears at  $\sim 350$  nm, indicative of a more cubic shape. Over the following 20 minutes, this 350 nm shoulder becomes defined, the dipole continues to red shift, and there is the appearance of a shoulder at  $\sim 400$  nm from the quadrupolar mode. The reaction was quenched once the dipolar peak had reached approximately 470 nm since this corresponds to cubes with an edge length of 60-70 nm. The size and shape of the silver nanocubes were confirmed with transmission electron microscopy (TEM) (Figure 3.2).

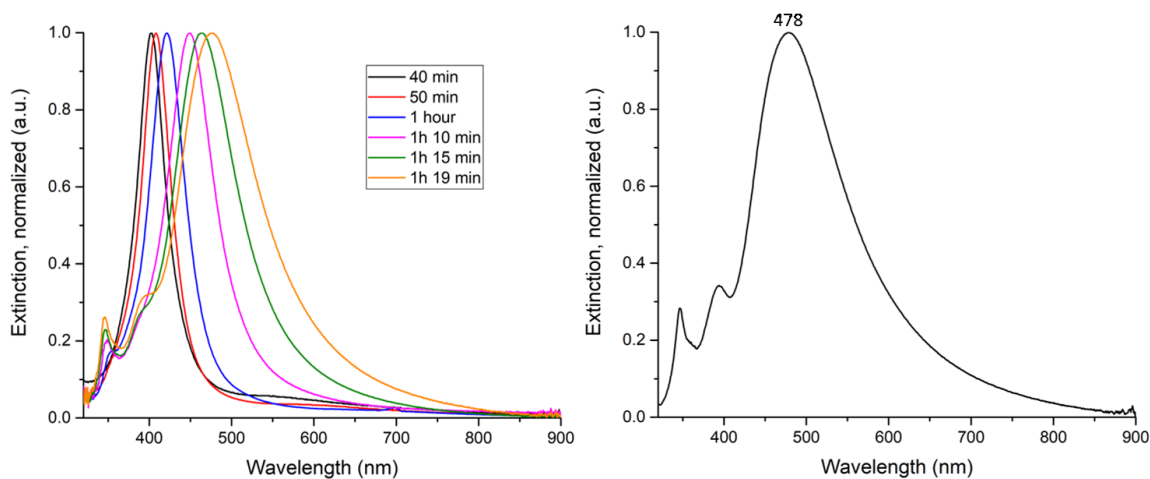


**Figure 3.1:** Extinction spectra of (left) growth of AgNC and (right) quenched AgNC suspended in ethanol.

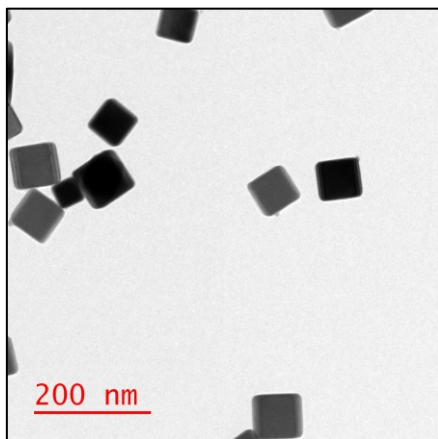


**Figure 3.2:** TEM image of silver nanocubes.

Alongside the AgNC synthesis, the glass-supported polystyrene thin films were produced. The spin coated PS resulted in films that had a roughness of  $\sim 0.5$  nm and a thickness of approximately 120 nm. This was deemed sufficient for use since the film thickness was greater than the edge length of the cubes and the surface was

smooth, without large features that would impede embedment and growth. Atomic force microscopy (AFM) images of a representative sample are provided in Figure 3.3. Unaltered films were used for roughness measurements and scratched films were used to measure the thickness.

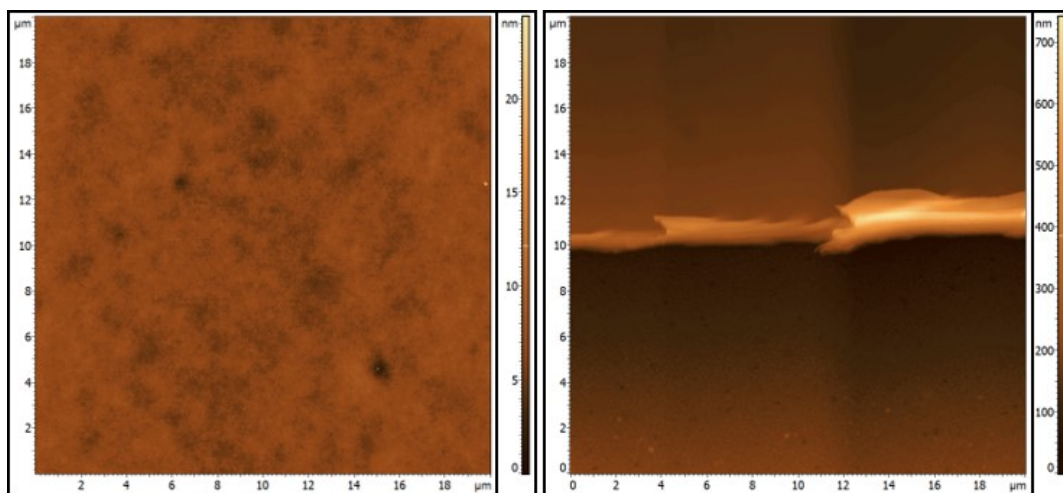


**Figure 3.3:** AFM images of (left) a PS thin film and (right) a scratched PS thin film for thickness measurements.

Once the AgNCs and the PS thin films were prepared, Langmuir-Schaeffer deposition was used to transfer a monolayer of nanocubes onto the glass-supported polystyrene substrate. This deposition method allows control of the interparticle distance and, for the present work, it was tailored such that there was enough room for shell growth. The nanoparticle organization on the substrate was observed through AFM (Figure 3.4), where it was confirmed that a well spaced monolayer of AgNCs was achieved. The extinction spectrum of the cubes on the substrate was measured and showed a multipolar mode at 339 nm, a quadrupolar mode at 397 nm and a dipolar mode at 442 nm (Figure 3.4).

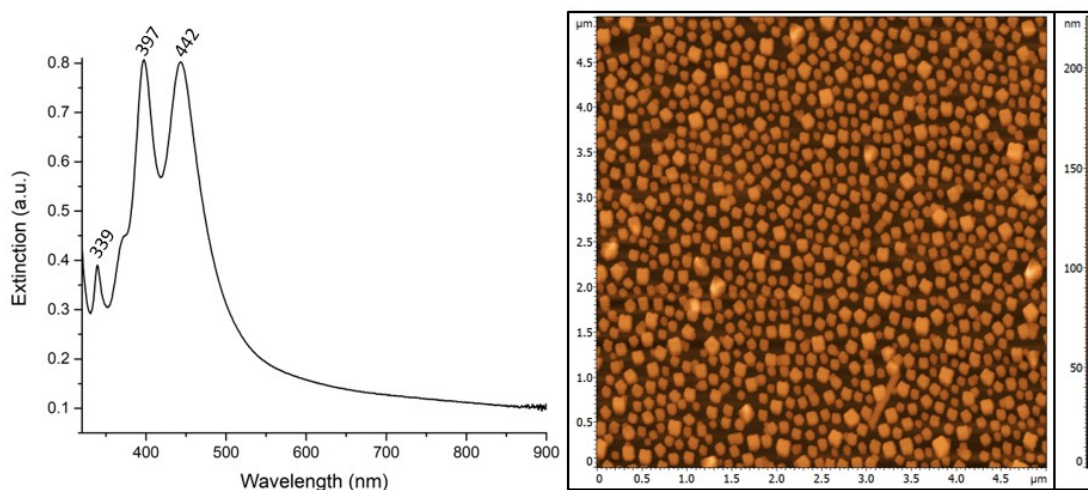


**Figure 3.4:** Left: Extinction spectrum of AgNC on PS thin film. Right: AFM image of the AgNC monolayer on PS.

Following the successful deposition of silver nanocubes on the PS thin film. The embedment process was completed wherein the sample slide was heated to just above 110°C until the desired embedment depth was achieved. The progression of embedment was monitored via UV-vis spectrometry (Figure 3.5) and the wavelengths of the LSPR peaks was used as an indicator of depth. In this case, before embedment, the LSPR peaks had wavelengths of 339 nm, 397 nm, and 447 nm. After heating for 6 minutes, the LSPR peaks had red shifted to 354 nm, 404 nm, and 477 nm. The embedment depth was confirmed with atomic force microscopy. For the majority of the experiments detailed in the following sections, the AgNCs were embedded half-way ( $\sim 35$  nm) into the PS.

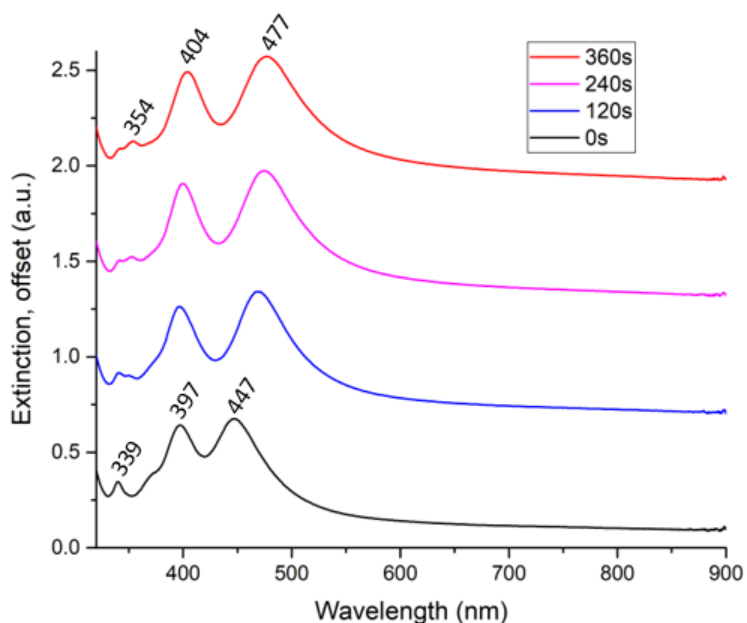


**Figure 3.5:** Extinction spectra of progression of AgNC embedment into PS. Heating time shown in legend.

In summary, the sample preparation was successfully completed through AgNC synthesis, spin coating of PS thin films, Langmuir-Schaeffer deposition, and AgNC embedment into PS. The following sections will detail the growth of various shell materials using the samples as prepared above.

### 3.2 Gold shell

The trials for the gold shell formation are divided into two separate methods with the first utilizing an alkaline solution and ascorbic acid as the reductant and the second using hydroquinone as the reducing agent. The reaction parameters for each trial are listed in Table 1 and Table 2.

**Table 1:** Reaction parameters for Method 1 trials

| Sample ID | Reaction time | dH <sub>2</sub> O | PVP         | AA              | NaOH            | HAuCl <sub>4</sub> | Gold injection rate |
|-----------|---------------|-------------------|-------------|-----------------|-----------------|--------------------|---------------------|
| Gm1-1     | 15min         |                   | 2mL,<br>1mM | 5mL,<br>10mM    | 0.5mL,<br>200mM | 0.8mL,<br>0.1mM    | 0.02mL/min          |
| Gm1-2     | 30min         | 16.2mL            | 2mL,<br>1mM | 0.5mL,<br>100mM | 0.5mL,<br>200mM | 0.8mL,<br>0.1mM    |                     |
| Gm1-3     | 10min         | 7.2mL             | 8mL,<br>1mM | 2mL,<br>100mM   | 2mL,<br>200mM   | 0.8mL,<br>0.4mM    |                     |
| Gm1-4     | 10min         | 4.2mL             | 2mL,<br>1mM | 5mL,<br>100mM   | 9mL,<br>200mM   | 0.8mL,<br>0.4mM    |                     |
| Gm1-5     | 5min          | 3.4mL             | 2mL,<br>1mM | 5mL,<br>100mM   | 8mL,<br>200mM   | 1.6mL,<br>0.4mM    | 0.04mL/min          |

**Table 2:** Reaction parameters for Method 2 trials

| Sample ID | Reaction time | dH <sub>2</sub> O | HAuCl <sub>4</sub> | Sodium citrate    | Hydroquinone | Other details  |
|-----------|---------------|-------------------|--------------------|-------------------|--------------|----------------|
| Gm2-1     | 1h            | 120mL             | 600μL,<br>14.6mM   | 25μL, 34mM        | 100μL, 30mM  | Embedded AgNC  |
| Gm2-2     | 1h            |                   | 60μL,<br>14.6mM    | 250μL,<br>0.34mM  | 100μL, 3mM   |                |
| Gm2-3     | 5min          |                   | 60μL,<br>14.6mM    | 250μL,<br>0.34mM  | 100μL, 3mM   |                |
| Gm2-4     | 20min         |                   | 60μL,<br>14.6mM    | 250μL,<br>0.34mM  | 100μL, 3mM   | Supported AgNC |
| Gm2-5     | 10min         |                   | 60μL,<br>14.6mM    | 250μL,<br>0.34mM  | 100μL, 3mM   |                |
| Gm2-6     | 10min         |                   | 60μL,<br>1.46mM    | 250μL,<br>0.034mM | 100μL, 0.3mM | Embedded AgNC  |

#### 3.2.1 Method 1

This method was modified by the work of Qin et al.<sup>59</sup> wherein they formed AgNC/Au core/shell nanoparticles where the shell had thicknesses of 3 and 6 atomic layers. The aim of utilizing this method, other than forming Au shells, was to increase the shell

thickness from their work in order to reliably obtain complete coverage of the exposed AgNC. In this work, water was used as the solvent, PVP was used as a capping agent, ascorbic acid as a reducing agent, sodium hydroxide to increase the pH, and HAuCl<sub>4</sub> as the precursor. These trials were performed using a magnetic plastic puck upon which the sample slide was immobilized and stirred. The set-up is pictured in Figure 3.6.



**Figure 3.6:** Apparatus used for method 1.

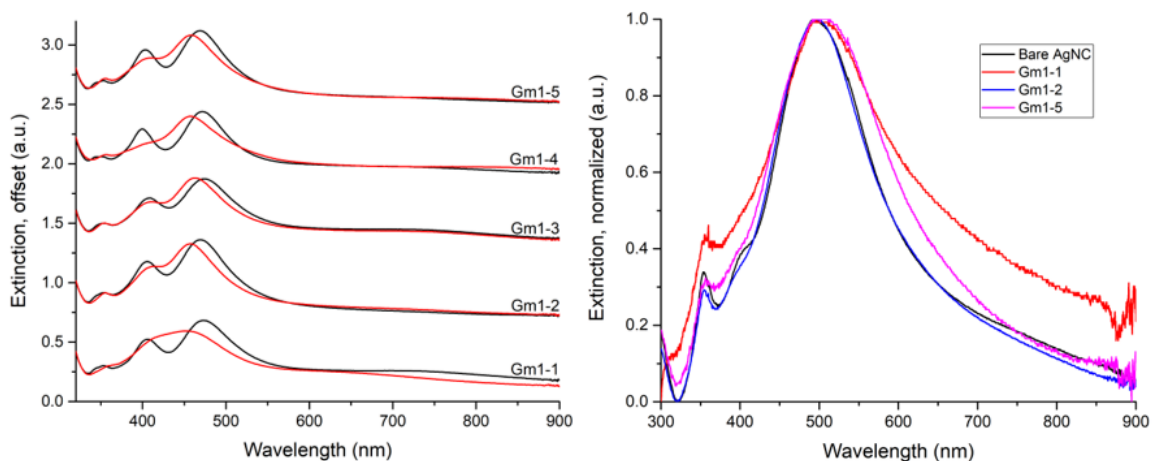


**Figure 3.7:** Extinction spectra of (left) embedded AgNC before (black) and after (red) reaction and (right) particles removed from substrate and suspended in toluene. Parameters for each sample is described in Table 1.

The first trial of this series, Gm1-1, was duplicated from the work by Qin et al.<sup>59</sup> with the single alteration of having AgNC embedded in PS as opposed to suspended in solution. The parameters were: 2mL of 1mM PVP, 5mL of 10mM AA, 0.5mL of 200mM NaOH, and 0.8mL 0.1mM HAuCl<sub>4</sub> (added at 0.02mL/min), and a 15-minute reaction time.

The extinction spectrum of the embedded particles (Figure 3.7) after reaction showed a merging of the quadrupolar (Q) and dipolar (D) modes (Q mode red shifting, D mode blue shifting). The extent of the merging was such that the peaks were no longer resolved from each other yet not quite completely combined into a single peak. This hinted to some surface alteration. However, the extinction of the particles suspended in solution had a very slight red shift in comparison to bare AgNC, potentially an indication that the gold shell was thin enough to not alter the LSPR of the AgNC (Figure 3.7). From transmission electron microscopy (TEM) images, it was observed that small gold nanospheres (5-10 nm in diameter) were formed (Figure 3.8A). The surface of the AgNC also exhibited increased roughness. The energy-dispersive X-ray spectroscopy (EDS) measurements showed a small amount of Au present in the sample with the small nanospheres containing a larger amount of Au in comparison to when the electron beam was focused elsewhere.

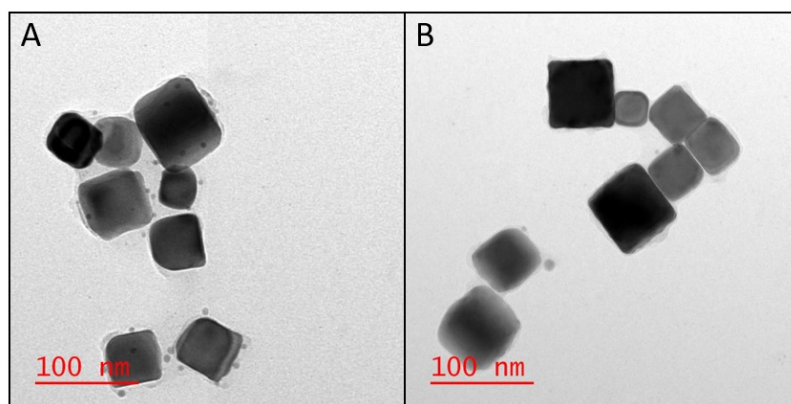


**Figure 3.8:** TEM images of reacted AgNC from sample (A) Gm1-1; (B) Gm1-2

In trial Gm1-1, the total volume of the reaction solution was slightly too low. The puck used for spinning the sample is approximately 1-1.5 cm in height and the total volume was 8.3mL. This did not leave enough space around the sample to allow full sample-solution interaction and to prevent an obstructing vortex. Therefore, the subsequent trial,

Gm1-2, had 16.2mL of dH<sub>2</sub>O added. This trial and all subsequent trials, the volume of water was adjusted to have a total solution volume of 20mL. This trial also had double the reaction time to permit increased growth. This did not prove fruitful since the extinction spectrum of the embedded AgNCs did not show as extensive Q and D peak merging as sample Gm1-1 (Figure 3.7). Also, the multipolar mode at 350nm was more pronounced than that of the previous trial. The extinction spectrum of the particles suspended in toluene showed no change from the bare AgNC (Figure 3.7). Once again, the TEM images showed Au nanospheres of 5-10 nm in diameter in addition to AgNC with increased roughness (Figure 3.8B). This surface roughness is a good indication that some galvanic exchange is taking place.

To entice further growth for sample Gm1-3, the amount of reagents was increased by a factor of 4 and the reaction time decreased to 10 minutes. The in-solution extinction spectra remained the same as for sample Gm1-2. Furthermore, their AFM images did not highlight any differences in that the topography was the same before and after reaction and the AgNC height did not deviate from the initial 34.7 nm.

Since the referenced paper emphasized a required pH of 11, test trials were performed to determine the required amount of NaOH to maintain this pH. Also tested was the amount of H<sub>2</sub>AuCl<sub>4</sub> needed to lower the pH below pH of 11. This is of importance since the galvanic exchange pathway would dominate over the ascorbic acid reduction pathway below this pH. It was found that 8-9 mL of 200mM NaOH was required and as much as 3 mL of 0.4mM H<sub>2</sub>AuCl<sub>4</sub> could be added without significant change to the pH. As such, the following parameters were used: 2mL of 1mM PVP, 5mL of 100mM AA, 8mL of 200mM

NaOH (with an additional 1mL added later on), and 0.8mL of 0.4mM HAuCl<sub>4</sub> (added at 0.02mL/min), and 10-minute reaction time. The extinction spectrum of this trial, Gm1-4, showed a depleted M and Q mode and a slightly blue shifted D mode (Figure 3.7). This change could be an indication that there was a loss of cubicity.

In the final trial, Gm1-5, 2mL of 1mM PVP, 5mL 100mM AA, 8mL 200mM NaOH and 1.6mL 0.4mM HAuCl<sub>4</sub> (added at 0.04mL/min), and a 5-minute reaction time were employed. The doubling of gold precursor volume and injection rate was done in order to have an overabundant excess of gold with which to push the reaction forward. This did not have an effect on the extinction spectrum. Although, the solution went from clear and colourless to having black/purple precipitate which points to homogeneous nucleation and growth of Au particles in solution, meaning the amount added was too high.

Control tests were performed on a PS thin film supported on glass without the presence of AgNCs. Identical parameters to Gm1-3 were employed. There was no change in the extinction spectra before and after reaction however the atomic force microscopy images determined that there was some growth on PS (Figure 3.9). The result change in film thickness was within error – from  $201 \pm 4$  nm (18 measurements) to  $192 \pm 21$  nm (13 measurements) – whereas the change in roughness was appreciable with an increase from  $0.55 \pm 0.05$  nm (5 measurements) to  $1.72 \pm 0.15$  nm (4 measurements). This roughness is evidenced from the image in which we see growths 20-40 nm in height. Therefore, there was some loss of gold to the substrate, interfering with the growth of gold uniquely on the silver nanoparticles.

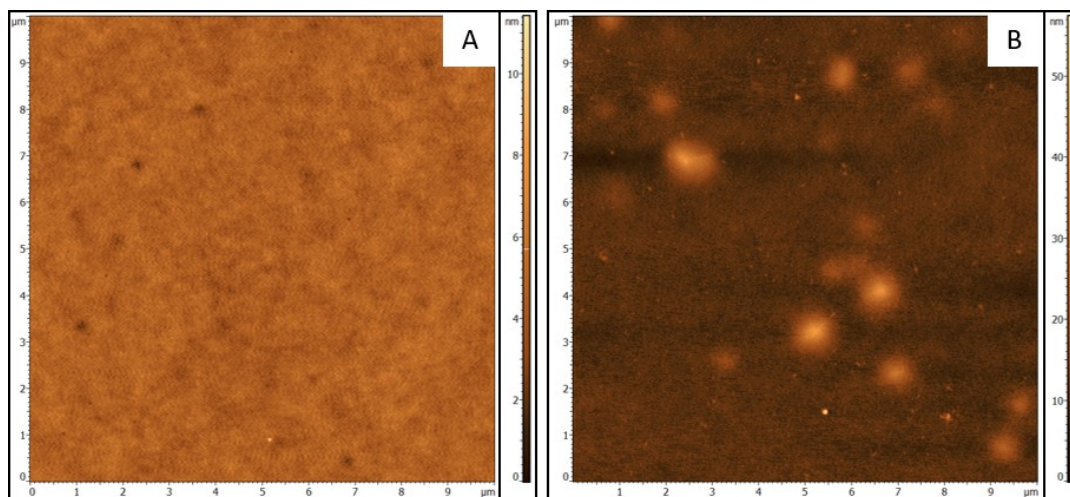


**Figure 3.9:** AFM of (A) before and (B) after of reaction on a PS control. Experiment conditions were identical to those of sample Gm1-3.

It has been previously shown that, for the formation of Au nanorods in a seeded method, ascorbic acid must be used in a molar excess of 10% compared to the gold concentration and that while less than this amount leads to very little growth, more than 10% promotes the growth of spherical particles. This is due to increased reduction rate and homogeneous nucleation in solution.<sup>113</sup> This fine balance of ascorbic acid and gold is a good indication of what failed in this growth since the amount of ascorbic acid was much higher than that of  $\text{HAuCl}_4$ . This resulted in predominantly random nucleation in solution as indicated by the Au nanospheres observed in the TEM images. If this were to be attempted again, there would need to be greater attention paid to this molar ratio.

In summary, multiple trials were attempted for the formation of gold shells on silver nanocubes using the method as described by Qin et al.<sup>59</sup> In this work, water was used as the solvent, PVP was used as a capping agent, ascorbic acid as a reducing agent, sodium hydroxide to increase the pH, and  $\text{HAuCl}_4$  as the precursor. While Qin et al. reported success with this dual reduction route, its reproduction was not confirmed under the

conditions tested in the present work. It is however possible that an extremely thin layer of gold was deposited due to the observed change in extinction.

### 3.2.2 Method 2

This following method was modified from the work by Haber et al.<sup>114</sup> wherein they grew gold/silver/gold core/shell/shell nanoparticles. The reason for selecting this method was that it would provide thicker shells than the previous method. Hydroquinone is supposed to more effectively reduce  $\text{Au}^+$ . While this may be a benefit it may also be detrimental since the lower reducing strength of ascorbic acid is supposed to regulate the propensity for galvanic exchange. In this work, water was used as a solvent, sodium citrate was used as a capping agent,

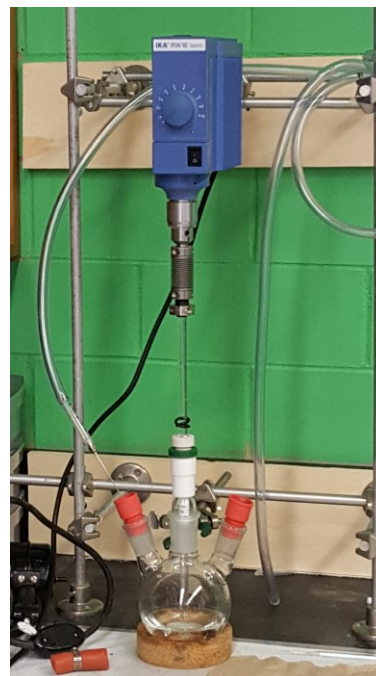


**Figure 3.10:** Apparatus used for method 2. Syringe pump not pictured.

hydroquinone was used as a reducing agent, and  $\text{HAuCl}_4$  as the precursor. The stirring apparatus was comprised of a round bottom flask and a glass stir rod upon which the sample slide was attached, and this rod was connected to a mechanical stirrer (Figure 3.10).

The first trial of this series, Gm2-1, was duplicated from the work by Haber et al.<sup>114</sup> with the single alteration of having AgNC embedded in PS as opposed to spherical Au/Ag core/shell nanoparticles suspended in solution. The parameters were: 600 $\mu\text{L}$  of 14.6mM  $\text{HAuCl}_4$ , 25 $\mu\text{L}$  of 34mM sodium citrate, 100 $\mu\text{L}$  of 30mM hydroquinone, 120mL  $\text{dH}_2\text{O}$ ,

and reaction time of 1 hour. The resultant extinction spectrum of this trial exhibited a complete loss of the AgNC LSPR (Figure 3.11).

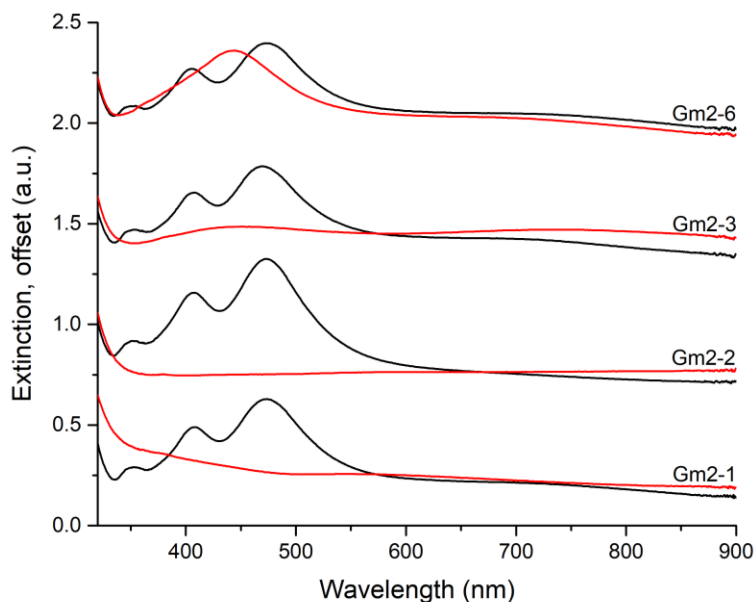


**Figure 3.11:** Extinction spectra of embedded AgNC before (black) and after (red) reaction. Parameters for each sample is described in Table 2.

The following two trials, Gm2-2 and Gm2-3 were conceived in order to limit the extent of LSPR loss. This was done by reducing all reagents by a factor of 10 for sample Gm2-2. Next, sample Gm2-3 also had this 10x reagent decrease with the addition of a lower reaction time from the original 1 hour to 5 minutes. This time was chosen since the slide exhibited a colour change from orange-brown to purple within those 5 minutes which is indicative of surface alteration. The extinction spectra showed a loss of LSPR for the embedded particles (Figure 3.11) whereas the spectra of those suspended in toluene still had a dipolar mode present (Figure 3.12). The dipole mode of sample Gm2-2 was very weak and red-shifted. The dipole mode of Gm2-3 was also red-shifted. TEM images were acquired of both samples and they showed predominant formation of Au nanocages with

Gm2-3 having some remaining AgNCs (Figure 3.14). This means that galvanic exchange took place instead of gold deposition on silver.

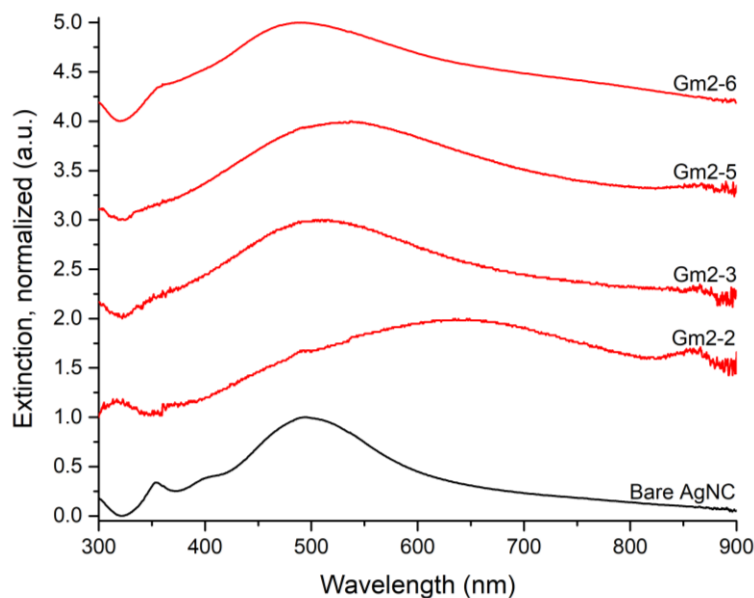


**Figure 3.12:** Extinction spectra of particles removed from substrate and suspended in toluene.

The following trials, Gm2-4 and Gm2-5, were performed on AgNCs which were supported on the PS film, i.e. not embedded. This was done in order to observe if PS was interfering with the deposition by leaching over the top of the AgNC during the embedment process. The results, however, were no different from the above trials with the extinction spectra of the embedded particles having a loss of LSPR (Figure 3.13) and those of the suspended particles had a red shifted dipole peak (Figure 3.12). The TEM images of sample Gm2-5 also showed Au nanocages (Figure 3.14).

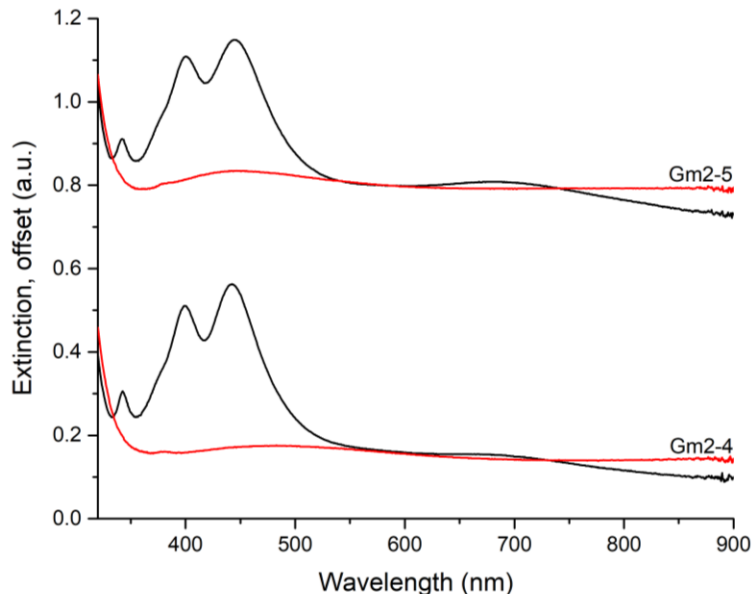


**Figure 3.13:** Extinction spectra of supported AgNC before (black) and after (red) reaction. Parameters for each sample is described in Table 2.

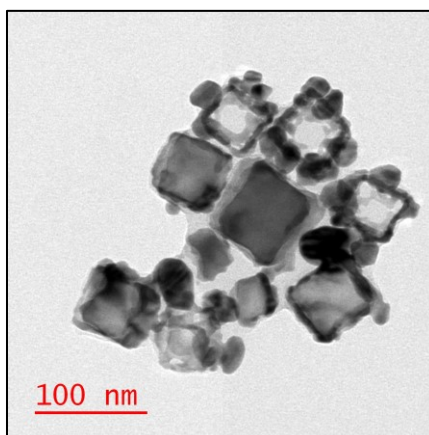


**Figure 3.14:** Representative TEM image of Au nanocages formed after reaction using method 2. Some AgNCs still present.

The final trial, Gm2-6, was organized in order to, once again, limit the extent of LSPR loss. This was done by reducing all reagents by a factor of 10. Early results are promising with the extinction spectrum of the embedded particles showing Q and D mode peak merging with the in-solution spectrum having no shift in peaks. However, there was loss in definition of peaks. These changes lie between the Gm1 trials, which saw very minimal change, and the other Gm2 trials which had over-reacted. Unfortunately, the

characterization was incomplete and the presence of a conformal half-shell of gold cannot be drawn.

A polystyrene control was performed under the same conditions as Gm2-2. Measured through AFM, the surface roughness increased from  $0.55 \pm 0.05$  nm (5 measurements) to  $0.74 \pm 0.06$  nm (4 measurements). The growths observed were of 10-20 nm in height and were not as plentiful as Gm1.

The predominant conclusion was that the reactions that took place were galvanic exchange and not gold reduction onto silver. This is due to the absence of a decrease in the reaction rate of the galvanic exchange which would be required for the reduction by hydroquinone in order to dominate and promote growth onto the AgNCs.

### 3.2.3 Gold shell conclusions

In this work, two gold growth methods were attempted. For the first method, water was used as the solvent, PVP was used as a capping agent, ascorbic acid as a reducing agent, sodium hydroxide to increase the pH, and  $\text{HAuCl}_4$  as the precursor. The presence of ascorbic acid and an alkaline solution should have provided adequate conditions for a decreased galvanic exchange rate and an increased reduction rate of  $\text{Au}^{3+}$  to  $\text{Au}^0$  onto the silver. While the galvanic exchange was successfully suppressed, the deposition of gold onto silver was unconfirmed. For the second method, water was used as a solvent, sodium citrate was used as a capping agent, hydroquinone was used as a reducing agent, and  $\text{HAuCl}_4$  as the precursor. It was found that galvanic exchange took place and so there was no core/half-shell particle formation. There is still potential for this method to provide gold deposition but it would require increased suppression of galvanic exchange and further optimization

of reagent concentrations. Additionally, the growth of Au on the PS mask signifies that another method of Au half-shell growth is required, one in which the growth is selective to the core.

### 3.3 Titania shell

In the following titania shell growth experiments, a few iterations of growth using varied concentrations of the titania precursor, titanium(IV) isopropoxide (TTIP), were attempted. The reaction parameters for each trial are detailed in Table 3.

**Table 3:** Reaction parameters for titania experiments.

| Sample ID | TTIP concentration (mM) | Reaction time (hour) | Stirring speed (rpm) |
|-----------|-------------------------|----------------------|----------------------|
| T1        | 5                       | 5                    | 0                    |
| T2        | 0                       | 24                   | 300                  |
| T3        | 1                       | 24                   | 300                  |
| T4        | 2                       | 24                   | 300                  |
| T5        | 3                       | 24                   | 300                  |
| T6        | 4                       | 24                   | 300                  |
| T7        | 5                       | 24                   | 300                  |
| T8        | 5                       | 24                   | 300                  |
| T9        | 5                       | 24                   | 300                  |
| T10       | 5                       | 24                   | 300                  |
| T11       | 3                       | 24                   | 0                    |

The first two trials to be discussed are those in which the reaction solution was not stirred, samples T1 and T11. In sample T1, the slide was immersed in a 5mM solution of TTIP for 5 hours. This yielded a depletion and blue shift of the Q and D modes as observed in the extinction spectra of the embedded particles in Figure 3.15. Sample T11 demonstrated the same spectral change even though the sample slide was immersed in a 3mM TTIP solution for 24 hours. This blue shift is commonly seen when the sample is

kept in alcohol for an extended period of time and thus this change in extinction is unlikely due to growth of  $\text{TiO}_2$ .

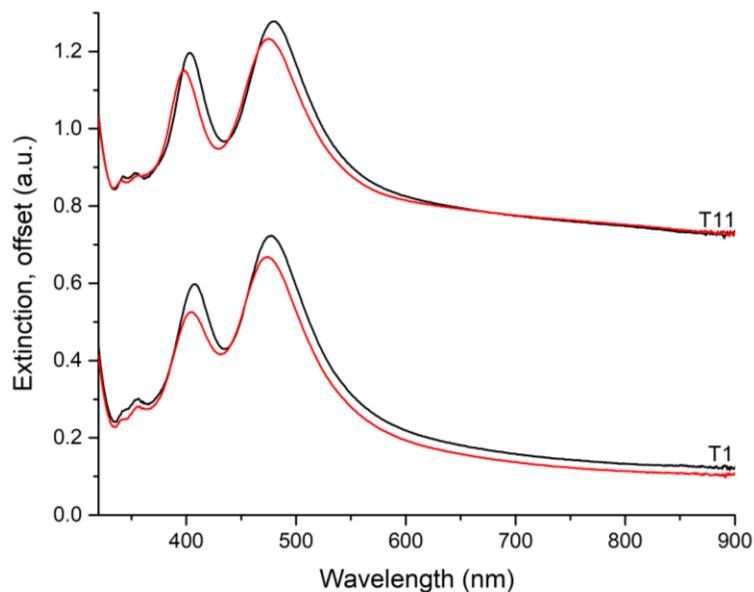


**Figure 3.15:** Extinction spectra of embedded AgNC before (black) and after (red) reaction without stirring. Parameters for each sample is described in Table 3.

The following series of experiments were performed with increasing concentrations of TTIP to determine an adequate growth solution. The solution was stirred at 300 rpm for the duration of the 24-hour reaction time in order to constantly replenish the surface of the AgNC with hydrolyzed TTIP to promote growth of thicker shells. The samples, from T2-T6, were respectively submerged in 0, 1, 2, 3, and 4 mM TTIP solutions. The 0 mM TTIP was simply anhydrous ethanol and served as a negative control. All trials from 0-3 mM TTIP showed the same blue shift of the Q and D modes in the extinction spectra of the embedded particles (Figure 3.16). The 4 mM trial, however, did exhibit a red shift of the Q mode and a blue shift of the D mode due to a more isotropic environment around the AgNCs.

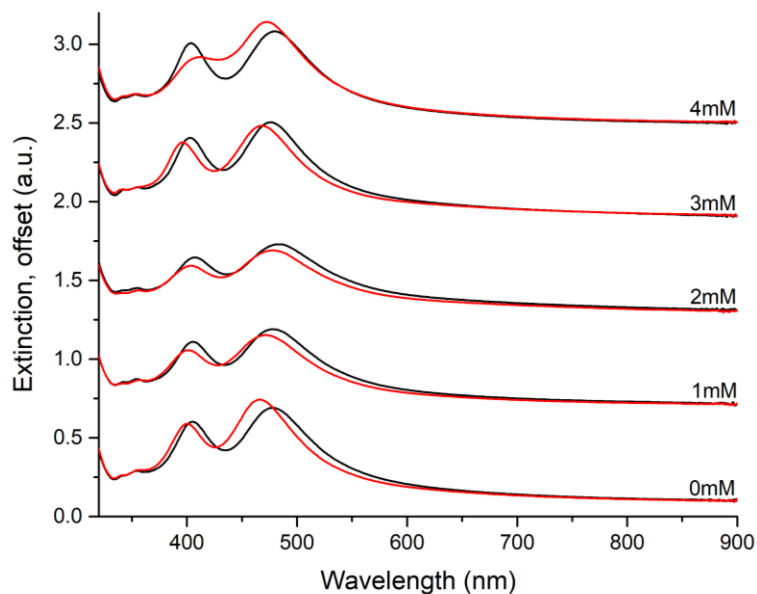


**Figure 3.16:** Extinction spectra of embedded AgNC before (black) and after (red) reaction with increasing amounts of TTIP.

The AFM images taken show increases in height of 1.7 nm, 3.4 nm, 8.0 nm, and 10.7 nm for the trials using 1mM, 2mM, 3mM, and 4mM TTIP, respectively. The topography of the 1mM to 3mM TTIP trials do not show any change (Figure 3.17) yet there is significant change for the trial using 4mM TTIP. This  $\text{TiO}_2$  growth is seen to encompass many AgNCs with most AgNCs being connected to their neighbours via the  $\text{TiO}_2$ .

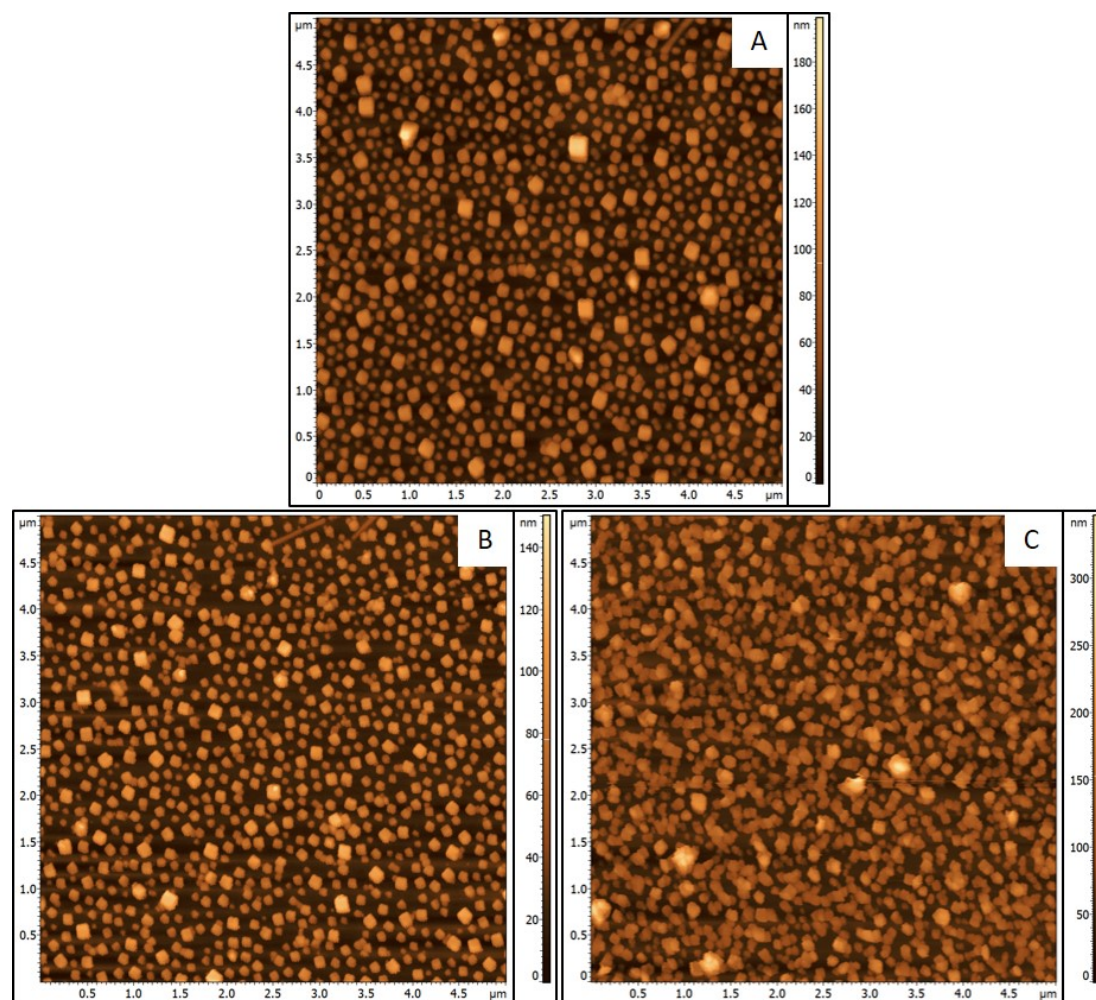


**Figure 3.17:** AFM images of embedded particles (A) before reaction; (B) after reaction with 3mM TTIP; (C) after reaction with 4mM TTIP. The 3mM TTIP trial is representative of the 1mM-3mM trials.

Sample T6 (4mM TTIP) was removed from the substrate and suspended in toluene. The resultant extinction spectrum has a very small red shift of the dipolar mode compared to bare AgNC but is otherwise unchanged (Figure 3.18) and the TEM images show that the  $\text{TiO}_2$  that grew was amorphous and did not form shells on individual AgNCs (Figure 3.19).

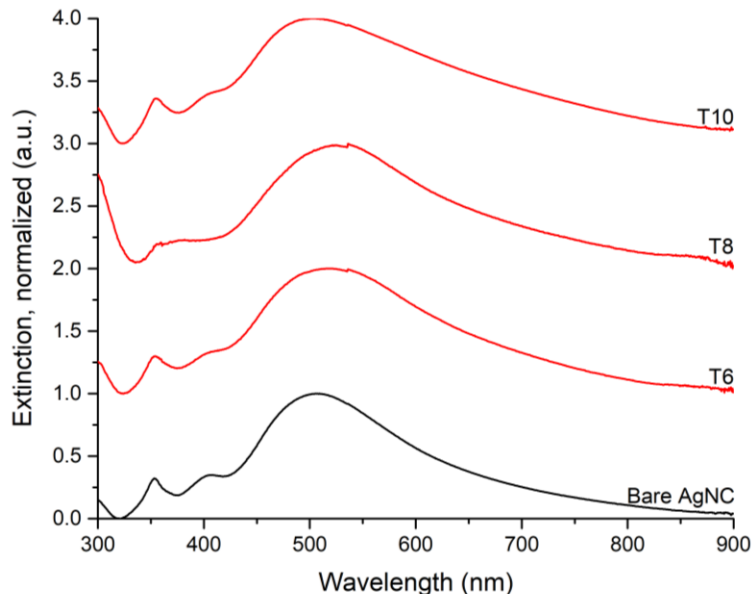


**Figure 3.18:** Extinction spectra of AgNC suspended in toluene before (black) and after (red). Parameters for each sample is described in Table 3.

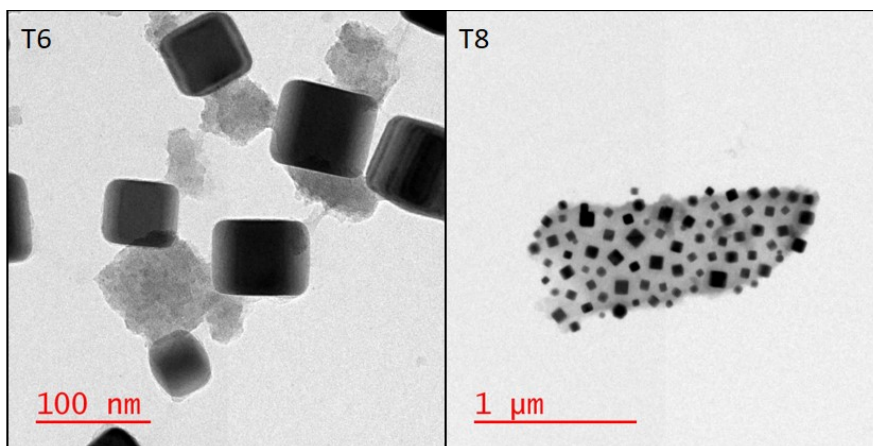


**Figure 3.19:** TEM images of samples T6 and T8.

The trials T7-T10 were performed with 5mM TTIP. This series highlighted the lack of reproducibility of this method. The embedded particles' extinction spectra in Figure 3.20 show significant difference under the same parameters. T7 had a depletion and red shift of the Q mode. T8 had loss of the Q mode and significant red shift of the D mode. T9 saw no change in extinction and T10 had a red shift of the Q mode with a more significant depletion than T8. The in-solution spectra of T8 and T10 show that neither deviate

significantly from the extinction of bare AgNC, although the multipolar mode of T8 has been depleted (Figure 3.18). The TEM of sample T8 show continuous films of TiO<sub>2</sub> containing the AgNC (Figure 3.19). While not the aim of this work, the potential for a “micro-substrate” is interesting.

In this synthesis, anhydrous ethanol was used as the solvent and no water was added to drive the hydrolysis step forward. When 95% ethanol was used as the solvent, immediate uncontrolled hydrolysis of the TTIP occurred. Since no water was manually added to the system, it can be confidently assumed that the moisture from the air in the headspace of the sealed reaction flask was sufficient to cause a gradual hydrolysis of TTIP. However, this is highly detrimental to the reproducibility of the reaction as it was performed in open air. Thus, any further experimentation of solution-based TiO<sub>2</sub> growth with TTIP should take place in a vacuum box.

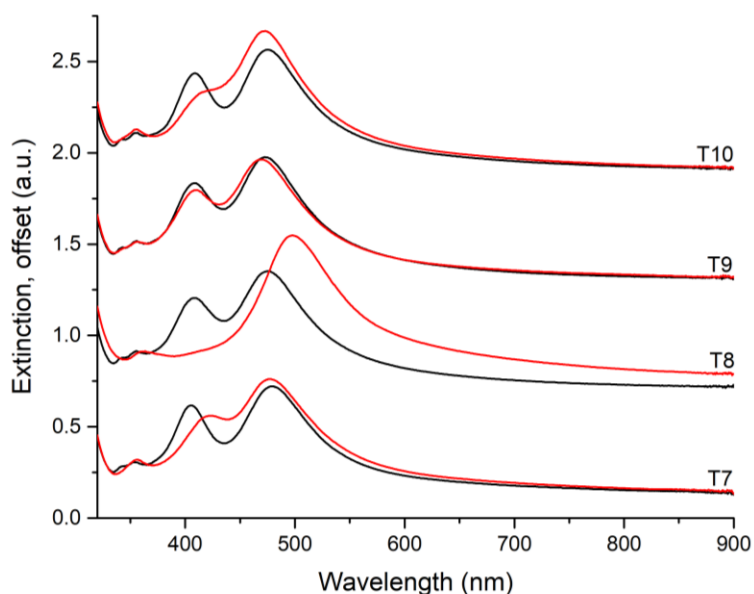


**Figure 3.20:** Extinction spectra of embedded AgNC before (black) and after (red) reaction with 5mM TTIP.

In conclusion, amorphous  $\text{TiO}_2$  was grown on silver nanocubes with a lack of reproducibility. While the lesser grown titania formed a broken network between particles, the greater growth produced  $\text{TiO}_2$  films with a few microns in dimension. Overall, the optical effects of the alteration were minimal. Crystalline  $\text{TiO}_2$  would have been desired due to its photocatalytic properties and high refractive index. Its refractive index would have significantly changed the AgNC's optical properties and allowed in-solution plasmon hybridization. However, due to the temperature limitations of the AgNC, the  $\text{TiO}_2$  could not undergo calcination and thus the crystalline form could not be obtained. Recently however, amorphous  $\text{TiO}_2$  has found uses as a protective coating and as a photocatalyst due to defects that provide increased photocatalytic activity.<sup>115</sup>

### **3.4 Silica shell**

Many iterations of attempted silica half-shell growth were undertaken. The first trials employed ethanol as the solvent with spinning of the sample slide. The following trials used isopropanol as the solvent without stirring or sample spinning. The number of tetraethyl orthosilicate (TEOS) additions was also tested to determine its effect on the shell thickness. Additionally, the reaction was scaled up and a preliminary dimerization experiment was performed. Finally, due to undergrowth of the shell that lead to complete AgNC coverage, a method for the reduction of undergrowth was investigated. The parameters for the above experiments are presented in Table 4.

**Table 4:** Reaction parameters for silica shell growth

| Sample ID | Reaction time | EtOH (mL) | IPA (mL) | dH <sub>2</sub> O (mL) | NH <sub>3</sub> (mL) | TEOS (μL)     | Other details              |
|-----------|---------------|-----------|----------|------------------------|----------------------|---------------|----------------------------|
| S-C1      | 30min         |           | 20       | 0                      | 0                    | 0             | Control                    |
| S-C2      | 30min         |           | 20       | 4                      | 0                    | 0             |                            |
| S-C3      | 30min         |           | 20       | 4                      | 0.4                  | 0             |                            |
| S1        | 4h            | 7.4       |          | 1.8                    | 0.0134               | 200 (1% TEOS) | Sample spun                |
| S2        | 45min         | 7.4       |          | 1.8                    | 0.0134               | 200 (1% TEOS) | Sample spun                |
| S3        | 2h            | 3.7       |          | 0.9                    | 0.067                | 100 (1% TEOS) |                            |
| S4        | 2h            | 7.4       |          | 1.8                    | 0.134                | 200 (1% TEOS) | Sample spun                |
| S5        | 30min         | 3.7       |          | 0.9                    | 0.067                | 200 (1% TEOS) | 2 TEOS additions           |
| S6        | 30min         |           | 20       | 4                      | 0.4                  | 160           | 1 TEOS addition            |
| S7        | 30min         |           | 20       | 4                      | 0.4                  | 160           | 2 TEOS additions           |
| S8        | 30min         |           | 20       | 4                      | 0.4                  | 240           | 3 TEOS additions           |
| S9        | 30min         |           | 20       | 4                      | 0.4                  | 320           | 4 TEOS additions           |
| S10-S11   | 30min         |           | 40       | 8                      | 0.8                  | 320           | 2x scaled up               |
| S12-S23   | 30min         |           | 80       | 16                     | 1.6                  | 640           | 4x scaled up               |
| S24       | 24h           |           | 20       | 4                      | 0                    | 160           | Less NH <sub>3</sub> /time |
| S25       | 15min         |           | 20       | 4                      | 0.4                  | 160           |                            |
| S26       | 30min         |           | 20       | 4                      | 0.2                  | 160           |                            |
| S27       | 2h            |           | 20       | 4                      | 0                    | 160           |                            |
|           |               |           |          |                        | <b>HCl (mL)</b>      |               |                            |
| S28       | 30min         | 20        | 4        | 0.4                    | 160                  | Acid catalyst |                            |
| S29       | 2h            | 20        | 4        | 0.4                    | 160                  |               |                            |

Trials S1-S5 were performed with 95% ethanol as the solvent, with S1, S2, and S4 having the sample slide spun and S3 and S5 not. The samples that had spinning showed a complete loss of LSPR in the extinction spectra of embedded particles (Figure 3.21). This loss of LSPR is due to loss of AgNC from the sample as seen in the AFM images (Figure 3.22). The AFM images of sample S1 are representative of all three samples. Square-shaped pits can be observed in place of the nanocubes. This cube removal is due in part to the interaction of ammonia with the silver leading to the dissolution of the nanocubes. The sample spinning also contributed to this loss by increasing the exposure of the silver to ammonia by replenishing the environment with ammonia continuously.

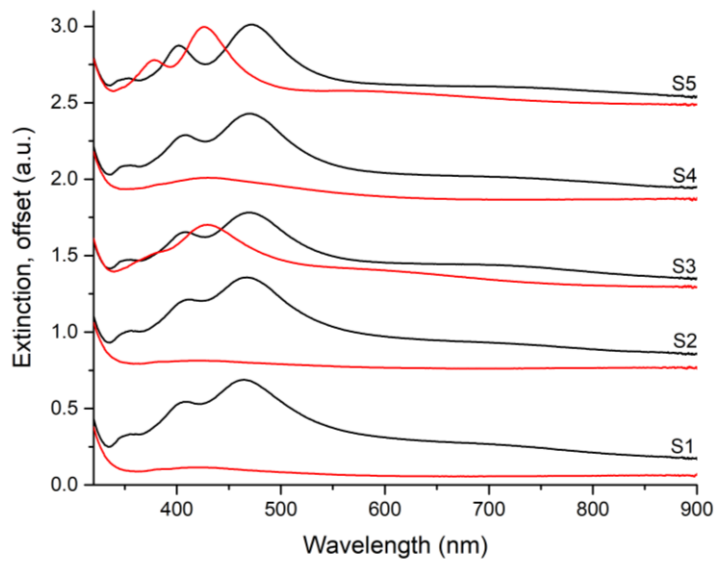


**Figure 3.21:** Extinction spectra of embedded particles before (black) and after (red) the silica growth reaction. Parameters for each sample is described in Table 4.

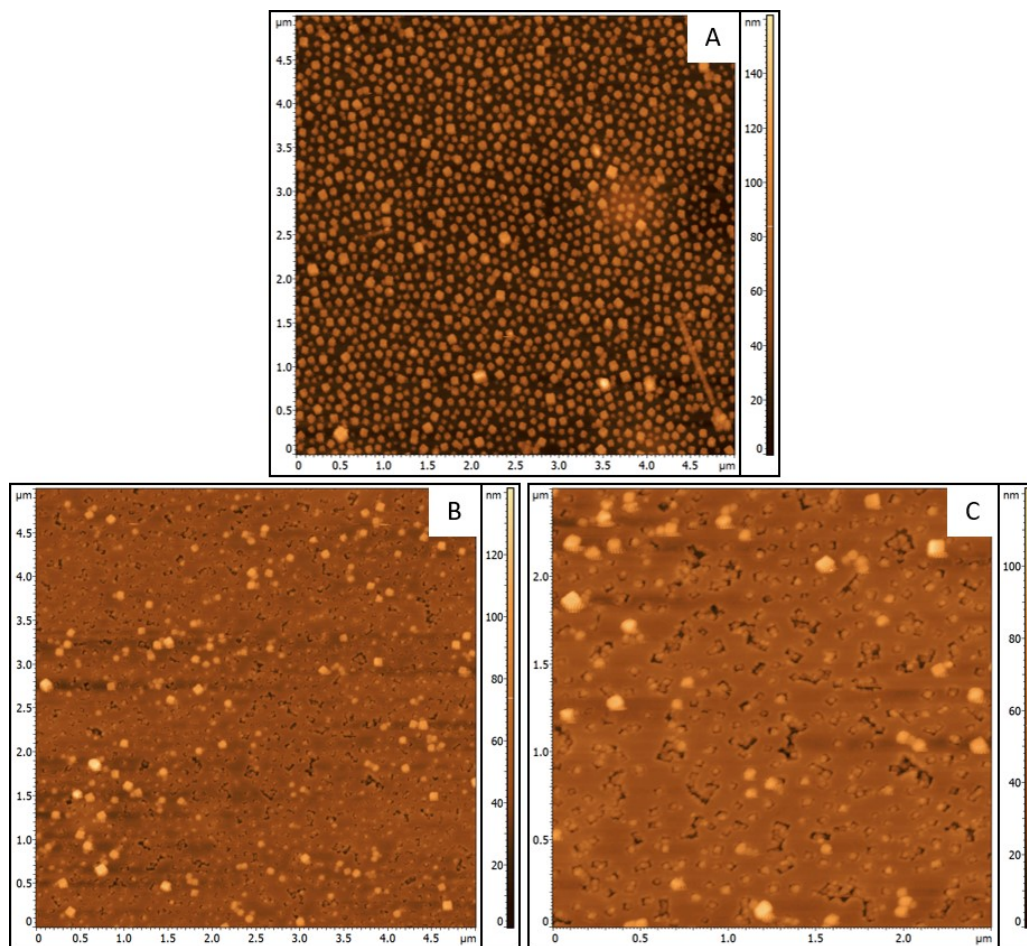


**Figure 3.22:** AFM images of (A) bare AgNC; (B, C) sample S1 after reaction. (B) is a  $5\mu\text{m} \times 5\mu\text{m}$  image and (C) is a  $2.5\mu\text{m} \times 2.5\mu\text{m}$  image of the same sample.

The other two samples S3 and S5 that were not subjected to spinning exhibited significant blue-shifting of the Q and D modes and the disappearance of the M mode (Figure 3.21). The extinction of the suspended particles for sample S3 show a blue shifted dipolar mode and a loss of the multipolar mode (Figure 3.23). These changes indicate that there is a size reduction and loss of cubic shape. Height information acquired through AFM found that there was a height decrease of the nanocubes of 10nm and 3nm for S3 and S5, respectively. TEM images further supported this size and shape change. It was seen that there was significant edge rounding of the AgNC with a very thin shell of SiO<sub>2</sub> characterized with EDS (Figure 3.23). This is due to the low concentration of TEOS used (1% TEOS solution) that resulted in little shell growth and allowed the AgNC to interact more heavily with the ammonia than TEOS.

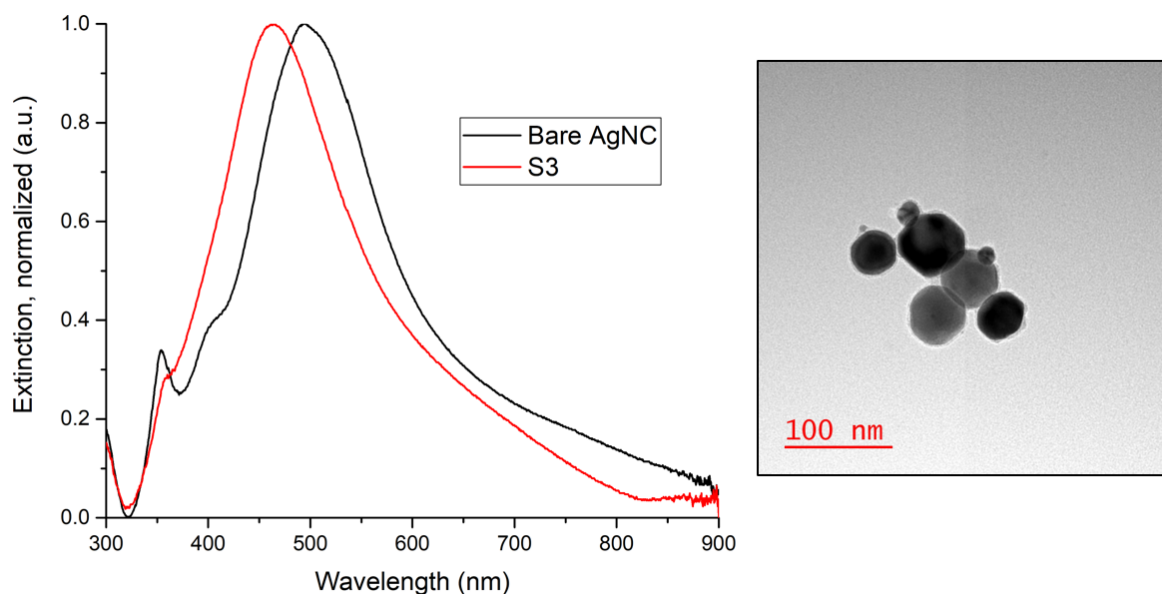


**Figure 3.23:** Left: Extinction of suspended particles. Right: TEM image of sample S3.

In the following set of experiments for samples S6-S9, the number of concentrated TEOS additions was also tested to determine its effect on increasing the shell thickness. Sample S6 had a single 160 $\mu$ L aliquot addition. Samples S7 to S9 had two to four 80 $\mu$ L

aliquots added at even time intervals. The TEOS for S7 was added at 0 minutes and 15 minutes. For S8, TEOS was added at 0, 10, and 20 minutes. S9 had TEOS injections at 0, 7.5, 15, and 22.5 minutes. The embedded particles' extinction spectra of all samples are similar with a merging of the Q and D modes, indicating that an isotropic environment around the AgNC was formed (Figure 3.24). The suspended particles' extinction spectra of samples S7 and S8 in Figure 3.25 show that there is no significant difference between 2 and 3 additions of TEOS and their TEM images highlight similar shell morphology with comparable thicknesses. Sample S7 had a shell thickness of  $10.0 \pm 2.9$  nm and S8 had a thickness of  $11.9 \pm 1.8$  nm. From these few data points it is not conclusive if increasing the number of TEOS additions increases shell thickness. While it has been shown previously that increasing TEOS concentrations increases the thickness of silica shells for particles suspended in solution,<sup>86</sup> it has not been researched for particles immobilized in relatively close proximity on a substrate. This interparticle distance may hinder the formation of thicker shells. To investigate this further, these experiments should be performed on low particle density substrates. However, for the purposes of our study, the silica shells were deemed sufficiently thick.

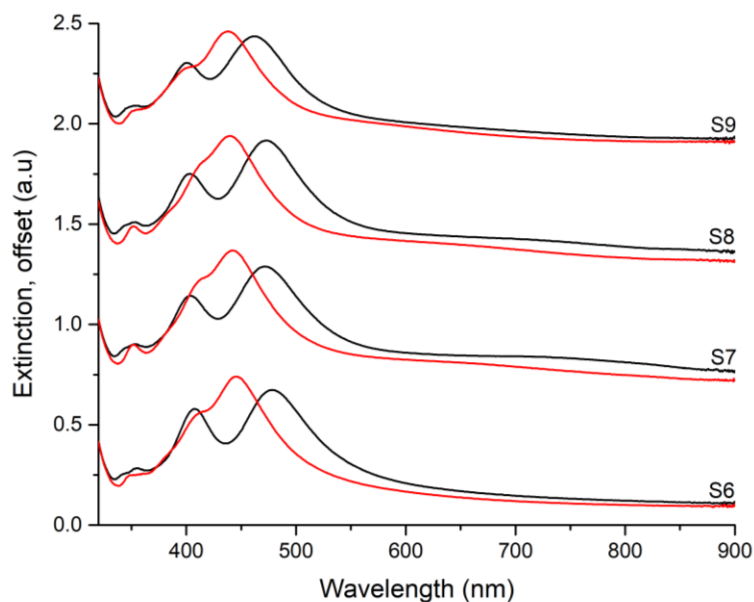


**Figure 3.24:** Extinction spectra of embedded particles before (black) and after (red) reaction. Parameters for each sample is described in Table 4.

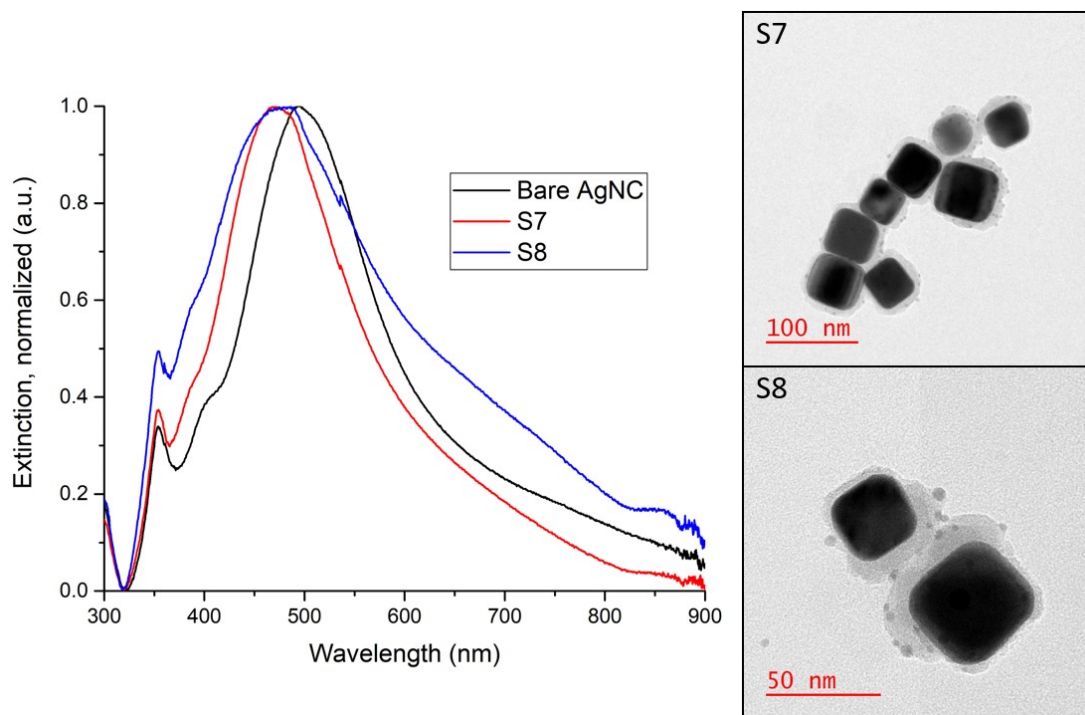


**Figure 3.25:** Left: Extinction spectra of particles suspended in toluene. Right: TEM images of samples S7 and S8.

The following trials were performed to determine if this was a scalable process in order to exploit these particles for practical uses, such as forming dimers for enhanced SERS sensing. The reaction was scaled up two-fold and four-fold for sample slides of twice

and four times the dimensions of previous trials. The extinction spectra were promising with the merging of the Q and D modes as is indicative of SiO<sub>2</sub> shell growth and so the reactions were deemed successful. Following this, a preliminary dimerization reaction was performed in which pentanedithiol (PDT) was used as the linking molecule. The concept was that the thiol at each end of the alkyl chain would bind to the exposed silver of the AgNC/SiO<sub>2</sub> nanoparticle and join two particles together. The AgNC/SiO<sub>2</sub> nanoparticles were removed from the substrate and suspended in a 1mM PDT solution in toluene and left for 17.5 hours. A control sample was performed alongside it wherein AgNC/SiO<sub>2</sub> nanoparticles were suspended in toluene. The extinction spectra of the suspended particles before and after reaction are shown in Figure 3.26. Although, there is no difference in extinction between the control and the sample with PDT before or after the reaction, the TEM images do show that aggregation occurred (Figure 3.27A, B). This, however, did not result in controlled dimer formation, instead forming aggregates on the micro-scale. From higher magnification TEM images, significant SiO<sub>2</sub> undergrowth is observed (Figure 3.27C). The undergrown shell was 35-50% the thickness of the above-grown shell. Since a side effect of this growth method is an etching of the cubic core by ammonia, wherein the produced Ag(NH<sub>3</sub>)<sub>2</sub><sup>+</sup> dissolves in the water/alcohol solution, it is presumed that this etching increases the space between the silver nanocube core and the polystyrene thin film allowing sufficient space for silica formation. This etching is evident from the TEM image in that the AgNC corners have become more truncated after silica growth.

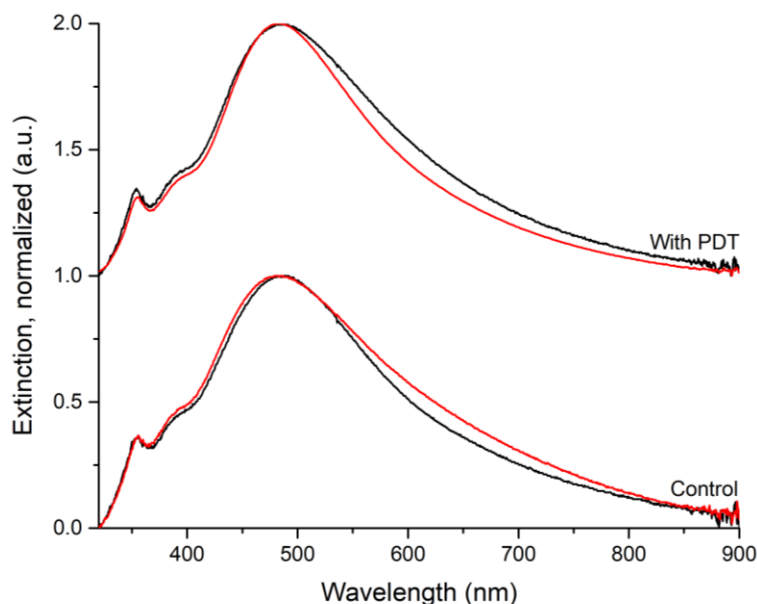


**Figure 3.26:** Extinction spectra of suspended particles before (black) and after (red) reaction.

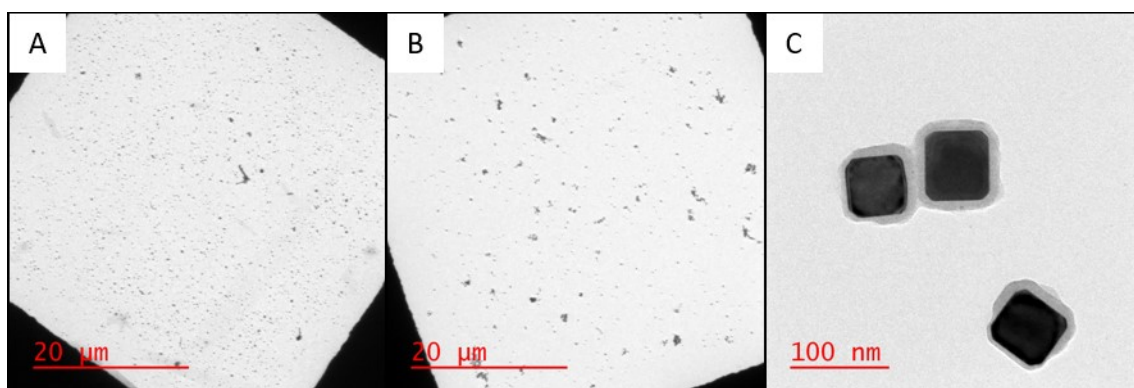


**Figure 3.27:** TEM images of AgNC/SiO<sub>2</sub> particles. (A) Control; (B) Particles with PDT; (C) Higher magnification, control sample.

The following experiments were performed with the aim of eliminating the SiO<sub>2</sub> undergrowth. Samples S24-S27 either utilized less ammonia than previous trials or had a reduced reaction time. Samples S24 and S27 had no ammonia added, with S24 having a reaction time of 24 hours and S27 having a reaction time of 2 hours. Sample S25 had the same volume of ammonia as previous trials but with half the reaction time. Sample S26 used half the volume of ammonia with a 30-minute reaction time. From the extinction spectra (Figure 3.28), it is observed that S24 had a complete loss of LSPR and it is

presumably due to the PS film dissolving in the isopropanol over the 24 hours. Samples S25 and S26 exhibited the typical Q and D mode merging indicating growth. And sample S27 had slight Q mode blue shift and D mode red shift. The TEM images found that there was still undergrowth that occurred for S25 and S26 whereas no growth occurred at all for S27 (Figure 3.29).

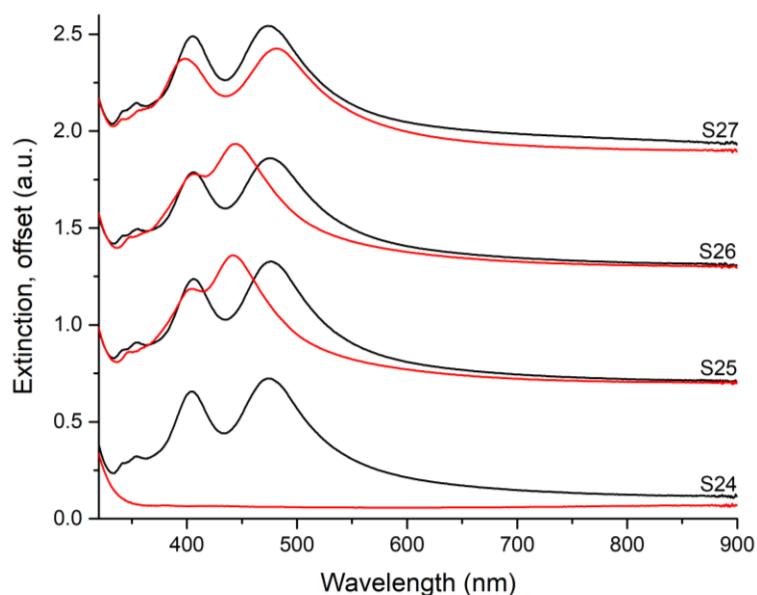


**Figure 3.28:** Extinction spectra of embedded particles before (black) and after (red) reaction. Parameters for each sample is described in Table 4.

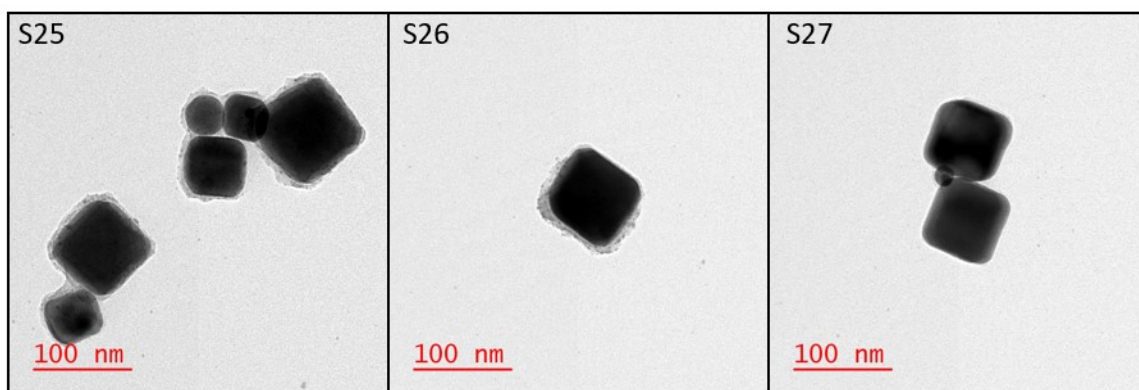


**Figure 3.29:** TEM images of samples S25-S27.

Another set of tests aimed at reducing the undergrowth through the use of an acid catalyst instead of the ammonia base catalyst. Both trials, S28 and S29, used HCl as the catalyst

with S28 having a 30-minute reaction time and S29 having a 2-hour reaction time. The extinction spectra show a blue shift of both Q and D mode with S29 having a more significant shift (Figure 3.30). The TEM images did not show shell growth or any change in AgNC size or shape, therefore this blue shift could be due to the interaction with the substrate.

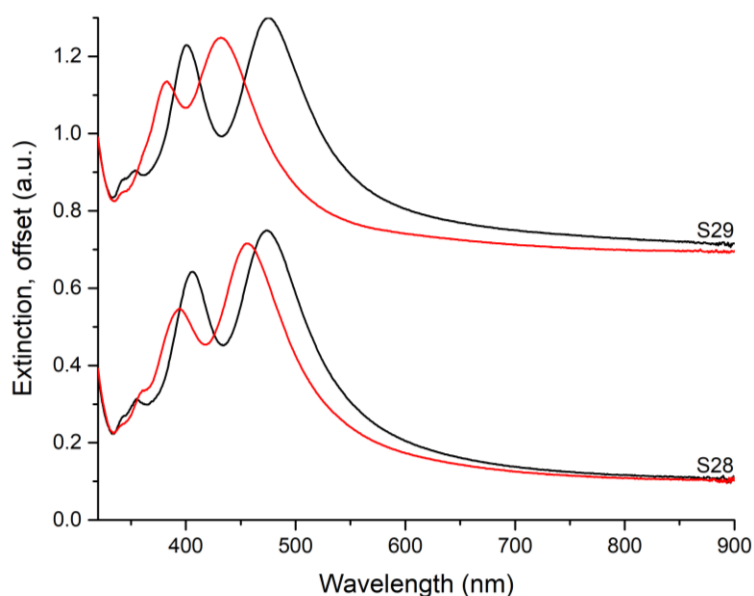


**Figure 3.30:** Extinction spectra of embedded particles before (black) and after (red) reaction. Parameters for each sample is described in Table 4.

Negative control trials were performed to assess the changes in the AgNC extinction that would occur without TEOS. These were performed using isopropanol (IPA) as the solvent and all were left submerged for 30 minutes. Sample S-C1 was immersed in IPA, S-C2 was immersed in IPA and water, and S-C3 was reacted with IPA, water, and ammonia. S-C1 and S-C2 showed some blue shifting of the Q and D modes whereas S-C3 exhibited significant Q and D mode blue shifting and loss of the M mode (Figure 3.31). This is of course due to the dissolution of the silver following reaction with ammonia as discussed earlier.

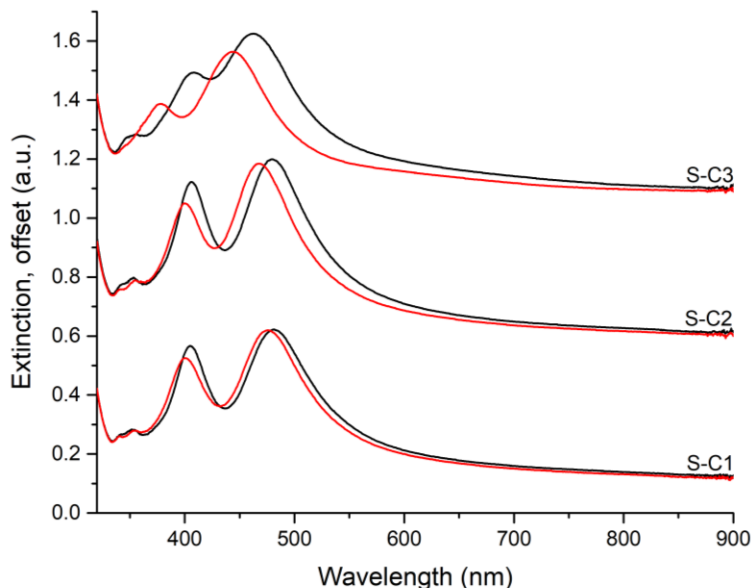


**Figure 3.31:** Extinction spectra of embedded particles before (black) and after (red) completion of control experiments. Parameters for each sample is described in Table 4.

In summary, there was the scalable production of complete shells around embedded particles. And while this was not the desired outcome, this does present an interesting method for reliable in-solution growth of thin, conformal silica shells. Additionally, it was found that spinning the sample slide resulted in loss of AgNCs, leaving behind their imprint and prompting an interesting approach to the formation of cavities of a defined shape. It was also determined that the amount of TEOS added to this system did not greatly impact the shell thickness therefore providing a robust method for conformal SiO<sub>2</sub> shell growth.

### 3.5 Cuprous oxide shell

In this section, the growth of cuprous oxide shells is investigated as it pertained to the effect of reagent concentrations, the effect of precursor injection method, the role of lactic acid, the manipulation of the order of reagent addition, the impact of a different copper salt on morphology, as well as the effect of cube coverage on the optical properties of the core. FDTD simulations were also performed to gain a deeper insight into the

theoretical effect of Cu<sub>2</sub>O half-shells on AgNC. The reaction parameters for each set of trials is shown in Table 5.

**Table 5:** Reaction parameters for cuprous oxide growth

| Section ID | Cu salt                           | *Volume (μL) or Concentration |     |        |                               |      | Order of addition                            | Injection method                         |
|------------|-----------------------------------|-------------------------------|-----|--------|-------------------------------|------|--|--|
|            |                                   | NaOH                          | LA  | Cu     | N <sub>2</sub> H <sub>4</sub> | AA   |  |  |
| 3.5.2      | Cu(NO <sub>3</sub> ) <sub>2</sub> | 350                           | 350 | 17.5mM | 220                           |      | NaOH, LA, N <sub>2</sub> H <sub>4</sub> , Cu | Stepwise Cu                              |
|            | Cu(NO <sub>3</sub> ) <sub>2</sub> | 450                           | 450 | 22.5mM | 220                           |      | NaOH, LA, N <sub>2</sub> H <sub>4</sub> , Cu |  |
|            | Cu(NO <sub>3</sub> ) <sub>2</sub> | 550                           | 550 | 27.5mM | 220                           |      | NaOH, LA, N <sub>2</sub> H <sub>4</sub> , Cu |  |
|            | Cu(NO <sub>3</sub> ) <sub>2</sub> | 650                           | 650 | 32.5mM | 220                           |      | NaOH, LA, N <sub>2</sub> H <sub>4</sub> , Cu |  |
|            | Cu(NO <sub>3</sub> ) <sub>2</sub> | 750                           | 750 | 37.5mM | 220                           |      | NaOH, LA, N <sub>2</sub> H <sub>4</sub> , Cu |  |
|            | Cu(NO <sub>3</sub> ) <sub>2</sub> | 850                           | 850 | 42.5mM | 220                           |      | NaOH, LA, N <sub>2</sub> H <sub>4</sub> , Cu |  |
| 3.5.3      | Cu(NO <sub>3</sub> ) <sub>2</sub> | 650                           | 650 | 32.5mM | 220                           |      | NaOH, LA, N <sub>2</sub> H <sub>4</sub> , Cu | Stepwise Cu                              |
|            | Cu(NO <sub>3</sub> ) <sub>2</sub> | 650                           | 650 | 32.5mM | 220                           |      | NaOH, LA, N <sub>2</sub> H <sub>4</sub> , Cu | Continuous Cu                            |
|            | Cu(NO <sub>3</sub> ) <sub>2</sub> | 650                           | 650 | 32.5mM | 220                           |      | NaOH, LA, N <sub>2</sub> H <sub>4</sub> , Cu | Continuous Cu<br>1/2 rate and volume     |
| 3.5.4      | Cu(NO <sub>3</sub> ) <sub>2</sub> | 650                           | 650 | 32.5mM | 220                           |      | NaOH, LA, N <sub>2</sub> H <sub>4</sub> , Cu | Continuous Cu                            |
|            | Cu(NO <sub>3</sub> ) <sub>2</sub> | 650                           |     | 32.5mM | 220                           |      | NaOH, N <sub>2</sub> H <sub>4</sub> , Cu     |  |
| 3.5.5.1    | Cu(NO <sub>3</sub> ) <sub>2</sub> | 450                           |     | 450    | 0.55%                         |      | NaOH, Cu, N <sub>2</sub> H <sub>4</sub>      | Continuous N <sub>2</sub> H <sub>4</sub> |
|            | Cu(NO <sub>3</sub> ) <sub>2</sub> | 550                           |     | 550    | 0.55%                         |      | NaOH, Cu, N <sub>2</sub> H <sub>4</sub>      |  |
|            | Cu(NO <sub>3</sub> ) <sub>2</sub> | 650                           |     | 650    | 0.55%                         |      | NaOH, Cu, N <sub>2</sub> H <sub>4</sub>      |  |
|            | Cu(NO <sub>3</sub> ) <sub>2</sub> | 750                           |     | 750    | 0.55%                         |      | NaOH, Cu, N <sub>2</sub> H <sub>4</sub>      |  |
| 3.5.5.2    | Cu(NO <sub>3</sub> ) <sub>2</sub> | 450                           | 450 | 450    | 0.55%                         |      | NaOH, Cu, LA, N <sub>2</sub> H <sub>4</sub>  | Continuous N <sub>2</sub> H <sub>4</sub> |
|            | Cu(NO <sub>3</sub> ) <sub>2</sub> | 450                           |     | 450    | 0.55%                         |      | NaOH, Cu, N <sub>2</sub> H <sub>4</sub>      |  |
|            | Cu(NO <sub>3</sub> ) <sub>2</sub> | 650                           | 650 | 650    | 0.55%                         |      | NaOH, Cu, LA, N <sub>2</sub> H <sub>4</sub>  |  |
|            | Cu(NO <sub>3</sub> ) <sub>2</sub> | 650                           |     | 650    | 0.55%                         |      | NaOH, Cu, N <sub>2</sub> H <sub>4</sub>      |  |
| 3.5.6      | CuSO <sub>4</sub>                 | 650                           | 650 | 32.5mM | 220                           |      | NaOH, LA, N <sub>2</sub> H <sub>4</sub> , Cu | Continuous Cu                            |
|            | CuSO <sub>4</sub>                 | 650                           | 650 | 650    | 220                           |      | Cu, NaOH, LA, N <sub>2</sub> H <sub>4</sub>  | All fast addition                        |
|            | CuSO <sub>4</sub>                 | 650                           |     | 650    |                               | 1000 | Cu, NaOH, AA                                 | All fast addition                        |
|            | CuSO <sub>4</sub>                 | 650                           | 650 | 650    |                               | 1000 | Cu, NaOH, LA, AA                             | All fast addition                        |
|            | CuSO <sub>4</sub>                 | 650                           | 650 | 650    | 0.55%                         |      | NaOH, Cu, LA, N <sub>2</sub> H <sub>4</sub>  | Continuous N <sub>2</sub> H <sub>4</sub> |
| 3.5.7      | Cu(NO <sub>3</sub> ) <sub>2</sub> | 450                           | 450 | 22.5mM | 220                           |      | NaOH, LA, N <sub>2</sub> H <sub>4</sub> , Cu | Continuous Cu                            |
|            | Cu(NO <sub>3</sub> ) <sub>2</sub> | 450                           | 450 | 22.5mM | 220                           |      | NaOH, LA, N <sub>2</sub> H <sub>4</sub> , Cu |  |
|            | Cu(NO <sub>3</sub> ) <sub>2</sub> | 450                           | 450 | 22.5mM | 220                           |      | NaOH, LA, N <sub>2</sub> H <sub>4</sub> , Cu |  |
|            | Cu(NO <sub>3</sub> ) <sub>2</sub> | 450                           | 450 | 22.5mM | 220                           |      | NaOH, LA, N <sub>2</sub> H <sub>4</sub> , Cu |  |
|            | Cu(NO <sub>3</sub> ) <sub>2</sub> | 650                           | 650 | 32.5mM | 220                           |      | NaOH, LA, N <sub>2</sub> H <sub>4</sub> , Cu |  |
|            | Cu(NO <sub>3</sub> ) <sub>2</sub> | 650                           | 650 | 32.5mM | 220                           |      | NaOH, LA, N <sub>2</sub> H <sub>4</sub> , Cu |  |
|            | Cu(NO <sub>3</sub> ) <sub>2</sub> | 650                           | 650 | 32.5mM | 220                           |      | NaOH, LA, N <sub>2</sub> H <sub>4</sub> , Cu |  |
|            | Cu(NO <sub>3</sub> ) <sub>2</sub> | 650                           | 650 | 32.5mM | 220                           |      | NaOH, LA, N <sub>2</sub> H <sub>4</sub> , Cu |  |

\*Unless otherwise stated, the concentrations were as follows: 5M NaOH, 4M lactic acid (LA), 0.5M Cu salt, 25% N<sub>2</sub>H<sub>4</sub>, and 1.13M ascorbic acid (AA).

### 3.5.1 FDTD simulated results

FDTD simulations, provided by Daniel Prezgot and Mike Bushell, were performed for a 60nm AgNC with pyramidal and cubic half-shells. The first simulations shown in Figure 3.32 are of bare AgNC (without a shell) for a particle half-way embedded in the

polystyrene (PS) thin film and of the particle suspended in solution. In both cases, we can observe the presence of the quadrupolar (Q) and dipolar (D) modes. The other extinction spectra in Figure 3.32 are of an AgNC with a pyramidal shell that covers half of the core. The extinction of the particle half-way embedded in the polystyrene (PS) thin film and of the particle suspended in solution are provided. For the particle embedded in PS, in comparison to its bare AgNC counterpart, there is a red shift of the Q and D modes such that the Q mode merges into the D mode. As for the particle suspended in solution, there is a red shift of the D mode. The E-fields of the of the simulated AgNC/Cu<sub>2</sub>O particles are provided in Figure 3.33 and show that the dipolar mode is localized toward the area of higher refractive index, Cu<sub>2</sub>O, and the Q mode is localized toward the area of lower refractive index, the PS or the vacuum.

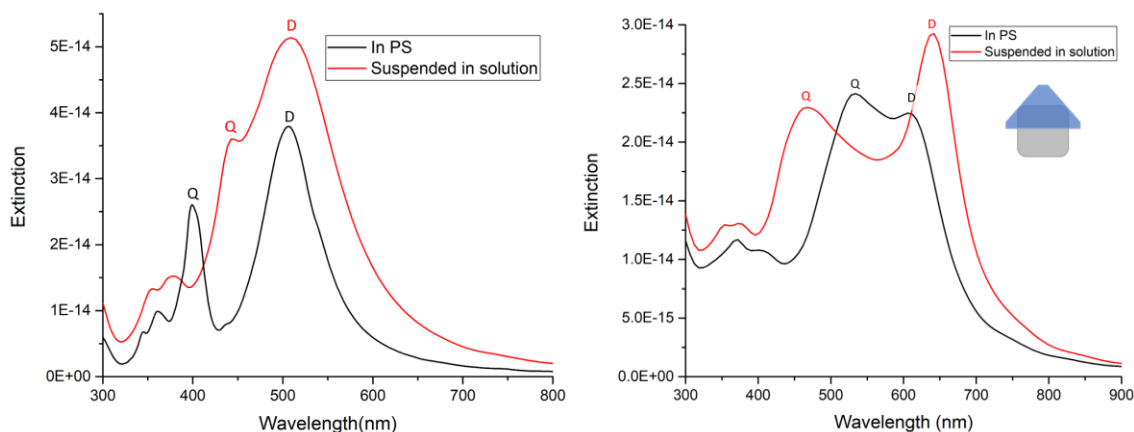


**Figure 3.32:** FDTD simulation of (left) bare AgNC and (right) AgNC with pyramidal Cu<sub>2</sub>O half-shell.

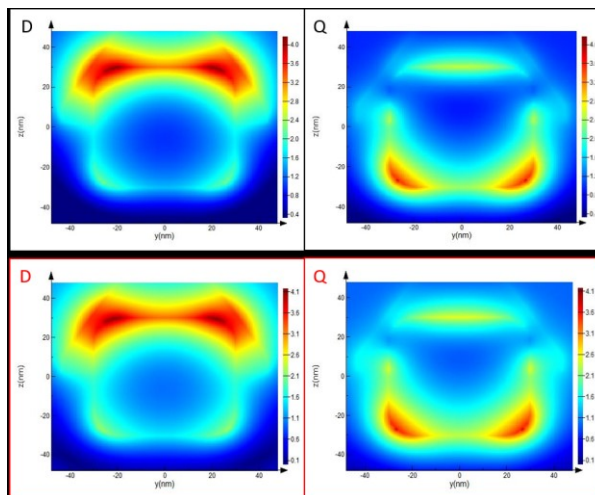


**Figure 3.33:** E-fields of 60nm AgNC with pyramidal Cu<sub>2</sub>O half-shell (covering the top half of the AgNC) for the dipolar and quadrupolar resonances. Top: Particle embedded in PS. Bottom: Particle suspended in solution.

The following simulations look into the impact of shell coverage on the optical properties of the core/partial-shell particle (Figure 3.34). As the amount of AgNC covered is reduced, as in having only the very top of the AgNC coated, the Q and D mode peak separation increases. This peak separation is indicative of plasmon hybridization and so the experimental production of these minimally coated particles is attractive and is attempted in section 3.5.7.

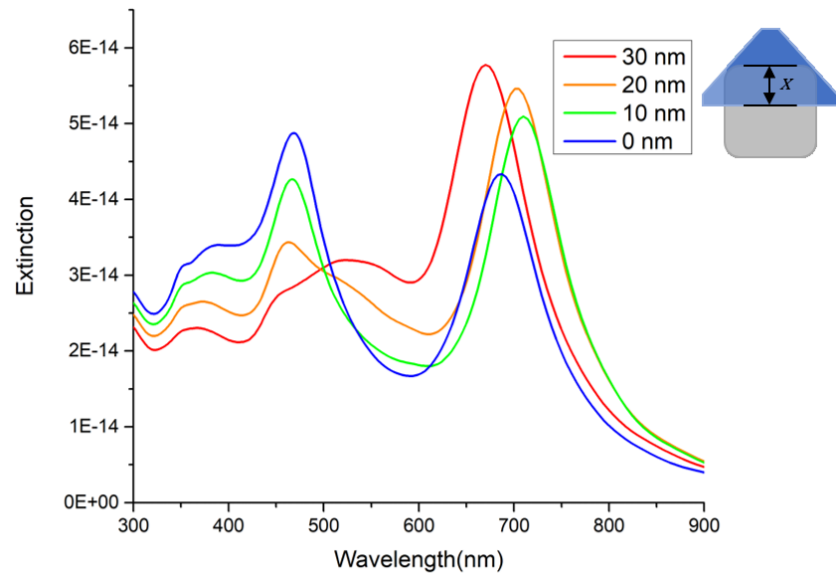


**Figure 3.34:** FDTD simulated extinction of 60nm AgNC with pyramidal  $\text{Cu}_2\text{O}$  shell with varied AgNC surface coverage. The legend indicates the amount of AgNC covered from the top of the cube (labeled  $x$  in the illustration).

It is also important to understand the effect of shell thickness on the optical properties of the particle. The simulations of a 60 nm AgNC with a cubic shell of varying thicknesses for particles embedded in PS and particles suspended in solution are provided in Figure 3.35 and Figure 3.36, respectively. It is observed that as the shell thickness increases, the dipolar and quadrupolar modes red shift and there is increased extinction below 450 nm wavelength. This increase is from the light absorption of copper and the red shift is due to the high refractive index. These trends are observed experimentally in the following sections.

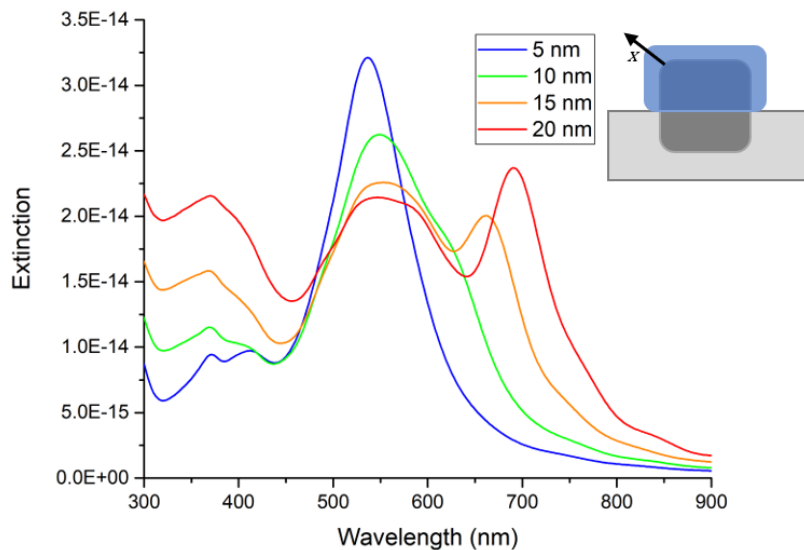


**Figure 3.35:** FDTD simulated extinction of 60nm AgNC with cubic Cu<sub>2</sub>O shell of varied thickness. The legend indicates shell thickness (labeled  $x$  in the illustration). These spectra are for particles half-way embedded in polystyrene.

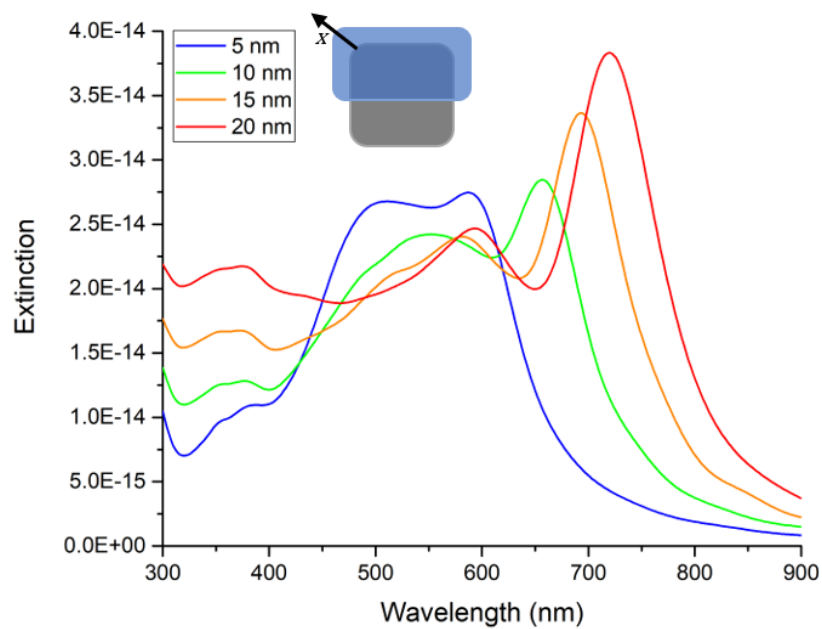


**Figure 3.36:** FDTD simulated extinction of 60nm AgNC with cubic Cu<sub>2</sub>O shell of varied thickness. The legend indicates shell thickness (labeled  $x$  in the illustration). These spectra are for particles suspended in solution.

### 3.5.2 Effect of reagent concentration

| Section ID | Cu salt                    | Volume ( $\mu\text{L}$ ) or Concentration |     |        |                        | Order of addition                     | Injection method |
|------------|----------------------------|---|-----|--------|------------------------|---------------------------------------|------------------|
|            |                            | NaOH                                      | LA  | Cu     | $\text{N}_2\text{H}_4$ |                                       |                  |
| 3.5.2      | $\text{Cu}(\text{NO}_3)_2$ | 350                                       | 350 | 17.5mM | 220                    | NaOH, LA, $\text{N}_2\text{H}_4$ , Cu | Stepwise Cu      |
|            | $\text{Cu}(\text{NO}_3)_2$ | 450                                       | 450 | 22.5mM | 220                    | NaOH, LA, $\text{N}_2\text{H}_4$ , Cu |                  |
|            | $\text{Cu}(\text{NO}_3)_2$ | 550                                       | 550 | 27.5mM | 220                    | NaOH, LA, $\text{N}_2\text{H}_4$ , Cu |                  |
|            | $\text{Cu}(\text{NO}_3)_2$ | 650                                       | 650 | 32.5mM | 220                    | NaOH, LA, $\text{N}_2\text{H}_4$ , Cu |                  |
|            | $\text{Cu}(\text{NO}_3)_2$ | 750                                       | 750 | 37.5mM | 220                    | NaOH, LA, $\text{N}_2\text{H}_4$ , Cu |                  |
|            | $\text{Cu}(\text{NO}_3)_2$ | 850                                       | 850 | 42.5mM | 220                    | NaOH, LA, $\text{N}_2\text{H}_4$ , Cu |                  |

Varied amounts of reagents were tested to determine optimal conditions for shell growth. The tested volumes of 5M NaOH and 4M lactic acid were 350, 450, 550, 650, 750, 850  $\mu\text{L}$ , and the corresponding  $\text{Cu}(\text{NO}_3)_2$  concentrations were 17.5, 22.5, 27.5, 32.5, 37.5, 42.5 mM. Ten millilitres of the  $\text{Cu}(\text{NO}_3)_2$  solution were added in a stepwise manner, meaning 1mL was added at 5-minute intervals. All received 220 $\mu\text{L}$  of 25% hydrazine.

Before reaction, the multipolar, quadrupolar, and dipolar modes had wavelengths of 353, 407, and 476 nm, respectively, for AgNC embedded in PS supported on glass (Figure 3.37). As the amount of reagents increased, a significant change in the extinction spectra was seen. For the trials denoted as 350 $\mu\text{L}$ , 17.5mM and 450 $\mu\text{L}$ , 22.5mM in Figure 3.37, there is a red shift of the dipolar mode from the original 476nm to 495nm and a depletion of the quadrupolar mode. For the remaining trials, there is the evolution of new peaks as the reagent amounts are further increased. The final spectrum (850 $\mu\text{L}$ , 42.5mM) shows five distinct peaks located at 353nm, 407nm, 473nm, 561nm, and 626nm. The highest energy peak (353nm) is due to the multipolar mode of the AgNC. It is believed that other four peaks arise from a mix of lesser and greater coated AgNC within a single sample. The presumption is that the 407nm and 473nm peaks are the Q and D modes of uncoated or lesser coated AgNC while the 561nm and the 626nm peaks are the Q and D peaks of the

more fully coated AgNC. The red shift of the quadrupolar and dipolar modes is expected since the refractive index of local environment above the polystyrene is increasing. For clarity, the red shifted quadrupolar and dipolar modes will be labeled Q' and D'. The experimental spectrum is in approximate agreement with the simulated spectra in section 3.5.1 in that the Q' and D' modes correspond to the FDTD simulated quadrupolar and dipolar modes.

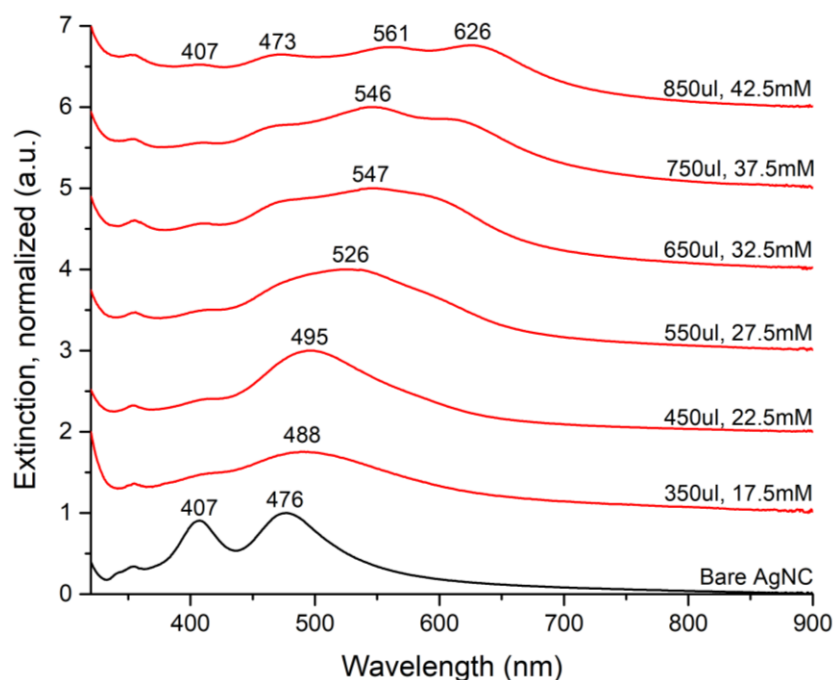


**Figure 3.37:** Extinction spectra of embedded AgNC in PS, before (black) and after (red) reaction.

The TEM images in Figure 3.38 show the copper oxide growth on the AgNC for the samples that had 450 $\mu$ L, 22.5mM; 650 $\mu$ L, 32.5mM; and 850 $\mu$ L, 42.5mM for the respective reagents as described above. The corresponding shell thicknesses are  $13.9 \pm 5.8$  nm (103 measurements),  $21.9 \pm 6.9$  nm (240 measurements), and  $24.9 \pm 6.8$  nm (209 measurements). Therefore, as the amount of reagents increase so does the shell thickness. However, there are constraints to this thickness increase, such as interparticle distance of

the AgNC core. If the AgNCs have a small interparticle distance, the shell will not be as thick compared to AgNCs that are widely spaced apart.

In addition to shell thickness, the growth process and morphology of these Cu<sub>2</sub>O half-shells are observed. As we go from low to high reagent amounts, a very polycrystalline and incomplete half-shell progresses to a more quasi-monocrystalline and complete half-shell. It is evident from the TEM images that a half-shell with a distinct pyramidal morphology is produced.

The extinction spectra in Figure 3.38 are of the particles removed from the substrate and suspended in toluene. With increased reagents, and therefore increased shell thickness, a red shift of the dipolar mode from the original 505nm to 683nm is exhibited. There is also the development of an additional peak at 470nm which corresponds to the quadrupolar mode observed in the FDTD simulations in Figure 3.32. It is therefore concluded that in-solution hybridization has been achieved with AgNC/Cu<sub>2</sub>O core/half-shell nanoparticles.

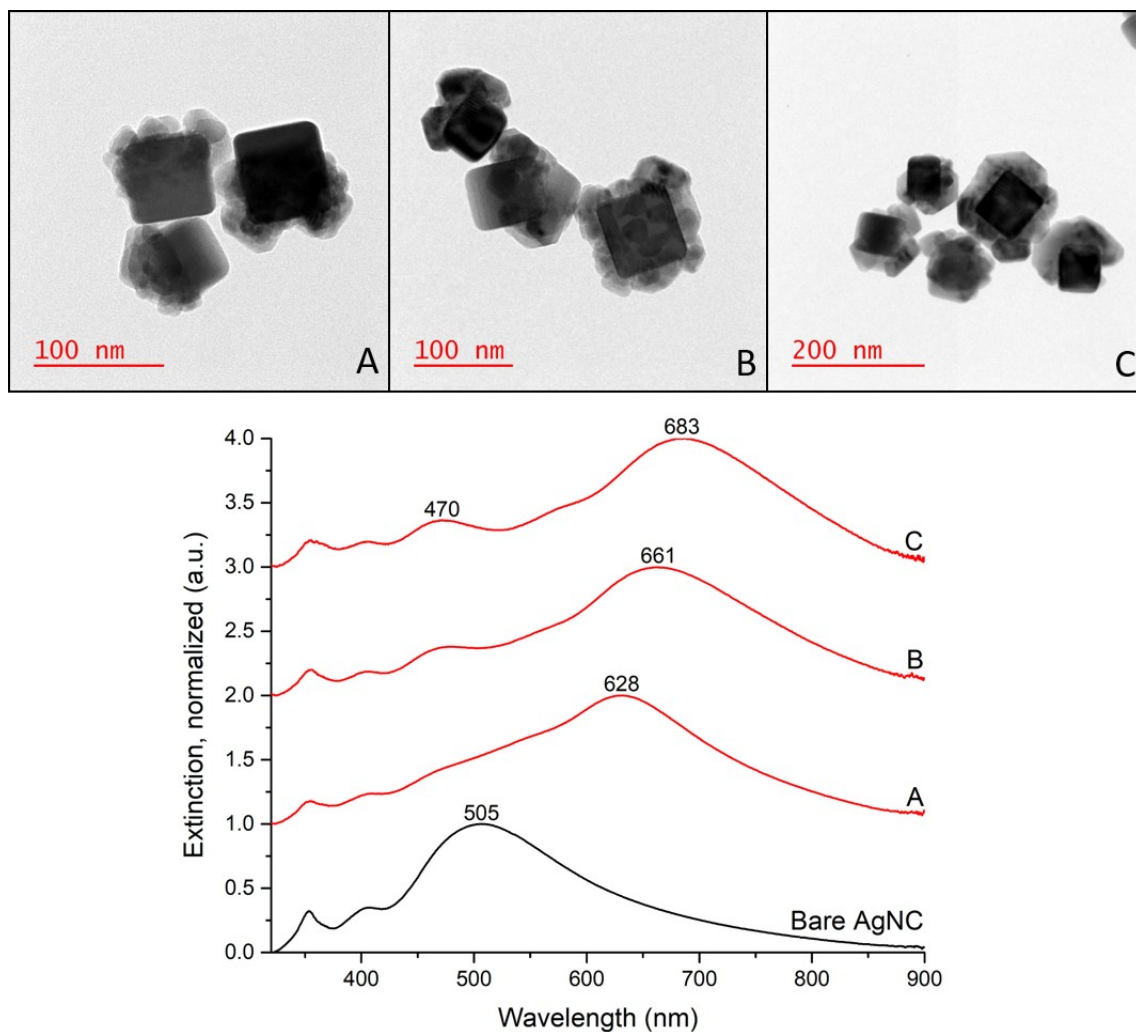


**Figure 3.38:** Above: TEM images of AgNC/Cu<sub>2</sub>O nanoparticles. Below: Extinction spectra of particles suspended in toluene. Black curve indicates bare AgNC, red curves indicate AgNC/Cu<sub>2</sub>O nanoparticles. (A) 450 $\mu$ L NaOH, LA and 22.5mM Cu(NO<sub>3</sub>)<sub>2</sub>; (B) 650 $\mu$ L NaOH, LA and 32.5mM Cu(NO<sub>3</sub>)<sub>2</sub>; (C) 850 $\mu$ L NaOH, LA and 42.5mM Cu(NO<sub>3</sub>)<sub>2</sub>, with the Q mode present at 407 nm and the D mode present at 683 nm.

### 3.5.3 Stepwise addition versus continuous injection

| Section ID | Cu salt                           | Volume ( $\mu$ L) or Concentration |     |        |                               | Order of addition                            | Injection method                     |
|------------|-----------------------------------|------------------------------------|-----|--------|-------------------------------|--|--------------------------------------|
|            |                                   | NaOH                               | LA  | Cu     | N <sub>2</sub> H <sub>4</sub> |  |                                      |
| 3.5.3      | Cu(NO <sub>3</sub> ) <sub>2</sub> | 650                                | 650 | 32.5mM | 220                           | NaOH, LA, N <sub>2</sub> H <sub>4</sub> , Cu | Stepwise Cu                          |
|            | Cu(NO <sub>3</sub> ) <sub>2</sub> | 650                                | 650 | 32.5mM | 220                           | NaOH, LA, N <sub>2</sub> H <sub>4</sub> , Cu | Continuous Cu                        |
|            | Cu(NO <sub>3</sub> ) <sub>2</sub> | 650                                | 650 | 32.5mM | 220                           | NaOH, LA, N <sub>2</sub> H <sub>4</sub> , Cu | Continuous Cu<br>1/2 rate and volume |

The objective of the following trials was to obtain more complete half-shells to increase the reliability for dimer formation. The injection method of the copper precursor

was changed from stepwise to continuous addition, utilizing a syringe pump to inject 10mL of  $\text{Cu}(\text{NO}_3)_2$  at a rate of 0.2 mL/min. From the extinction spectra of the embedded particles (Figure 3.39 A, B), when comparing the stepwise addition and continuous injection, the continuous injection method results in more pronounced resolution of the Q, D, Q', and D' peaks as well as a significant red shift of the D' mode from 547 nm to 633 nm. From the analysis of the TEM images acquired (Figure 3.40 A, B), it was found that the stepwise addition and the continuous injection methods yielded  $21.9 \pm 6.9$  nm (240 measurements) and  $32.4 \pm 8.4$  nm (270 measurements) thick shells, respectively. Both of these methods produce shells with a pyramidal morphology. As introduced in section 1.4.5.1, the growth mechanism is as follows: (i) nucleation of  $\text{Cu}_2\text{O}$  nanoparticles on the metal core; (ii)  $\text{Cu}_2\text{O}$  nanoparticle growth; (iii) crystal reconstruction to relieve stress. And as such, as growth progresses, the shell becomes less polycrystalline until a monocrystalline shell is obtained. The shells produced from the continuous injection method were thicker and had less polycrystallinity, though complete monocrystalline shells were not obtained. In order to further decrease the polycrystallinity, the volume of  $\text{Cu}(\text{NO}_3)_2$  was decreased to 5mL and the rate was reduced to 0.1 mL/min, maintaining a total reaction time of 55 minutes. Through these changes it was suspected that the slower introduction of copper precursor would allow crystal reconstruction to proceed without  $\text{Cu}_2\text{O}$  nucleation dominating the growth process. However, it was found that shells  $36.2 \pm 8.2$  nm (86 measurements) in thickness were formed with increased polycrystallinity. Interestingly, the extinction spectrum of the embedded particles (Figure 3.39 C) did not exhibit as significant of a red shift of the D' mode (585 nm) even though the shell thickness was comparable to that of

the 10mL, 0.2mL/min trial (Figure 3.40 C). This was presumably due to the higher polycrystallinity of the 5mL, 0.1mL/min trial.

The extinction spectra of the AgNC/Cu<sub>2</sub>O nanoparticles suspended in toluene (Figure 3.40) show in-solution hybridization for all trials with the most significant peak separation occurring for the continuous injection method with 10mL of Cu(NO<sub>3</sub>)<sub>2</sub> with a rate of 0.2 mL/min.

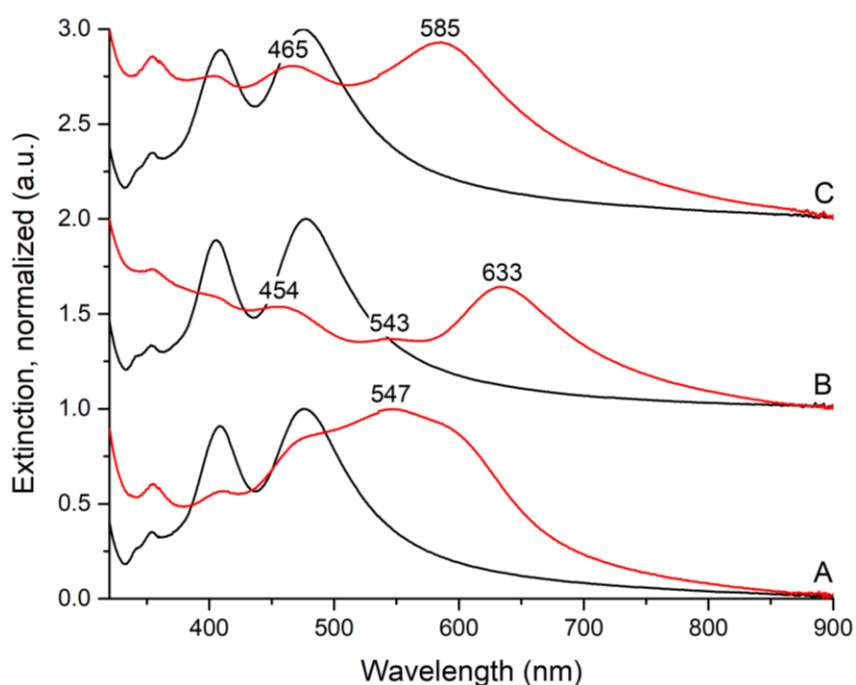


**Figure 3.39:** Extinction spectra of embedded AgNC before (black) and after (red) reaction. (A) Stepwise Cu(NO<sub>3</sub>)<sub>2</sub> addition (B) Continuous Cu(NO<sub>3</sub>)<sub>2</sub> addition, 10mL added at 0.2mL/min (C) Continuous Cu(NO<sub>3</sub>)<sub>2</sub> addition, 5mL added at 0.1mL/min

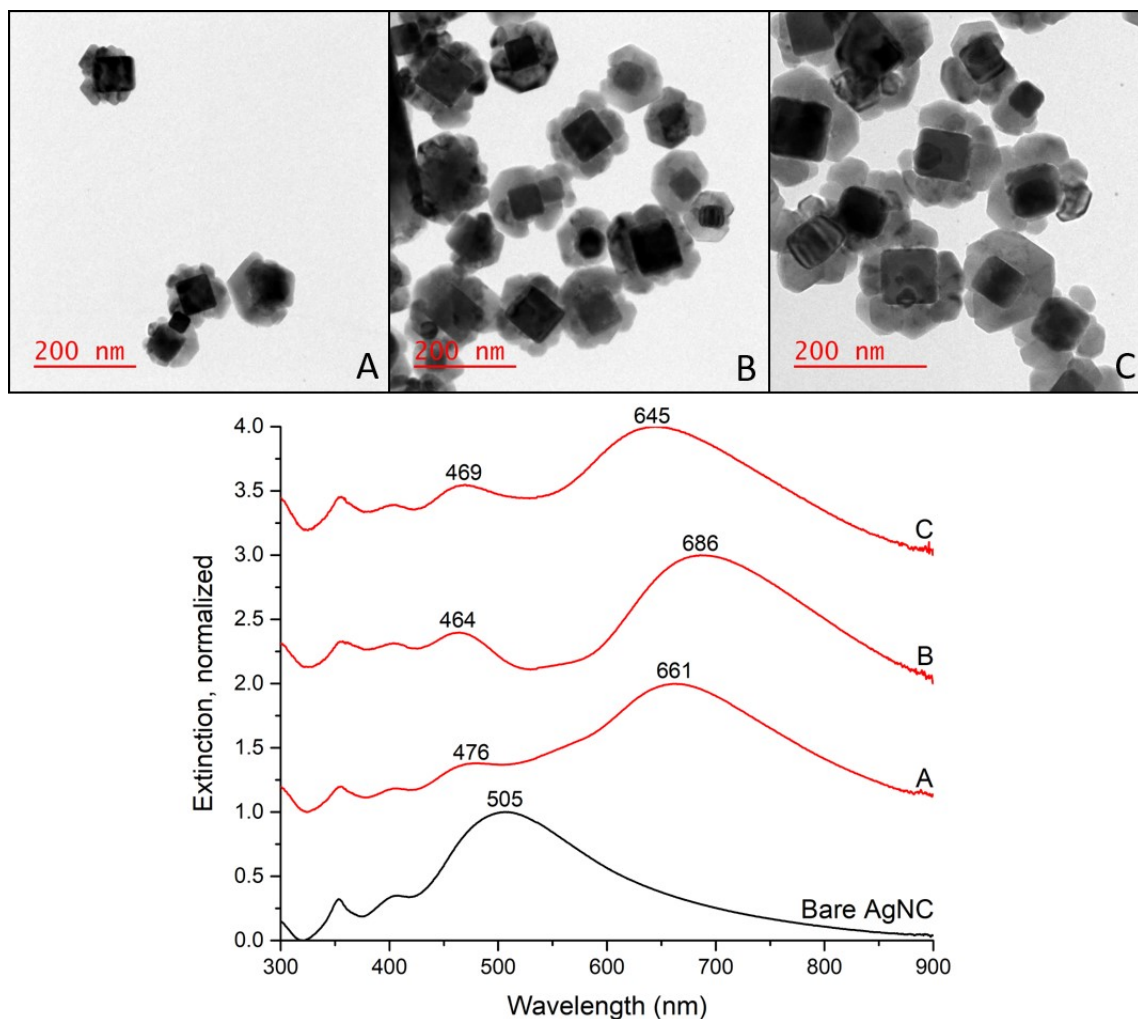


**Figure 3.40:** Above: TEM images of AgNC/Cu<sub>2</sub>O nanoparticles. Below: Extinction spectra of particles suspended in toluene. Black curve indicates bare AgNC, red curves indicate AgNC/Cu<sub>2</sub>O nanoparticles. (A) Stepwise addition of 32.5mM Cu(NO<sub>3</sub>)<sub>2</sub>, 10mL, 1mL every 5 minutes; (B) Continuous addition of 32.5mM Cu(NO<sub>3</sub>)<sub>2</sub>, 10mL at 0.2mL/min; (C) Continuous addition of 32.5mM Cu(NO<sub>3</sub>)<sub>2</sub>, 5mL at 0.2mL/min.

### 3.5.4 Role of lactic acid

| Section ID | Cu salt                           | Volume (μL) or Concentration |     |        |                               | Order of addition                            | Injection method |
|------------|-----------------------------------|------------------------------|-----|--------|-------------------------------|--|------------------|
|            |                                   | NaOH                         | LA  | Cu     | N <sub>2</sub> H <sub>4</sub> |  |                  |
| 3.5.4      | Cu(NO <sub>3</sub> ) <sub>2</sub> | 650                          | 650 | 32.5mM | 220                           | NaOH, LA, N <sub>2</sub> H <sub>4</sub> , Cu | Continuous Cu    |
|            | Cu(NO <sub>3</sub> ) <sub>2</sub> | 650                          | NA  | 32.5mM | 220                           | NaOH, N <sub>2</sub> H <sub>4</sub> , Cu     |                  |

Tests were performed with and without lactic acid to determine its role in the cuprous oxide growth. Continuous copper nitrate injection was tested with and without lactic acid and it was determined that lactic acid plays a role in the kinetics of the reaction.

The pH of the solution with LA was 10.5, while without LA the pH was 11.9. The extent of growth is observed in the extinction spectra of embedded (Figure 3.41) and suspended (Figure 3.42) particles. For trials without lactic acid, the growth was not as extensive and is equivalent to that of trials utilizing lactic acid with reduced amounts of reagents.

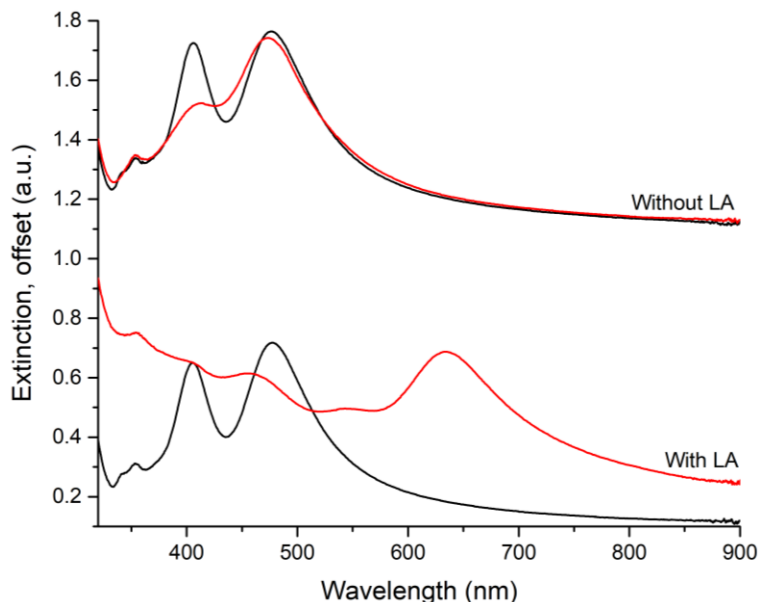


**Figure 3.41:** Extinction spectra of embedded AgNC before (black) and after (red) reaction with and without lactic acid.

From the TEM images obtained (Figure 3.42), it was found that with lactic acid, the shells were on average  $32.4 \pm 8.4$  nm (270 measurements) thick with complete coverage of the exposed silver. For the growth without lactic acid, shells with a thickness of  $14.5 \pm 5.6$  nm (43 measurements) were obtained and energy-dispersive x-ray spectroscopy (EDS) showed a ratio of Cu:O of 1.8:1 determined from atomic percent measurements. This growth did not result in complete coverage of the silver, just distinct  $\text{Cu}_2\text{O}$  NPs grown on the exposed silver. Therefore, it is confirmed that using lactic acid will increase the growth rate of  $\text{Cu}_2\text{O}$  shells.

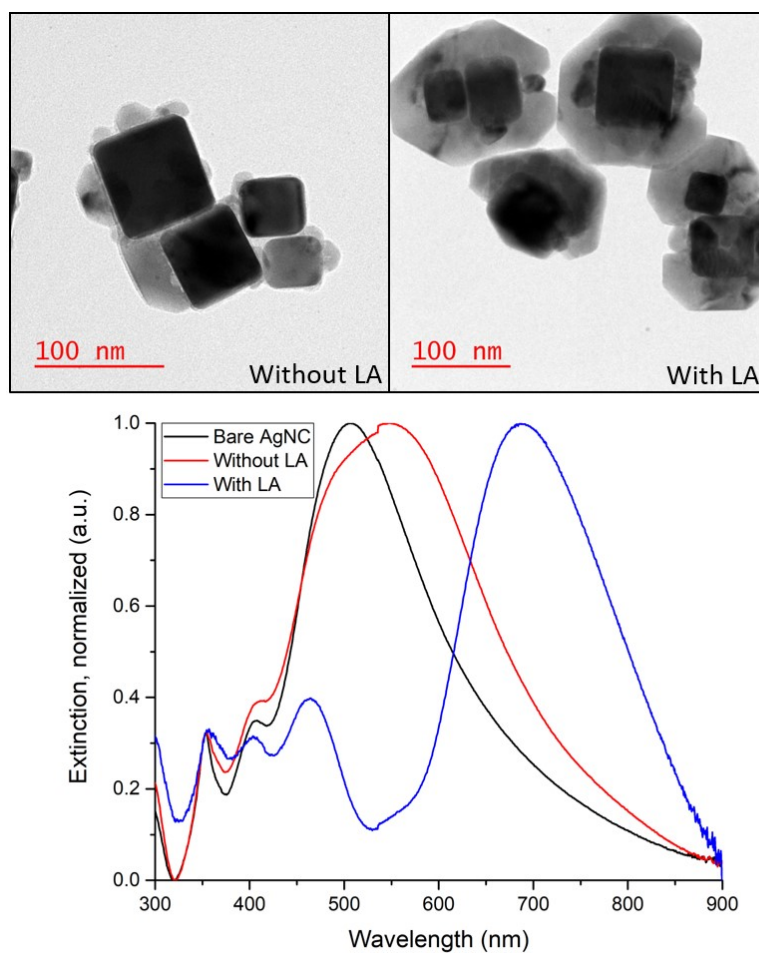


**Figure 3.42:** Above: TEM images of AgNC/Cu<sub>2</sub>O nanoparticles. Below: Extinction spectra of particles suspended in toluene.

### 3.5.5 Continuous hydrazine injection

| Section ID | Cu salt                           | Volume ( $\mu\text{L}$ ) or Concentration |     |     |                               | Order of addition                           | Injection method                         |
|------------|-----------------------------------|---|-----|-----|-------------------------------|---|--|
|            |                                   | NaOH                                      | LA  | Cu  | N <sub>2</sub> H <sub>4</sub> |   |  |
| 3.5.5.1    | Cu(NO <sub>3</sub> ) <sub>2</sub> | 450                                       | NA  | 450 | 0.55%                         | NaOH, Cu, N <sub>2</sub> H <sub>4</sub>     | Continuous N <sub>2</sub> H <sub>4</sub> |
|            | Cu(NO <sub>3</sub> ) <sub>2</sub> | 550                                       | NA  | 550 | 0.55%                         | NaOH, Cu, N <sub>2</sub> H <sub>4</sub>     |  |
|            | Cu(NO <sub>3</sub> ) <sub>2</sub> | 650                                       | NA  | 650 | 0.55%                         | NaOH, Cu, N <sub>2</sub> H <sub>4</sub>     |  |
|            | Cu(NO <sub>3</sub> ) <sub>2</sub> | 750                                       | NA  | 750 | 0.55%                         | NaOH, Cu, N <sub>2</sub> H <sub>4</sub>     |  |
| 3.5.5.2    | Cu(NO <sub>3</sub> ) <sub>2</sub> | 450                                       | 450 | 450 | 0.55%                         | NaOH, Cu, LA, N <sub>2</sub> H <sub>4</sub> | Continuous N <sub>2</sub> H <sub>4</sub> |
|            | Cu(NO <sub>3</sub> ) <sub>2</sub> | 450                                       | NA  | 450 | 0.55%                         | NaOH, Cu, N <sub>2</sub> H <sub>4</sub>     |  |
|            | Cu(NO <sub>3</sub> ) <sub>2</sub> | 650                                       | 650 | 650 | 0.55%                         | NaOH, Cu, LA, N <sub>2</sub> H <sub>4</sub> |  |
|            | Cu(NO <sub>3</sub> ) <sub>2</sub> | 650                                       | NA  | 650 | 0.55%                         | NaOH, Cu, N <sub>2</sub> H <sub>4</sub>     |  |

The purpose of the following series of experiments was to elucidate the reasoning for varied shell morphology.

### 3.5.5.1 Without lactic acid

Continuous injection of hydrazine without the use of lactic acid resulted in a cubic shell morphology, whereas continuous copper nitrate injection gave pyramidal shells. The tested volumes of 5M NaOH and 0.5M Cu(NO<sub>3</sub>)<sub>2</sub> were 450, 550, 650, 750  $\mu$ L. Ten millilitres of 0.55% N<sub>2</sub>H<sub>4</sub> aqueous solution were injected at a rate of 0.2mL/min. EDS measurements showed an average Cu:O ratio of 2.1:1 indicating that the shell is composed of Cu<sub>2</sub>O. The 450 $\mu$ L trial resulted in cubic-like growth, apparent at the AgNC corners as seen in the TEM images (Figure 3.43 A). The coverage was incomplete and the overall thickness was  $10.6 \pm 4.0$  nm (59 measurements). When 550 $\mu$ L of the reagents were added, the growth was nearly complete cubic half-shells (Figure 3.43 B). These shells were still primarily polycrystalline, with clear boundaries observed between Cu<sub>2</sub>O shell segments, indicating the final growth step of crystal reconstruction was incomplete. The mean shell thickness was  $18.0 \pm 4.1$  nm (34 measurements). As for the 650 $\mu$ L trial, cubic shells are once again observed (Figure 3.43 C). Polycrystallinity was still seen, although to a lesser extent than the 550 $\mu$ L trial. The average shell thickness was  $18.2 \pm 4.5$  nm (34 measurements). For the final trial, 750 $\mu$ L of reagents were added. The resultant shell had cubic (Figure 3.43 D-1) and amorphous (Figure 3.43 D-2) morphologies with the mean shell thickness being  $20.2 \pm 9.2$  nm (74 measurements). The amorphous morphology may be due to spontaneous growth on the polystyrene stemming from high NaOH and Cu(NO<sub>3</sub>)<sub>2</sub> volumes.

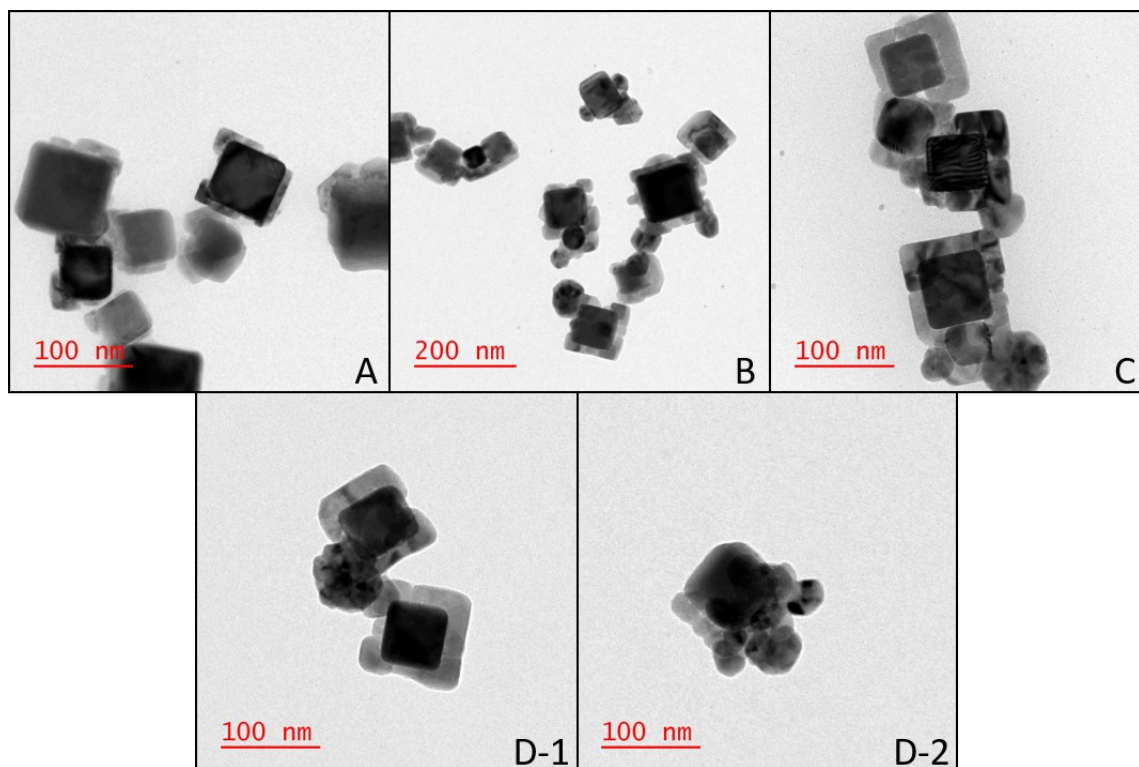


**Figure 3.43:** TEM images of AgNC/Cu<sub>2</sub>O particles for the following volumes of each 5M NaOH and 0.5M Cu(NO<sub>3</sub>)<sub>2</sub> (A) 450μL; (B) 550μL; (C) 650μL; (D) 750μL. (D-1) Cubic morphology; (D-2) Amorphous morphology.

For both the embedded and suspended particles, the extinction spectra (Figure 3.44) have a similar progression of peak shift and peak development as compared to the continuous addition of Cu(NO<sub>3</sub>)<sub>2</sub> with the use of lactic acid (Figure 3.37, Figure 3.38). While the shell thickness does not increase significantly beyond the 550μL trial, the extinction spectra display continued progression of dipole red shift and peak development. This is potentially due to the reduction in polycrystallinity as the reagent volumes are increased.

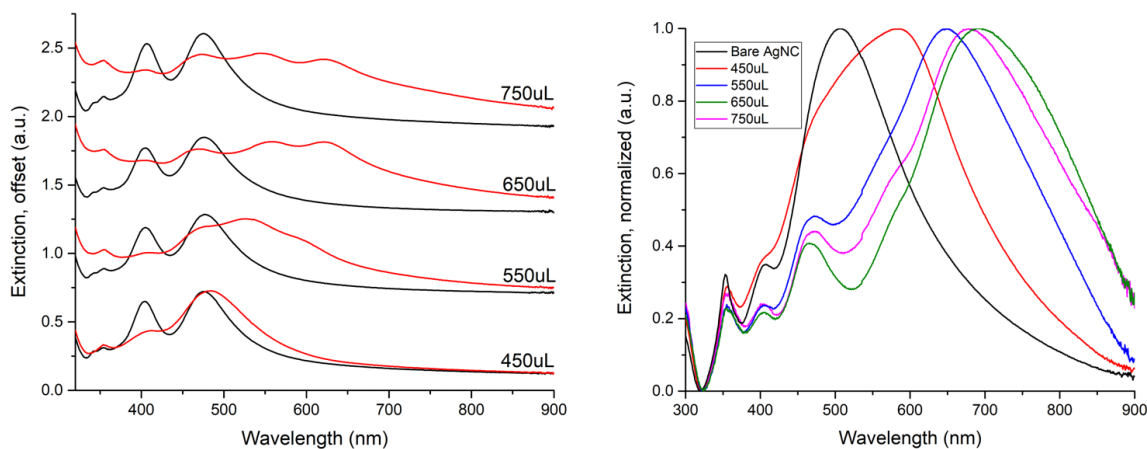


**Figure 3.44:** Left: Extinction spectra of  $\text{Cu}_2\text{O}$  reaction with slow addition of hydrazine without lactic acid, before reaction (black) and after reaction (red). Right: Extinction spectra of particles suspended in toluene. Volume in legend indicates the amount of 5M NaOH and 0.5M  $\text{Cu}(\text{NO}_3)_2$  added.

### 3.5.5.2 With lactic acid

Some of the above tests were replicated with the use of lactic acid to determine if it affects the morphology of the shell when hydrazine is added continuously.

As was shown in section 3.5.4, there is increased growth progression with the presence of lactic acid. This stands true with continuous hydrazine addition and is evident in the extinction spectra of embedded (Figure 3.45) and suspended (Figure 3.46) AgNC/ $\text{Cu}_2\text{O}$  nanoparticles. Dual tests were performed with different parameters: the first being 450 $\mu\text{L}$  of each 5M NaOH, 4M lactic acid, 0.5M  $\text{Cu}(\text{NO}_3)_2$ , and the second being 650 $\mu\text{L}$  of each 5M NaOH, 4M lactic acid, 0.5M  $\text{Cu}(\text{NO}_3)_2$ . Both had the 10mL injection of 0.55%  $\text{N}_2\text{H}_4$  at 0.2mL/min. We still see the progression of growth with increase in reagent volume; and growth is stunted when lactic acid is not used.

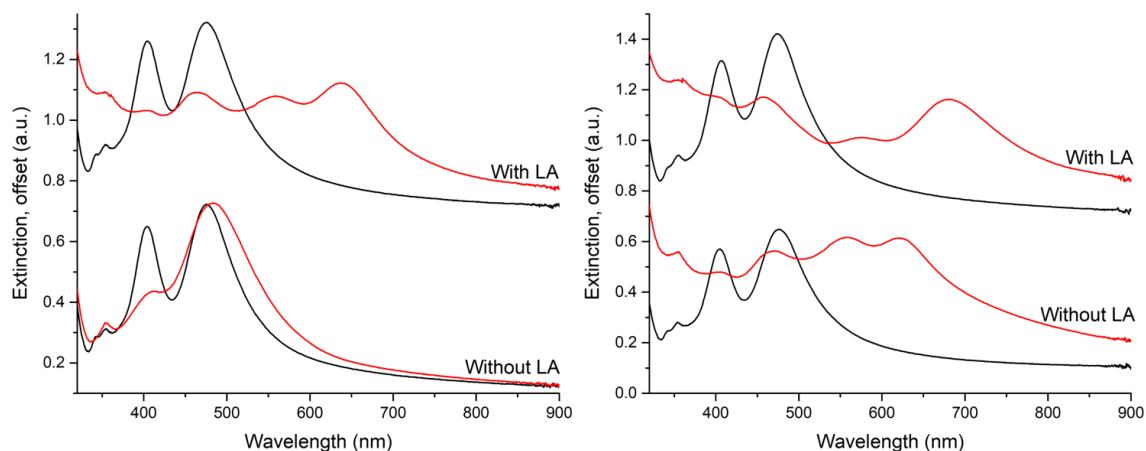


**Figure 3.45:** Extinction spectra of embedded AgNC/Cu<sub>2</sub>O particles synthesized with the following volumes of each 5M NaOH, 4M LA, and 0.5M Cu(NO<sub>3</sub>)<sub>2</sub> (left) 450μL; (right) 650μL.

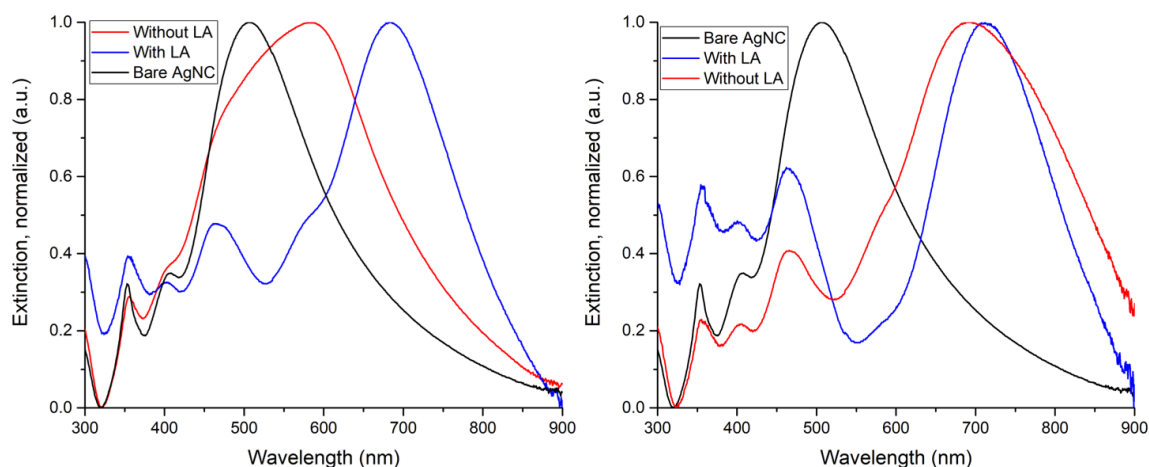


**Figure 3.46:** Extinction spectra of suspended AgNC/Cu<sub>2</sub>O particles synthesized with the following volumes of each 5M NaOH, 4M LA, and 0.5M Cu(NO<sub>3</sub>)<sub>2</sub> (left) 450μL; (right) 650μL.

The increase in shell growth is also evident from the TEM images acquired (Figure 3.47) wherein the 450μL and 650μL trials had average shell thicknesses of  $21.3 \pm 8.3$  nm (58 measurements) and  $29.2 \pm 8.3$  nm (92 measurements), respectively. It was determined from EDS that the Cu:O ratio was 1.4:1, potentially indicating that the shell was comprised of CuO. However, this measurement technique is not conclusive and X-ray diffraction (XRD) is required for reliable compositional analysis. What is most striking about these

samples is that the shell has a mix of cubic and pyramidal morphologies within the same particle. The cubic shells are classified by those that have outer boundaries that run parallel to the cube core edge. The pyramidal shells are those where the outer boundaries of the Cu<sub>2</sub>O are offset by 45 degrees to the cube core edge.

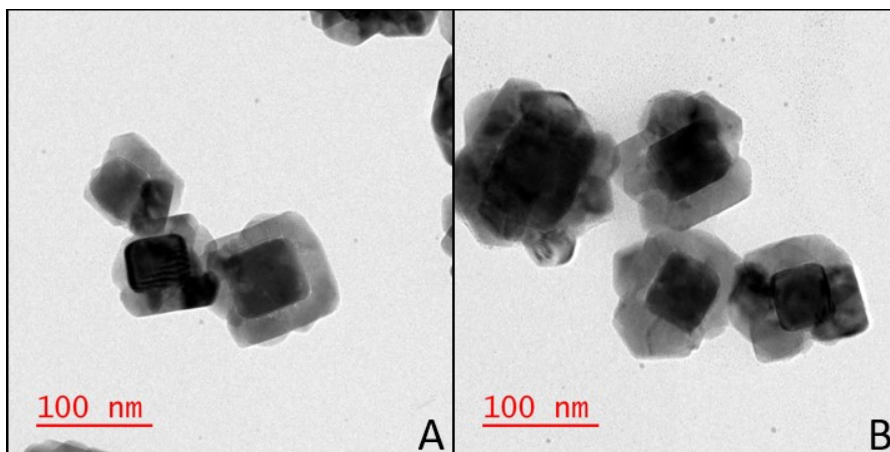


**Figure 3.47:** TEM images of AgNC/Cu<sub>2</sub>O particles synthesized with the following volumes of each 5M NaOH, 4M LA, and 0.5M Cu(NO<sub>3</sub>)<sub>2</sub> (A) 450μL; (B) 650μL.

Since it was elucidated from previous tests that lactic acid increases the kinetics of the synthesis, it can be presumed that a pyramidal morphology is likely to appear when the rate of growth increases.

### 3.5.6 Copper sulphate as precursor

Before witnessing the effects of continuous hydrazine injection, it was believed that a different copper precursor would provide the cubic shell morphology based on the work by Huang et al.<sup>103</sup> Multiple procedural modifications were made to the following series of trials and will be detailed individually.

| Section ID | Cu salt           | Volume (μL) or Concentration |     |        |                               |      | Order of addition                            | Injection method                         |
|------------|-------------------|------------------------------|-----|--------|-------------------------------|------|--|--|
|            |                   | NaOH                         | LA  | Cu     | N <sub>2</sub> H <sub>4</sub> | AA   |  |  |
| 3.5.6      | CuSO <sub>4</sub> | 650                          | 650 | 32.5mM | 220                           | NA   | NaOH, LA, N <sub>2</sub> H <sub>4</sub> , Cu | Continuous Cu                            |
|            | CuSO <sub>4</sub> | 650                          | 650 | 650    | 220                           | NA   | Cu, NaOH, LA, N <sub>2</sub> H <sub>4</sub>  | All fast addition                        |
|            | CuSO <sub>4</sub> | 650                          | NA  | 650    | NA                            | 1000 | Cu, NaOH, AA                                 |  |
|            | CuSO <sub>4</sub> | 650                          | 650 | 650    | NA                            | 1000 | Cu, NaOH, LA, AA                             |  |
|            | CuSO <sub>4</sub> | 650                          | 650 | 650    | 0.55%                         | NA   | NaOH, Cu, LA, N <sub>2</sub> H <sub>4</sub>  | Continuous N <sub>2</sub> H <sub>4</sub> |

**CuSO<sub>4</sub> reduced with ascorbic acid, without lactic acid:**

In this sample, CuSO<sub>4</sub> was reduced with ascorbic acid instead of hydrazine. The order of addition was copper sulfate, sodium hydroxide, and then ascorbic acid. All were quick, individual injections. In the extinction spectrum of the embedded particles (Figure 3.48 A), there was a slight blue shift of the dipolar and quadrupolar modes, and in the in-solution spectrum of the particles (Figure 3.49 A), there is a slight red shift of the dipolar mode. From the TEM images (Figure 3.49 A), we can observe minimal amorphous growth on the AgNC which explains the lack of change in the extinction. Therefore, ascorbic acid alone was not sufficient for the formation of shells.

**CuSO<sub>4</sub> reduced with ascorbic acid, with lactic acid:**

In this synthesis, the order of addition was copper sulfate, sodium hydroxide, lactic acid, and then ascorbic acid. All were quick, individual injections. A typical synthesis with copper nitrate had a colour progression from blue or yellow to an opaque orange from the formation of cuprous oxide nanoparticles in solution. Throughout this experiment, the solution colour did not deviate from pale, transparent blue. However, the colour of the slide changed from a transparent light brown to an opaque pink-orange. This potentially indicates that copper oxide particles did not form in solution and all the copper precursor was instead directly reduced onto the silver nanocubes. The extinction spectrum of embedded particles (Figure 3.48 B) has very high extinction across all measured wavelengths and the in-solution spectrum (Figure 3.49 B) had the appearance of an abnormal peak at 590 nm and there is significant tailing from 600-900 nm. TEM images were acquired for this sample and are shown in Figure 3.49 B. The energy-dispersive x-

ray spectroscopy (EDS) measurements indicated a negligible amount of oxygen in comparison to copper in atomic percent (30:1). Therefore, it is postulated that the reduction of copper went further than desired, forming predominantly Cu metal and not copper oxide. The geometry of this shell varied from particle to particle with some having a cuboctahedron shape and others having random morphology or left completely bare. The mean shell thickness is 47.4 nm with a standard deviation of 20.8 nm (49 measurements), this mean excludes the particles that did not have a shell.

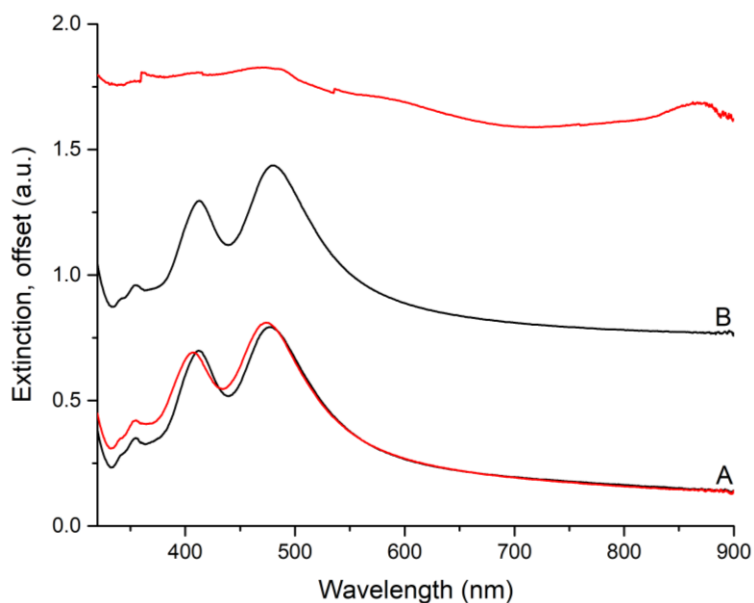


**Figure 3.48:** Extinction spectra of embedded AgNC before (black) and after (red) reaction. Synthesis used ascorbic acid as reducing agent. (A) Without lactic acid; (B) With lactic acid.

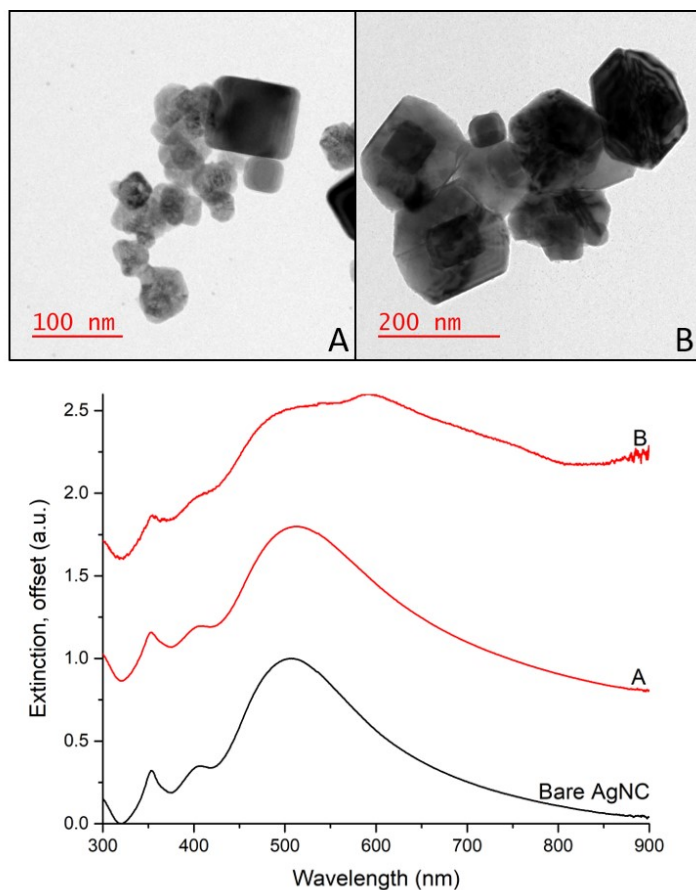


**Figure 3.49:** Above: TEM images of AgNC/Cu<sub>2</sub>O nanoparticles. Below: Extinction spectra of particles suspended in toluene. Black curve indicates bare AgNC, red curves indicate AgNC/Cu<sub>2</sub>O nanoparticles. Synthesis used ascorbic acid as reducing agent. (A) Without lactic acid; (B) With lactic acid.

#### **CuSO<sub>4</sub> added last, continuously, reduced with hydrazine:**

In this sample, the order of addition was sodium hydroxide, lactic acid, hydrazine, and then copper sulfate. The copper sulfate was added with continuous injection at a rate of 0.2mL/min. There was no significant colour change in the solution which could have been an indication that the copper sulfate was not sufficiently reduced to form copper oxide. The extinction spectrum (Figure 3.50 A) of this sample shows a slight blue shift of both the quadrupolar and dipolar modes meaning that there was very little to no shell growth on the AgNCs.

**CuSO<sub>4</sub> added first, reduced with hydrazine:**

In this synthesis, the order of addition is as such: copper sulfate, sodium hydroxide, lactic acid, and hydrazine. All were quick, individual injections. The extinction spectrum of the embedded particles (Figure 3.50 B) shows a slight red shift of the dipolar mode and a depletion of the quadrupolar mode. The extinction spectrum of the particles suspended in toluene (Figure 3.51 A) shows a red shift of the dipolar mode and the development of a quadrupolar mode, therefore indicating a small amount of shell growth. The TEM images (Figure 3.51 A) show a small amount of nucleation on the AgNC but primary growth was in solution and formed rough and polycrystalline spheres of copper oxide. The average thickness of growth on the AgNCs was  $11.2 \pm 3.3$  nm (51 measurements) with approximate Cu:O of 1.3:1.

**CuSO<sub>4</sub> reduced with continuous hydrazine, with LA:**

The order of addition for this synthesis was sodium hydroxide, copper sulfate, lactic acid, and then hydrazine. The hydrazine was added with continuous injection at a rate of 0.2mL/min. For both the embedded and suspended particles, the extinction spectra (Figure 3.50C, Figure 3.51B) have a similar progression of peak shift and peak development as compared to the continuous addition of Cu(NO<sub>3</sub>)<sub>2</sub> (Figure 3.37, Figure 3.38). The TEM images acquired show a mix of pyramidal and cubic shell growth (Figure 3.51B).

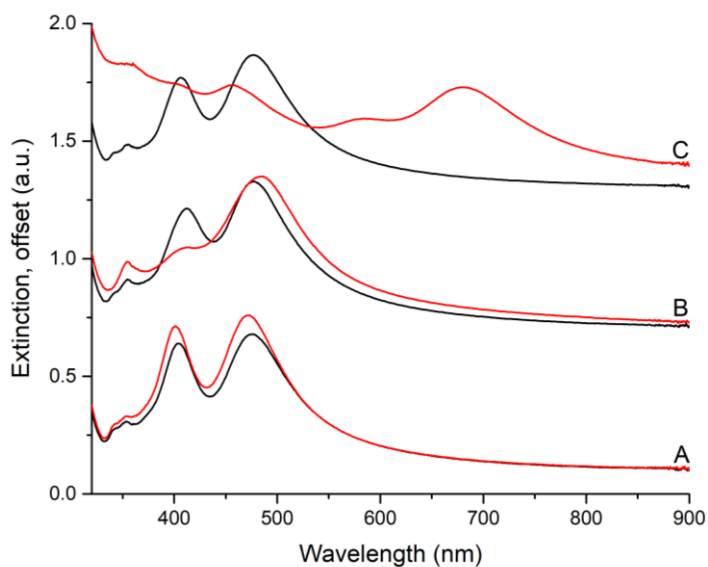


**Figure 3.50:** Extinction spectra of embedded AgNC before (black) and after (red) reaction. Synthesis used hydrazine as reducing agent. (A)  $\text{CuSO}_4$  added last, continuously; (B)  $\text{CuSO}_4$  added first, quickly; (C) Hydrazine added last, continuously.

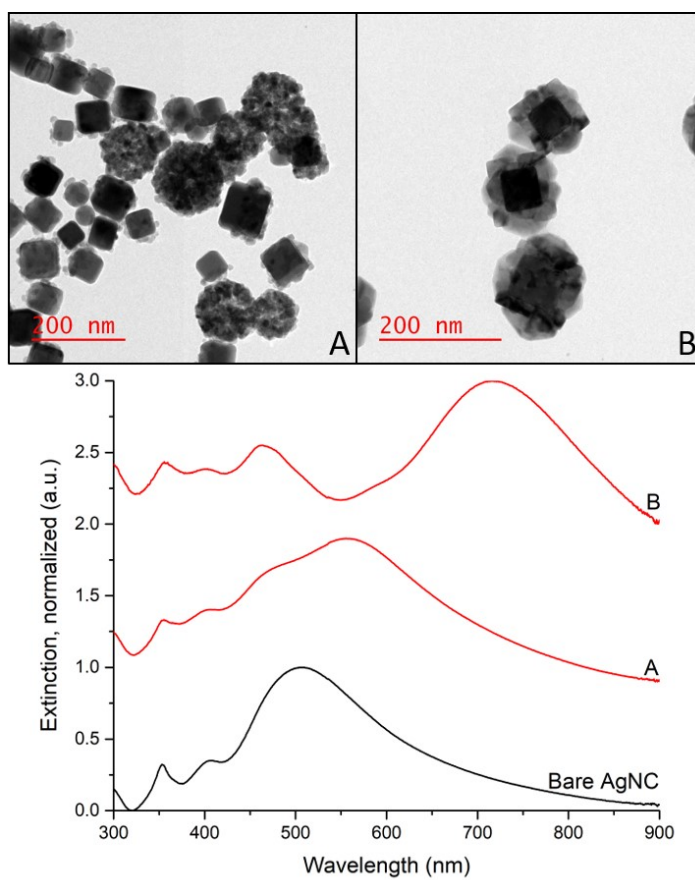


**Figure 3.51:** Above: TEM images of AgNC/ $\text{Cu}_2\text{O}$  nanoparticles. Below: Extinction spectra of particles suspended in toluene. Black curve indicates bare AgNC, red curves indicate AgNC/ $\text{Cu}_2\text{O}$  nanoparticles. (A) Reduced with hydrazine,  $\text{CuSO}_4$  added first; (B) Reduced with hydrazine, added slowly, with lactic acid.

### 3.5.7 Effect of cube coverage on optical properties

| Section ID | Cu salt                    | Volume ( $\mu\text{L}$ ) or Concentration |     |        |                        | Order of addition                     | Injection method |
|------------|----------------------------|---|-----|--------|------------------------|---------------------------------------|------------------|
|            |                            | NaOH                                      | LA  | Cu     | $\text{N}_2\text{H}_4$ |                                       |                  |
| 3.5.7      | $\text{Cu}(\text{NO}_3)_2$ | 450                                       | 450 | 22.5mM | 220                    | NaOH, LA, $\text{N}_2\text{H}_4$ , Cu | Continuous Cu    |
|            | $\text{Cu}(\text{NO}_3)_2$ | 450                                       | 450 | 22.5mM | 220                    | NaOH, LA, $\text{N}_2\text{H}_4$ , Cu |                  |
|            | $\text{Cu}(\text{NO}_3)_2$ | 450                                       | 450 | 22.5mM | 220                    | NaOH, LA, $\text{N}_2\text{H}_4$ , Cu |                  |
|            | $\text{Cu}(\text{NO}_3)_2$ | 450                                       | 450 | 22.5mM | 220                    | NaOH, LA, $\text{N}_2\text{H}_4$ , Cu |                  |
|            | $\text{Cu}(\text{NO}_3)_2$ | 650                                       | 650 | 32.5mM | 220                    | NaOH, LA, $\text{N}_2\text{H}_4$ , Cu |                  |
|            | $\text{Cu}(\text{NO}_3)_2$ | 650                                       | 650 | 32.5mM | 220                    | NaOH, LA, $\text{N}_2\text{H}_4$ , Cu |                  |
|            | $\text{Cu}(\text{NO}_3)_2$ | 650                                       | 650 | 32.5mM | 220                    | NaOH, LA, $\text{N}_2\text{H}_4$ , Cu |                  |

For the cube coverage tests, the AgNCs were embedded into the PS to varied depths. These trials had the aim of coating the top half, third, and quarter of the cubes in order to observe increased hybridization with decreased cube coverage. Essentially, the value of  $x$  in Figure 3.52 is what is being altered.

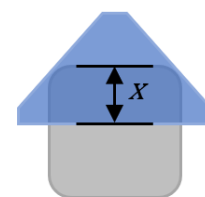
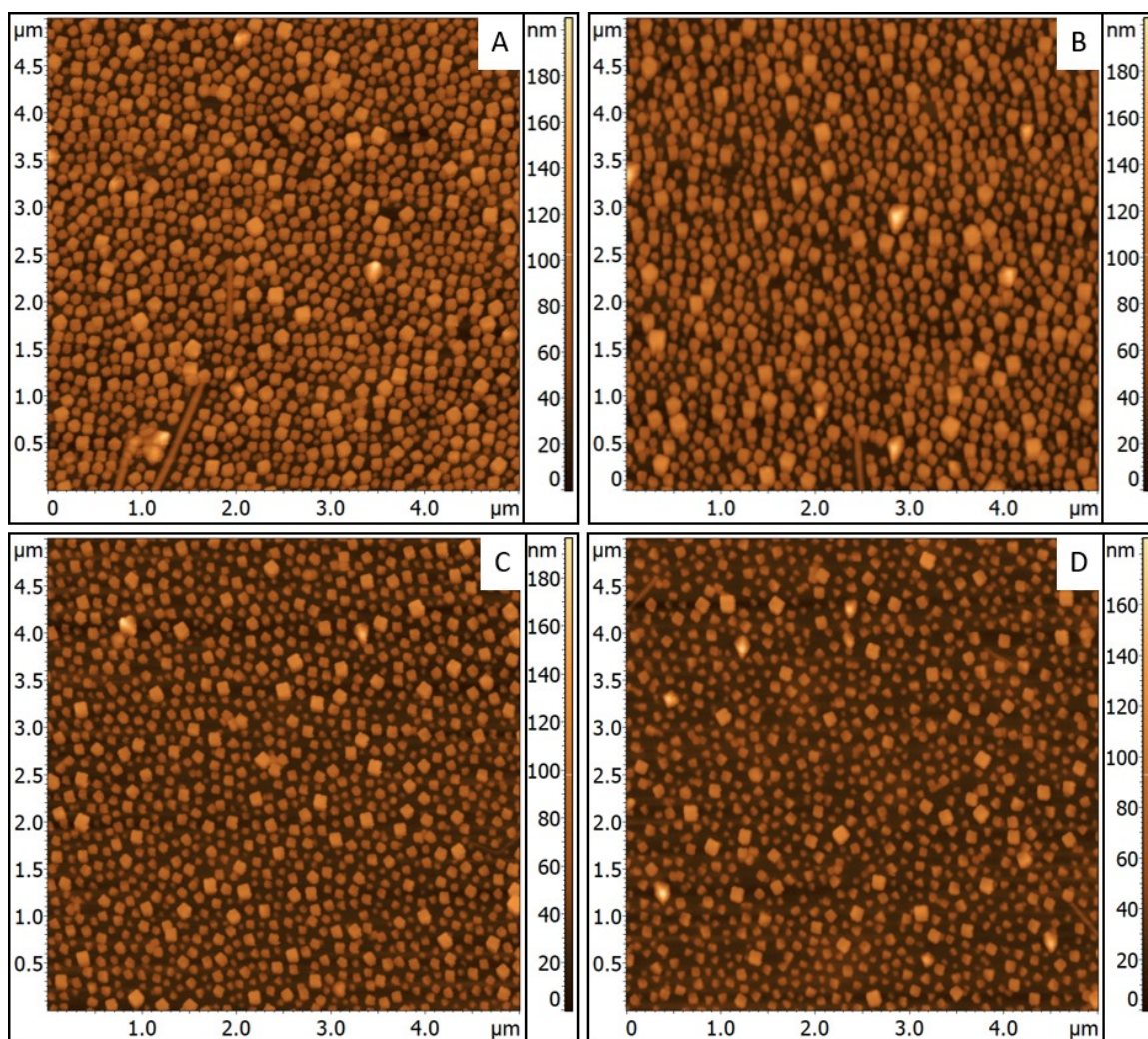


Figure 3.52: Illustration for experiment concept.

Dual tests were performed with different parameters: the first being 450 $\mu\text{L}$  of each 5M NaOH, 4M lactic acid, and 10mL of 22.5mM  $\text{Cu}(\text{NO}_3)_2$ , and the second being 650 $\mu\text{L}$  of each 5M NaOH, 4M lactic acid, and 10mL of 32.5mM  $\text{Cu}(\text{NO}_3)_2$ . Both had 220 $\mu\text{L}$  of 25% hydrazine. Each of the above will be shorthanded to the “450 $\mu\text{L}$ ” and “650 $\mu\text{L}$ ” trials. The least embedded AgNCs had  $46.1 \pm 3.4$  nm (4 measurements) exposed. The low-mid embedded AgNCs had either  $34.8 \pm 1.9$  nm (4 measurements) or  $32.7 \pm 2.8$  nm (4 measurements) exposed, dependant on the trial. The high-mid embedded AgNCs had  $29.5 \pm 3.8$  nm (4 measurements) exposed. The most embedded AgNCs had  $24.2 \pm 2.0$  nm exposed (4 measurements). Through the embedding process, until reaching half-way embedding, the AgNCs remain vertical (Figure 3.53 A, B). When the cube approaches half-way embedding, some cubes begin to tilt (Figure 3.53 C) and as it continues to embed most cubes are tilted on one corner (Figure 3.53 D).



**Figure 3.53:** AFM images of bare AgNCs embedded in PS. The amount of AgNC exposed is (A) 46 nm; (B) 33 nm; (C) 30 nm; (D) 24 nm.

For the 450 $\mu$ L trials, from the extinction spectra of the embedded particles (Figure 3.54), it is observed that the more the nanocubes are embedded, the less the effect of the Cu<sub>2</sub>O shell on the particles' extinction due to less of the particle being surrounded by this high refractive index substance. This trend partially stands for the 650 $\mu$ L trials wherein the two most embedded samples show less change and the two least embedded show more change, however within the four there is alternating higher and lower growth (Figure 3.55).

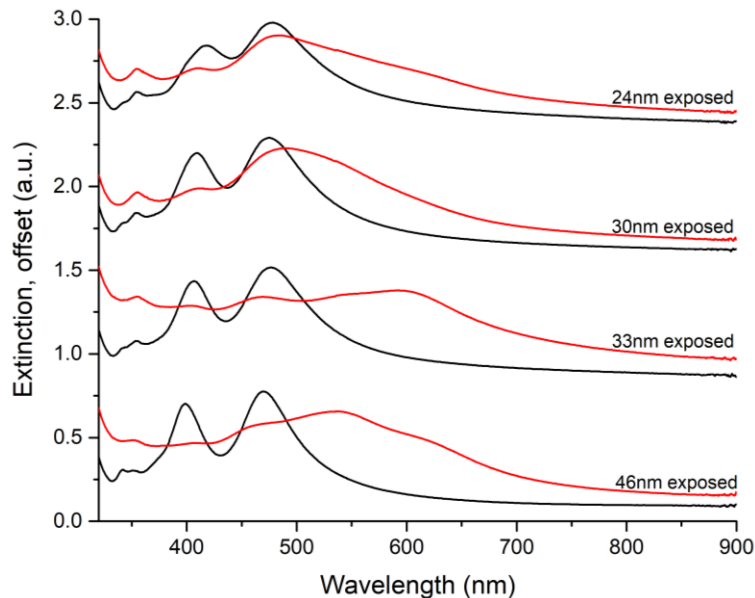


**Figure 3.54:** Extinction spectra of embedded particles for the 450uL trials before (black) and after (red)  $\text{Cu}_2\text{O}$  reaction.

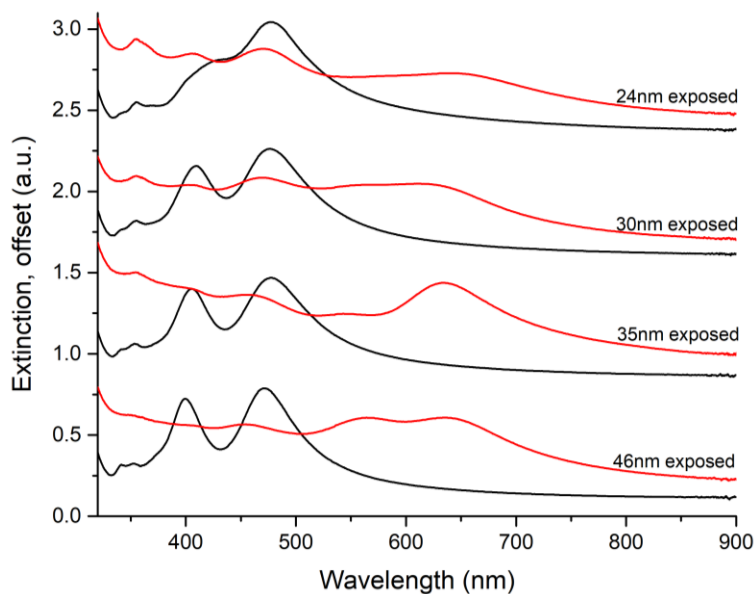


**Figure 3.55:** Extinction spectra of embedded particles for the 650uL trials before (black) and after (red)  $\text{Cu}_2\text{O}$  reaction.

For the 450 $\mu\text{L}$  trial, the resultant shells grown from the least to most embedded are:  $28.2 \pm 9.0$  nm (128 measurements),  $35.3 \pm 11.3$  nm (96 measurements),  $28.7 \pm 8.7$  nm (83 measurements),  $31.4 \pm 10.6$  nm (97 measurements). Since these values do not extend beyond the associated errors, it can be said that the shell thickness does not significantly deviate with change of embedment depth. For the least embedded samples, the

polycrystallinity is much higher than for the mid-way and most embedded particles. For all samples, a mix of morphologies and orientations are seen. The least embedded particles have rectangular growths growing orthogonally to the cube core corners and multiple  $\text{Cu}_2\text{O}$  nanocrystals on the edges and faces of the AgNC (Figure 3.56 A). The mid-way and most embedded particles have a significant amount of complete half-shells many of which are pyramidal and some of which are rectangular. These two shapes are due to the orientation of the embedded cube. If the AgNC embeds vertically without any tilting, the resultant shell is pyramidal (Figure 3.56 B). If the AgNC is tilted in the PS then the shell produced is rectangular (Figure 3.56 C). Both are growing along the same crystal facets; however, it is the polystyrene that blocks the  $\text{Cu}_2\text{O}$  from reaching the rest of the cube. EDS for the 450 $\mu\text{L}$  and 650 $\mu\text{L}$  trials result in 1.9:1 Cu:O, indicating  $\text{Cu}_2\text{O}$  composition.

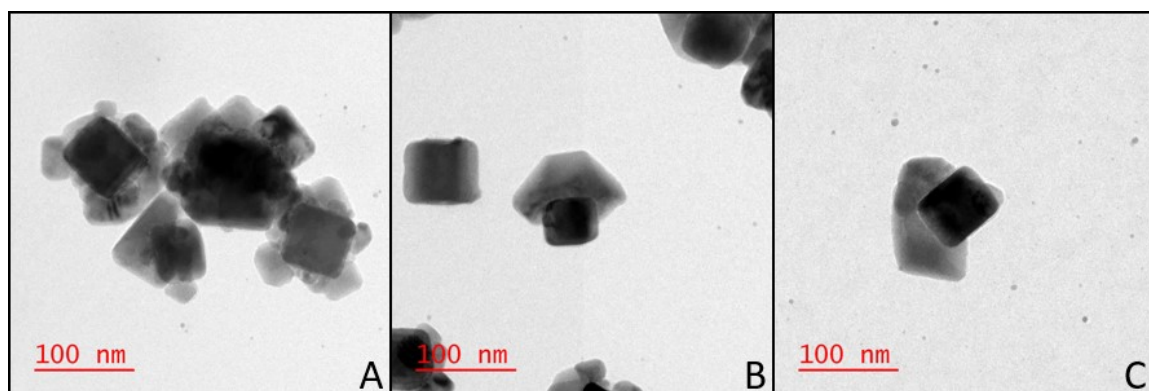


**Figure 3.56:** TEM images of AgNC/ $\text{Cu}_2\text{O}$  particles for (A) least embedded, (B) mid-way embedded, (C) most embedded particles from the 450 $\mu\text{L}$  trials.

From the extinction spectra of the particles suspended in toluene (Figure 3.57), we are able to quantify the extent of the quadrupolar ( $\sim 475\text{nm}$ ) and dipolar ( $\sim 650\text{nm}$ ) peak splitting. This was then compared to the shell thickness in relation to the amount of AgNC exposed. From the plot in Figure 3.58, it can be observed that there is no discernable shared trend for the shell thickness and peak splitting.

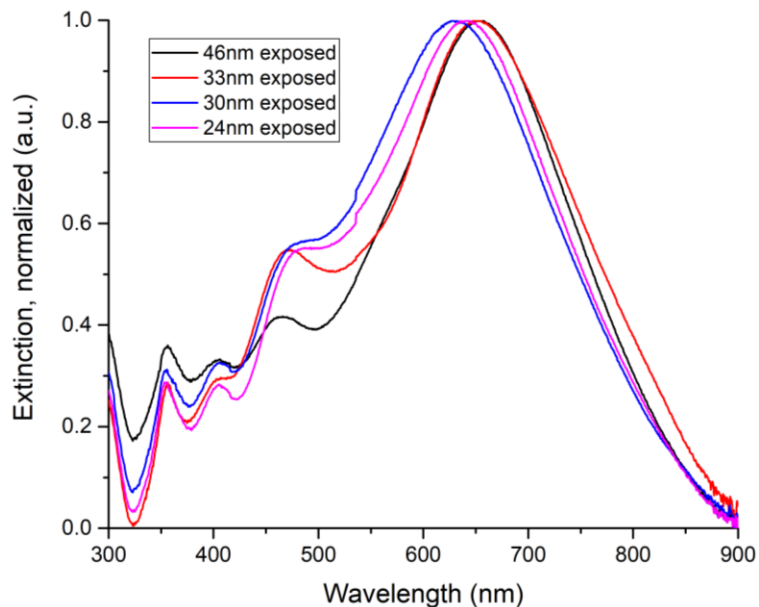


**Figure 3.57:** Extinction spectra of 450uL, 22.5mM trials removed from slide, in toluene.

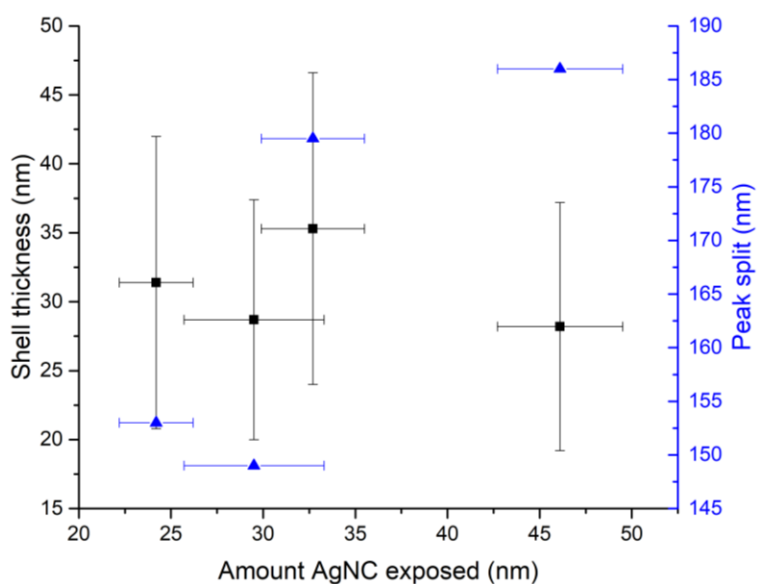


**Figure 3.58:** Relationship of shell growth and peak splitting with amount of AgNC exposed, 450uL trial.

For the 650 $\mu$ L trial, the resultant shells grown from the least to most embedded are:  $31.3 \pm 9.3$  nm (187 measurements),  $32.4 \pm 8.4$  nm (270 measurements),  $35.8 \pm 8.6$  nm (82 measurements),  $38.2 \pm 11.3$  nm (101 measurements). While the values appear to increase with depth of embedding, they do not extend beyond the associated errors. Therefore, as with the 450 $\mu$ L trial, the shell thickness does not significantly deviate with change of

embedding depth. The differences in shell morphology are similar to those for the 450 $\mu$ L trial however there are some differences. The least embedded particles (Figure 3.59 A) have lower polycrystallinity, that is fewer crystal boundaries, and more complete shells than the equivalent sample in the 450 $\mu$ L trials. For the mid-way and most embedded particles (Figure 3.59 B, C) also have the pyramidal and rectangular shells as seen above.

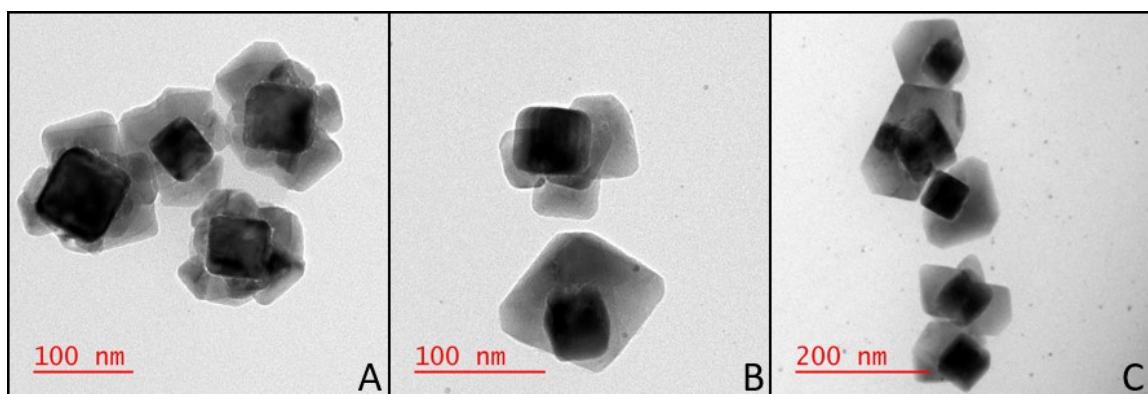


**Figure 3.59:** TEM images of AgNC/Cu<sub>2</sub>O particles for (A) least embedded, (B) mid-way embedded, (C) most embedded particles from the 650 $\mu$ L trials.

The extinction spectra of the suspended particles (Figure 3.60), exhibit greater peak splitting of the quadrupolar ( $\sim$ 475nm) and dipolar ( $\sim$ 700nm) peaks compared to the 450 $\mu$ L trials. This peak split was once again used for comparison with the shell thickness in relation to the amount of AgNC exposed. From the plot in Figure 3.61, we can see a slight increase in peak splitting as the shell thickness increases, however due to the large numerical errors this is not conclusive.

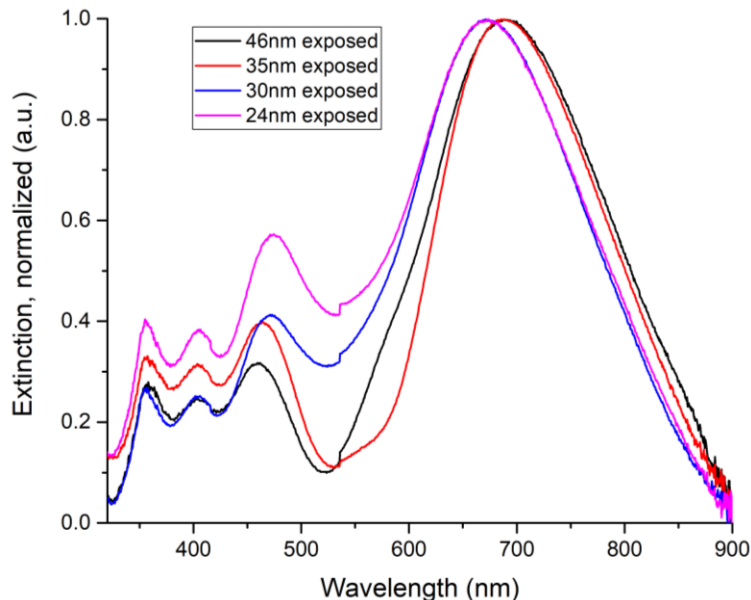


**Figure 3.60:** Extinction spectra of 650uL, 32.5mM trials removed from slide, in toluene.

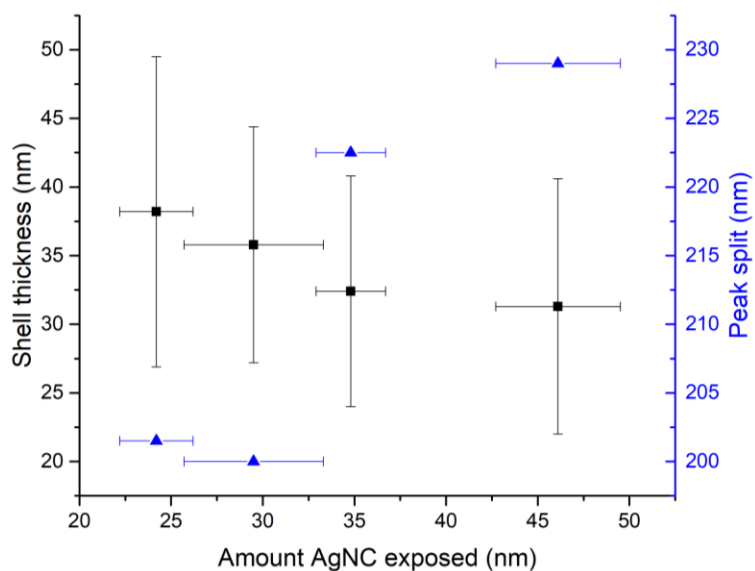


**Figure 3.61:** Relationship of shell growth and peak splitting with amount of AgNC exposed, 650uL trial.

Overall, this method of embedment limits a comprehensive study of the effects of AgNC coverage on its optical properties since the cube tilting is an uncontrolled variable. This research would be enhanced if another method of selectively blocking the nanocube core that can control the cube orientation was developed.

### 3.5.8 Cuprous oxide conclusions

The aim of producing AgNC/Cu<sub>2</sub>O core/half-shell nanoparticles was successful. Through FDTD simulations, we gained an insight into the theoretical effect of Cu<sub>2</sub>O half-shells on AgNC in varied scenarios: AgNC/Cu<sub>2</sub>O particles with a pyramidal shell in PS and suspended in solution; varied AgNC surface coverage by the shell; varied shell thicknesses for particles in PS and suspended in solution. Experimentally, the effect of reagent concentration found increased shell thickness with increasing reagent concentration. It was also determined that with thicker shells there is significant change in the optical properties of the particles and the thicker shells resulted in in-solution plasmon hybridization. For this method of slow Cu(NO<sub>3</sub>)<sub>2</sub> addition, the half-shell morphology was pyramidal. When the method of Cu(NO<sub>3</sub>)<sub>2</sub> addition was changed from stepwise addition to continuous injection, it was found that the continuous injection method yielded thicker and less polycrystalline shells with a maintained pyramidal morphology. When experiments were performed with and without lactic acid, it was determined that LA increases the kinetics of the reaction. Therefore, this resulted in a more complete progression of growth wherein the shells are thick and more monocrystalline. Following these experiments, continuous hydrazine injection was attempted instead of continuous Cu(NO<sub>3</sub>)<sub>2</sub> injection. This produced AgNC/Cu<sub>2</sub>O core/half-shell nanoparticles with a cubic half-shell morphology, meaning the order and method of reagent addition significantly impacts the final geometry. Additionally, the cubic shells had similar extinction spectra in comparison to the pyramidal shells. The effect of LA was the same as for slow copper injection (increased growth rate) but produced a mix of cubic and pyramidal shells. The reason for

this mix in morphology is yet to be fully elucidated but it is shown that the pyramidal morphology is favoured in when the growth rate is increased. As a secondary method for altering the morphology,  $\text{CuSO}_4$  was used as the precursor. The varied combinations of reducing agent, order of addition, and use of LA produced different outcomes. When ascorbic acid was used as the reducing agent without lactic acid, there was minimal amorphous growth on AgNC. Whereas when LA was used, thick copper shells were formed. When hydrazine was used as the reducing agent with LA and a slow addition of  $\text{CuSO}_4$ , no significant change was observed. However, when hydrazine was added slowly with LA, there was a mix of pyramidal and cubic shell growth as was observed with  $\text{Cu}(\text{NO}_3)_2$ . With hydrazine and all reagents added in single, quick injection, rough polycrystalline spheres were formed with minimal growth on AgNC. Finally, the investigation of the effect of cube coverage was incomplete. The method of embedment used in this work limited a comprehensive study of the effects of AgNC coverage on its optical properties since the cube tilting was an uncontrolled variable.

#### **4 Conclusion**

The objective of producing and investigating core/half-shell nanoparticles through the use of a polystyrene mask was achieved. While the gold and titania shell growths are incomplete at this time, silica and cuprous oxide provided positive results.

As it pertains to the attempted gold shell, two gold growth methods were attempted. For the first method, the presence of ascorbic acid and an alkaline solution should have provided adequate conditions for a decreased galvanic exchange rate and an increased reduction rate of  $\text{Au}^{1+}$  to  $\text{Au}^0$  onto the silver. While the galvanic exchange was successfully

suppressed, the deposition of gold onto silver was unconfirmed. For the second method, it was found that galvanic exchange primarily took place and so there was no core/half-shell particle formation. There is still potential for this method to provide gold deposition but would require increased suppression of galvanic exchange and further optimization of reagent concentrations. Additionally, the growth of Au on the PS mask means that another method of Au half-shell growth is required, one in which the growth is selective to the core.

For the titania growth, while well-defined shells were not formed, there was the formation of a titania film that coated multiple particles, making somewhat of a “micro-substrate”. The  $\text{TiO}_2$  that was produced was amorphous in structure and inducing crystallinity would have required temperatures that would have negatively affected the core. Due to the amorphous structure, the optical effects of the physical alterations were minimal. This could be beneficial for applications that seek to exploit the optical properties of the core.

The AgNC/ $\text{SiO}_2$  core/shell nanoparticles exhibited a complete and conformal coverage of  $\text{SiO}_2$ . This fully encapsulating shell was due to the undergrowth of silica between the AgNC and the polystyrene. While this was not the original desired outcome of this work, this does present an interesting method for reliable in-solution growth of thin, conformal silica shells. Additionally, it was found that spinning the sample slide resulted in loss of AgNCs, leaving behind their imprint and prompting an interesting approach to the formation of cavities of a defined shape. It was also determined that the amount of TEOS added to this system did not greatly impact the shell thickness therefore providing a

robust method for conformal SiO<sub>2</sub> shell growth. This method also proved to be scalable, making it attractive for functional uses.

The aim of producing AgNC/Cu<sub>2</sub>O core/half-shell nanoparticles was successful. The nanoparticles formed had a distinct half-shell morphology with either pyramidal or cubic half-shells where the geometry of the shell was dependent upon the order of reagent addition. Furthermore, the cuprous oxide half-shells caused significant modifications to the localized surface plasmon resonance of the AgNC core and resulted in in-solution hybridization of the plasmon modes. Through FDTD simulations, we gained an insight into the theoretical effect of Cu<sub>2</sub>O half-shells on AgNC in various scenarios. Experimentally, the effect of increased reagent concentrations yielded increased shell thicknesses. It was also determined that thicker shells demonstrated significant alterations to the optical properties of the particles. When the method of Cu(NO<sub>3</sub>)<sub>2</sub> addition was changed from stepwise addition to continuous injection, it was found that the continuous injection method yielded thicker and less polycrystalline shells. When experiments were performed with and without lactic acid, it was determined that LA increases the kinetics of the reaction and so results more a complete progression of growth wherein the shells are thick and more monocrystalline. Following this, slow hydrazine injection was attempted instead of slow Cu(NO<sub>3</sub>)<sub>2</sub> injection. While slow copper nitrate addition produced pyramidal shell morphologies, slow hydrazine injection resulted in cubic shells. Therefore, the order and method of reagent addition significantly impacts the final geometry. Some experimentation was also performed using copper sulfate as the precursor instead of copper nitrate and the varied combinations of reducing agent, order of addition, and use of LA produced a myriad

of outcomes, from no growth to copper shells to rough polycrystalline spheres. Finally, the investigation of the effect of cube coverage was deemed incomplete.

This partial shell growth technique is ideal for any low temperature, two step core/shell synthesis. The possible combinations of core and shell components can be tailored to satisfy a multitude of uses, some of which include SERS sensing, LSPR sensing, photocatalysis, and directed assembly. The present work should be further expanded to other cores and shells as well as employing these particles as functional materials for the applications listed above. For example, the AgNC/Cu<sub>2</sub>O nanoparticles could be used for the production of hydrogen from water splitting.

## 5 References

- (1) Howse, J. R.; Jones, R. A. L.; Ryan, A. J.; Gough, T.; Vafabakhsh, R.; Golestanian, R. *Phys. Rev. Lett.* **2007**, *99*, 048102.
- (2) McConnell, M. D.; Kraeutler, M. J.; Yang, S.; Composto, R. J. *Nano Lett.* **2010**, *10* (2), 603–609.
- (3) Glotzer, S. C.; Solomon, M. J. *Nat. Mater.* **2007**, *6* (8), 557–562.
- (4) Burrows, N. D.; Vartanian, A. M.; Abadeer, N. S.; Grzincic, E. M.; Jacob, L. M.; Lin, W.; Li, J.; Dennison, J. M.; Hinman, J. G.; Murphy, C. J. *J. Phys. Chem. Lett.* **2016**, *7* (4), 632–641.
- (5) Walther, A.; Müller, A. H. E. *Soft Matter* **2008**, *4* (4), 663–668.
- (6) Pawar, A. B.; Kretzschmar, I. *Macromol. Rapid Commun.* **2010**, *31* (2), 150–168.
- (7) Roh, K. H.; Martin, D. C.; Lahann, J. *J. Am. Chem. Soc.* **2006**, *128* (21), 6796–6797.
- (8) Casagrande, C.; Veyssie, M. *C. R. Acad. Sc. Paris* **1988**, *306*, 1423–1425.
- (9) Du, J.; O'Reilly, R. K. *Chem. Soc. Rev.* **2011**, *40*, 2402–2416.
- (10) Lattuada, M.; Hatton, T. A. *Nano Today* **2011**, *6* (3), 286–308.
- (11) Yoshida, M.; Roh, K. H.; Lahann, J. *Biomaterials* **2007**, *28* (15), 2446–2456.
- (12) Serra, C. A.; Chang, Z. *Chem. Eng. Technol.* **2008**, *31* (8), 1099–1115.
- (13) Nie, Z.; Li, W.; Seo, M.; Xu, S.; Kumacheva, E. *J. Am. Chem. Soc.* **2006**, *128* (29), 9408–9412.
- (14) Snyder, C. E.; Yake, A. M.; Feick, J. D.; Velegol, D. *Langmuir* **2005**, *21* (11), 4813–4815.
- (15) Pochan, D. J.; Zhu, J.; Zhang, K.; Wooley, K. L.; Miesch, C.; Emrick, T. *Soft Matter* **2011**, *7* (6), 2500–2506.
- (16) Xia, Y.; Gilroy, K. D.; Peng, H. C.; Xia, X. *Angew. Chemie - Int. Ed.* **2017**, *56* (1), 60–95.
- (17) Polte, J. *CrystEngComm* **2015**, *17* (36), 6809–6830.
- (18) Xia, Y.; Xiong, Y.; Lim, B.; Skrabalak, S. E. *Angew. Chemie - Int. Ed.* **2009**, *48* (1), 60–103.
- (19) Xiong, Y.; Xia, Y. *Adv. Mater.* **2007**, *19*, 3385–3391.
- (20) Martin, C. R. *Science (80-. )*. **1994**, *266* (5193), 1961–1966.
- (21) Kuijk, A.; Blaaderen, A. Van; Imhof, A. *J. Am. Chem. Soc.* **2011**, *133*, 2346–2349.
- (22) Choueiri, R. M.; Galati, E.; Klinkova, A.; Therien-Aubin, H.; Kumacheva, E. *Faraday Discuss.* **2016**, *191*, 189–204.
- (23) Pothorszky, S.; Zámbo, D.; Deák, A. *Part. Part. Syst. Charact.* **2017**, *34*, 1600291.
- (24) Miyanohta, R.; Matsushita, T.; Tsuruoka, T.; Nawafune, H.; Akamatsu, K. *J. Colloid Interface Sci.* **2014**, *416*, 147–150.
- (25) Chen, T.; Chen, G.; Xing, S.; Wu, T.; Chen, H. *Chem. Mater.* **2010**, *22*, 3826–3828.
- (26) Chen, T.; Yang, M.; Wang, X.; Tan, L. H.; Chen, H. *J. Am. Chem. Soc.* **2008**, *130*, 11858–11859.
- (27) Tan, L. H.; Xing, S.; Chen, T.; Chen, G.; Huang, X.; Zhang, H.; Chen, H. *ACS Nano* **2009**, *3* (11), 3469–3474.

- (28) Crane, C. C.; Tao, J.; Wang, F.; Zhu, Y.; Chen, J. *J. Phys. Chem. C* **2014**, *118*, 28134–28142.
- (29) Lu, X.; Rycenga, M.; Skrabalak, S. E.; Wiley, B.; Xia, Y. *Annu. Rev. Phys. Chem.* **2009**, *60*, 167–192.
- (30) Rycenga, M.; Cobley, C. M.; Zeng, J.; Li, W.; Moran, C. H.; Zhang, Q.; Qin, D.; Xia, Y. *Chem. Rev.* **2011**, *111*, 3669–3712.
- (31) Mulvaney, P. *Langmuir* **1996**, *12*, 788–800.
- (32) Willets, K. A.; Van Duyne, R. P. *Annu. Rev. Phys. Chem.* **2007**, *58*, 267–297.
- (33) Sherry, L. J.; Chang, S.-H.; Schatz, G. C.; Van Duyne, R. P.; Wiley, B. J.; Xia, Y. *Nano Lett.* **2005**, *5* (10), 2034–2038.
- (34) Knight, M. W.; Wu, Y.; Lassiter, J. B.; Nordlander, P.; Halas, N. J. *Nano Lett.* **2009**, *9* (5), 2188–2192.
- (35) Zhang, S.; Bao, K.; Halas, N. J.; Xu, H.; Nordlander, P. *Nano Lett.* **2011**, *11* (4), 1657–1663.
- (36) Ahamad, N.; Bottomley, A.; Ianoul, A. *J. Phys. Chem. C* **2012**, *116*, 185–192.
- (37) Bottomley, A.; Prezgot, D.; Coyle, J. P.; Ianoul, A. *Nanoscale* **2016**, *8* (21), 11168–11176.
- (38) Bushell, M.; Bottomley, A.; Ianoul, A. *Appl. Phys. A Mater. Sci. Process.* **2017**, *123* (2), 1–7.
- (39) Bushell, M.; Ianoul, A. *J. Phys. Chem. C* **2018**, *122* (18), 10197–10204.
- (40) Donth, E.-J. *The Glass Transition: Relaxation Dynamics in Liquids and Disordered Materials*, 1st ed.; Springer-Verlag Berlin Heidelberg, 2001; Vol. 48.
- (41) Rieger, J. *J. Therm. Anal.* **1996**, *46*, 965–972.
- (42) Kovacs, G. J.; Vincett, P. S. *J. Colloid Interface Sci.* **1982**, *90* (2), 335–351.
- (43) Brandrup, J.; Immergut, E. H.; Grulke, E. A. *Polymer Handbook*, 4th ed.; Wiley: New York, 1999.
- (44) Chaudhury, M. K. *Mater. Sci. Eng. R* **1996**, *16* (3), 97–159.
- (45) Chaudhuri, R. G.; Paria, S. *Chem. Rev.* **2012**, *112*, 2373–2433.
- (46) Gilroy, K. D.; Ruditskiy, A.; Peng, H.-C.; Qin, D.; Xia, Y. *Chem. Rev.* **2016**, [acs.chemrev.6b00211](https://doi.org/10.1021/acs.chemrev.6b00211).
- (47) Li, J.; Cushing, S. K.; Bright, J.; Meng, F.; Senty, T. R.; Zheng, P.; Bristow, A. D.; Wu, N. *ACS Catal.* **2013**, *3* (1), 47–51.
- (48) Burda, C.; Chen, X.; Narayanan, R.; El-sayed, M. A. *Chem. Rev.* **2005**, *105*, 1025–1102.
- (49) Das, A.; Zhao, J.; Schatz, G. C.; Sligar, S. G.; Duyne, R. P. Van. *Anal. Chem.* **2009**, *81*, 3754–3759.
- (50) Yang, L.; Wang, H.; Yan, B.; Reinhard, B. M. *J. Phys. Chem. C* **2010**, *114*, 4901–4908.
- (51) Moskovits, M. *J. Raman Spectrosc.* **2005**, *36*, 485–496.
- (52) Rycenga, M.; Camargo, P. H. C.; Li, W.; Moran, C. H.; Xia, Y. *J. Phys. Chem. Lett.* **2010**, *1*, 696–703.
- (53) Skrabalak, S. E.; Au, L.; Li, X.; Xia, Y. *Nat. Protoc.* **2007**, *2* (9), 2182–2190.
- (54) Skrabalak, S. E.; Wiley, B. J.; Kim, M.; Formo, E. V.; Xia, Y. *Nano Lett.* **2008**, *8*, 2077–2081.

- (55) Wiley, B.; Herricks, T.; Sun, Y.; Xia, Y. *Nano Lett.* **2004**, *4* (9), 1733–1739.
- (56) Sun, Y.; Mayers, B.; Herricks, T.; Xia, Y. *Nano Lett.* **2003**, *3* (7), 955–960.
- (57) Sun, Y.; Xia, Y. *Science (80-. )*. **2002**, *298*, 2176–2179.
- (58) Rycenga, M.; Xia, X.; Moran, C. H.; Zhou, F.; Qin, D.; Li, Z.; Xia, Y. *Angew. Chemie - Int. Ed.* **2011**, *50*, 5473–5477.
- (59) Yang, Y.; Liu, J.; Fu, Z. W.; Qin, D. *J. Am. Chem. Soc.* **2014**, *136* (23), 8153–8156.
- (60) Xia, X.; Wang, Y.; Ruditskiy, A.; Xia, Y. *Adv. Mater.* **2013**, *25*, 6313–6333.
- (61) Murshid, N.; Gourevich, I.; Coombs, N.; Kitaev, V. *Chem. Commun.* **2013**, *49*, 11355–11357.
- (62) Sanedrin, R. G.; Georganopoulou, Dimitra, G.; Park, S.; Mirkin, C. A. *Adv. Mater.* **2005**, *17* (8), 1027–1031.
- (63) Shahjamali, M. M.; Bosman, M.; Cao, S.; Huang, X.; Saadat, S.; Martinsson, E.; Aili, D.; Tay, Y. Y.; Liedberg, B.; Chye, S.; Loo, J.; Zhang, H.; Boey, F.; Xue, C. *Adv. Funct. Mater.* **2012**, *22*, 849–854.
- (64) Gao, C.; Lu, Z.; Liu, Y.; Zhang, Q.; Chi, M.; Cheng, Q.; Yin, Y. *Angew. Chemie - Int. Ed.* **2012**, *51*, 5629–5633.
- (65) Personick, M. L.; Mirkin, C. A. *J. Am. Chem. Soc.* **2013**, *135*, 18238–18247.
- (66) Luty-Błoch, M.; Paclawski, K.; Wojnicki, M.; Fitzner, K. *Inorganica Chim. Acta* **2013**, *395*, 189–196.
- (67) Du, J.; Cullen, J. J.; Buettner, G. R. *Biochim. Biophys. Acta* **2012**, *1826*, 443–457.
- (68) Sun, X.; Yang, Y.; Zhang, Z.; Qin, D. *Chem. Mater.* **2017**, *29*, 4014–4021.
- (69) Bourikas, K.; Kordulis, C.; Lycourghiotis, A. *Chem. Rev.* **2014**, *114*, 9754–9823.
- (70) Rehman, S.; Ullah, R.; Butt, A. M.; Gohar, N. D. *J. Hazard. Mater.* **2009**, *170*, 560–569.
- (71) Yang, L.; Jiang, X.; Ruan, W.; Yang, J.; Zhao, B.; Xu, W.; Lombardi, J. R. *J. Phys. Chem. C* **2009**, *113*, 16226–16231.
- (72) Xie, Y.; Jin, Y.; Zhou, Y.; Wang, Y. *Appl. Surf. Sci.* **2014**, *313*, 549–557.
- (73) Singh, L. P.; Bhattacharyya, S. K.; Kumar, R.; Mishra, G.; Sharma, U.; Singh, G.; Ahalawat, S. *Adv. Colloid Interface Sci.* **2014**, *214*, 17–37.
- (74) Livage, J.; Sanchez, C.; Henry, M.; Doeuff, S. *Solid State Ionics* **1989**, *32–33*, 633–638.
- (75) Jean, J. H.; Ring, T. A. *Langmuir* **1986**, *2*, 251–255.
- (76) Su, C.; Hong, B. Y.; Tseng, C. M. *Catal. Today* **2004**, *96*, 119–126.
- (77) Yin, H.; Wada, Y.; Kitamura, T.; Kambe, S.; Murasawa, S.; Mori, H.; Sakata, T.; Yanagida, S. *J. Mater. Chem.* **2001**, *11* (6), 1694–1703.
- (78) Shibata, H.; Ogura, T.; Mukai, T.; Ohkubo, T.; Sakai, H.; Abe, M. *J. Am. Chem. Soc.* **2005**, *127*, 16396–16397.
- (79) Horiguchi, Y.; Kanda, T.; Torigoe, K.; Sakai, H.; Abe, M. *Langmuir* **2014**, *30*, 922–928.
- (80) Sakai, H.; Kanda, T.; Shibata, H.; Ohkubo, T.; Abe, M. *J. Am. Chem. Soc.* **2006**, *128*, 4944–4945.
- (81) Graf, C.; Vossen, D. L. J.; Imhof, A.; van Blaaderen, A. *Langmuir* **2003**, *19* (17), 6693–6700.

- (82) Angkaew, S.; Limsuwan, P. *Procedia Eng.* **2012**, *32*, 649–655.
- (83) Kanda, T.; Komata, K.; Torigoe, K.; Endo, T.; Sakai, K.; Abe, M.; Sakai, H. *J. Oleo Sci.* **2014**, *63* (5), 507–513.
- (84) Giersig, M.; Ung, T.; Liz-Marzán, L. M. *Adv. Mater.* **1997**, *9* (7), 570–575.
- (85) Ung, T.; Liz-Marzán, L. M. *Langmuir* **1998**, *14* (10), 3740–3748.
- (86) Kobayashi, Y.; Katakami, H.; Mine, E.; Nagao, D.; Konno, M.; Liz-Marzán, L. M. *J. Colloid Interface Sci.* **2005**, *283* (2), 392–396.
- (87) Li, C.; Mei, J.; Li, S.; Lu, N.; Wang, L.; Chen, B.; Dong, W. *Nanotechnology* **2010**, *21*, 245602.
- (88) Liu, S.; Zhang, Z.; Han, M. *Anal. Chem.* **2005**, *77* (8), 2596.
- (89) Sun, J. Y.; Wang, Z. K.; Lim, H. S.; Ng, S. C.; Kuok, M. H.; Tran, T. T.; Lu, X. *ACS Nano* **2010**, *4* (12), 7692–7698.
- (90) Tay, L.; Hulse, J. *J. Mod. Opt.* **2013**, *60* (14), 1107–1114.
- (91) Stober, W.; Fink, A.; Bohn, E. *J. Colloid Interface Sci.* **1968**, *26*, 62–69.
- (92) Chou, K.-S.; Chen, C.-C. *Microporous Mesoporous Mater.* **2007**, *98*, 208–213.
- (93) Van Blaaderen, A.; Van Geest, J.; Vrij, A. *J. Colloid Interface Sci.* **1992**, *154* (2), 481–501.
- (94) Rahman, I. A.; Padavettan, V. *J. Nanomater.* **2012**, *2012*, 1–15.
- (95) Kuo, C.; Huang, M. H. *Nano Today* **2010**, *5* (2), 106–116.
- (96) Liu, C.; Chang, Y. H.; Chen, J.; Feng, S. P. *ACS Appl. Mater. Interfaces* **2017**, *9* (44), 39027–39033.
- (97) Cushing, S. K.; Li, J.; Meng, F.; Senty, T. R.; Suri, S.; Zhi, M.; Li, M.; Bristow, A. D.; Wu, N. *J. Am. Chem. Soc.* **2012**, *134* (36), 15033–15041.
- (98) Wang, Z.; Wang, H.; Wang, L.; Pan, L. *Cryst. Res. Technol.* **2009**, *44* (6), 624–628.
- (99) Sciacca, B.; Mann, S. A.; Tichelaar, F. D.; Zandbergen, H. W.; Van Huis, M. A.; Garnett, E. C. *Nano Lett.* **2014**, *14* (10), 5891–5898.
- (100) Jing, H.; Large, N.; Zhang, Q.; Wang, H. *J. Phys. Chem. C* **2014**, *118*, 19948–19963.
- (101) Kuo, C.-H.; Hua, T.-E.; Huang, M. H. *J. Am. Chem. Soc.* **2009**, *131* (49), 17871–17878.
- (102) Jimenez-Cadena, G.; Comini, E.; Ferroni, M.; Sberveglieri, G. *Mater. Lett.* **2010**, *64* (3), 469–471.
- (103) Ke, W. H.; Hsia, C. F.; Chen, Y. J.; Huang, M. H. *Small* **2016**, *12* (26), 3530–3534.
- (104) Bai, Y.; Yang, T.; Gu, Q.; Cheng, G.; Zheng, R. *Powder Technol.* **2012**, *227*, 35–42.
- (105) Andal, V.; Buvaneswari, G. *Eng. Sci. Technol. an Int. J.* **2017**, *20* (1), 340–344.
- (106) Ho, J.; Huang, M. H. *J. Phys. Chem.* **2009**, *113*, 14159–14164.
- (107) Kuo, C.; Huang, M. H. *J. Phys. Chem. C* **2008**, *112*, 18355–18360.
- (108) Sui, Y.; Fu, W.; Yang, H.; Zeng, Y.; Zhang, Y.; Zhao, Q.; Li, Y.; Zhou, X.; Leng, Y.; Li, M.; Zou, G. *Cryst. Growth Des.* **2010**, *10* (1), 99–108.
- (109) Bijani, S.; Schrebler, R.; Dalchiele, E. A.; Gabás, M.; Martínez, L.; Ramos-Barrado, J. R. *J. Phys. Chem. C* **2011**, *115* (43), 21373–21382.

- (110) Shrestha, K. M.; Sorensen, C. M.; Klabunde, K. J. *J. Phys. Chem. C* **2010**, *114* (34), 14368–14376.
- (111) Deng, D.; Cheng, Y.; Jin, Y.; Qi, T.; Xiao, F. *J. Mater. Chem.* **2012**, *22* (45), 23989.
- (112) Xu, S.; Song, X.; Fan, C.; Chen, G.; Zhao, W.; You, T.; Sun, S. *J. Cryst. Growth* **2007**, *305*, 3–7.
- (113) Vigderman, L.; Zubarev, E. R. *Chem. Mater.* **2013**, *25*, 1450–1457.
- (114) Karam, T. E.; Smith, H. T.; Haber, L. H. *J. Phys. Chem. C* **2015**, *119* (32), 18573–18580.
- (115) Deskins, N. A.; Du, J.; Rao, P. *Phys. Chem. Chem. Phys.* **2017**, *19*, 18671–18684.